Title
A large deviation framework for interacting systems far from equilibrium

Author
GrandPre, Trevor

Publication Date
2021

Peer reviewed|Thesis/dissertation

A large deviation framework for interacting systems far from equilibrium

by

Trevor GrandPre

A dissertation submitted in partial satisfaction of the

requirements for the degree of

Doctor of Philosophy

in

Physics

in the

Graduate Division

of the

University of California, Berkeley

Committee in charge:

Assistant Professor David T. Limmer, Co-chair
Associate Professor Oskar Hallatschek, Co-chair
Associate Professor Holger Mueller
Professor Phillip L. Geissler

Spring 2021

A large deviation framework for interacting systems far from equilibrium

Abstract

A large deviation framework for interacting systems far from equilibrium

by

Trevor GrandPre

Doctor of Philosophy in Physics

University of California, Berkeley

Assistant Professor David T. Limmer, Co-chair

Associate Professor Oskar Hallatschek, Co-chair

It has remained a mystery for the past few decades whether there is a non-equilibrium extension to equilibrium statistical mechanics. Recently, there has been advancements through dynamical relationships between currents and energy dissipation and correspondingly their distributions which comes from a framework called large deviation theory. Within this framework, large deviation functions operate in a similar fashion to the free energy in equilibrium which generates the cumulants for the energy. However, advancements of this theory have been mainly for non-interacting models that are exactly solvable. During my graduate career, I have made advancements towards predicting the fluctuations of interacting systems away from equilibrium. Towards this end, I developed a so-called weighted many body expansion which when combined with an approximate closure allowed for mean-field predictions for the distributions of entropy production and mass current in active matter. The same theory also allowed me to quantify density fluctuations and identify the type of phase transition that occurs in interacting active matter and in a model of 2 dimensional membrane-bound protein condensation. Akin to equilibrium distributions, by quantifying how the large deviation functions scale with system size gives information about the interface. I feel confident that my body of work has progressed the field and has provided a new perspective on a decades old problem.

I dedicate this to all the people in my life who have helped me get to this point.

Contents

List of Figures

List of Tables

Acknowledgments

My Wife, thank you for all of your love and support these past few years. We came to California together to pursue our dreams. I have learned from you to not only use logic in overcoming problems but to equally balance that with emotion. Without both, our humanity can be lost. Thank you for your patience and helping me be whole.

Mom and Dad, I will forever and always be your miracle baby. Thank you for giving me plentiful opportunity and knowledge to succeed. You all taught me discipline and foresight among other things. It is no doubt that that training has equipped me to tackle any obstacle I may face. You also made it possible for me to have such an expansive worldview. I am grateful to have had the opportunity to travel the world as a child even sometimes at the expense of school.

David, thank you for choosing me to be a part of your group. It has been an honor to learn so much and to arrive at a time when we could learn new theory together. It is rare to find someone as nurturing and caring as you in a boss. You truly cared about my success as much as yours. I could not have asked for a better adviser who taught me many things about science and research that would be difficult to learn on my own. I learned the delicate balance in academia between lingering on interesting problems to flush out subtleties and producing good work efficiently. The qualities that I have developed under your mentorship will certainly help me in the future.

Lastly, I would like to thank my wonderful colleagues and mentors that I have had along the way. Thank you Ahmad Omar, Katie Klymko, Kranthi Mandadapu, Summer Sun, Jay Groves, Johannes Blaschke, Ethan Levien, Ariel Amir, Phillip Geissler, and Lewis Pan.

Chapter 1

Introduction

1.1 Beyond equilibrium

Many biophysical systems are out of equilibrium and require a constant supply of energy to function. For instance, *E. Coli* is an example of active matter, systems that consume energy at the level of individual particles, which uses ATP hydrolysis to measure chemical concentration gradients, giving rise to directed motion and in some cases motility induced phase separation (MIPS) [1, 2]. Another set of non-equilibrium systems are those that have glassy dynamics and are slowly decaying to equilibrium but with prohibitively long relaxation times to reach the steady state. In the biophysical context, a membrane bound protein called Linker for Activation of T-Cells (LAT) enhances its signal transduction by phase separating into a dense and dilute phase [3, 4, 5]. In both sets of problems, fluctuations are essential in gaining mechanistic understanding. In active matter, it is known that MIPS arises from a dynamical instability where a large local density fluctuation can induce phase separation [6]. In the cell, stochastic fluctuations drastically impact the cellular function of proteins and genes and there is an increasing amount of examples showing that noise enhances functionality. Such is the case for signalling networks where it has been shown that noise improves coordination of downstream target genes and impacts the signalling network capacity [7]. It is a wonder how cells create collective order and develop into multicellular organisms from inherently noisy microscopic dynamics. A key component of vertebrate animal development is the LAT protein mentioned above which is essential for T-Cell receptor activation which initiates numerous signaling cascades that determine cell fate. In my thesis, I will discuss a theory that encompasses both of these vastly different types of non-equilibrium systems and the progress I have made in understanding them.

The ultimate goal is to develop a framework that provides predictive power similar to what we currently have for equilibrium systems. In equilibrium, the free energy contains all of the information you can possibly know about the system. For instance, the second derivative of the free energy gives us diffusion constants and the barrier provides rate constants. Out of equilibrium, the framework called large deviation theory provides a natural extension of the

free energy as well as a method to calculate rare fluctuations of relevant observables [8]. In fact, an equilibrium free energy is a large deviation function where the extensive parameter is the number of particles. Large deviation theory has provided the tools to understand critical phenomena in complex dynamical systems that are far from equilibrium. It has also provided a unique way to derive real forces needed to access rare fluctuations which give access to important dynamical phases in non-equilibrium systems.

Origin of fluctuations

In theory, all of the motion is contained in Newton's laws of motion but it requires every force acting on an object to be accounted for. With this equation, the trajectory of the system is completely determined by the initial conditions of the system. However, in practice, it is difficult to enumerate all the forces and in many cases all the forces are not even known.

From the intuition of classical mechanics, immersing a small object in a solvent would displace some of the solvent but then it would come to rest. However, in experiments it was discovered that such systems did not come to rest but continued to move in motion that looked like jiggling. It was later found that this jiggling came from collisions with solvent molecules with the immersed object. In principle, by keeping track of all of these collisions on the object, the equation of motion would be deterministic. This turns out to be a formidable task because of the enormous amount of molecules acting on an immersed body being on the scale of Avogadro's number with 10^{23} solvent molecules.

Instead of trying to account for all the forces and collisions exactly, the jiggling motion is modelled as noise which leads to a zero displacement on average but with some distance travelled about a fixed point given by the square root of two times a diffusion constant. Microscopically, the mix between deterministic forces and noise terms is given by a stochastic differential equation where in the overdamped case is given by

$$\frac{dx}{dt} = F(x,t) + B(x,t)\zeta(t) \ , \tag{1.1}$$

where B is the square root of the diffusivity, and $F(x,t)$ is the drift term composed of a force times a dissipative coefficient $\mu(x)$ (often called the mobility), potentially with an additional function $f(x,t)$ with units of velocity, $F(x,t) = -\mu(x)\frac{\partial \mathcal{H}}{\partial x} + f(x,t)$, where the first term is the mobility times the spatial derivative of the system hamiltonian. The noise and the force are related by the Stokes-Einstein relation

$$D(x) = \frac{B^2(x)}{2} = k_{\mathrm{B}} T \mu(x) \ . \tag{1.2}$$

This relation is also called the Fluctuation Dissipation Theorem and tells us that the amount of jiggling of an object is linearly proportional to the temperature of the solvent. The statistics of the noise are that it is zero on average,

$$\langle \zeta(t) \rangle = 0 \ , \tag{1.3}$$

and that the variance is delta correlated in time,

$$\langle \zeta(t)\zeta(t')\rangle = \delta(t-t'). \tag{1.4}$$

Hence, we see that this equation assumes that dynamic correlations occur instantaneously which is impossible for real systems and is an idealization. However, from the statistics of the noise, one cannot simply write the statistics of $x(t)$. To understand why, we write the equation of motion in Eq. 1.1 in a different form. This noisy process is also called a Wiener process written as

$$dx = F(x,t)dt + B(x,t)dW(t)\ , \tag{1.5}$$

with

$$dW(t) = \zeta(t)dt\ , \tag{1.6}$$

This equation does not tell us whether we should use in $B(x)$ the value of x before the jump, or at some other instance of time. Hence, this equation is only useful when we have instructions on how to evaluate the noise. We can integrate over the Wiener process and represent the integral as a Riemann-Stieltjes sum,

$$\int_0^t B[x(s),s]dW(s) \stackrel{\alpha}{=} \lim_{n\to\infty}\sum_{i=0}^{n} B(\bar{x}(t_i),t_i)[W(t_{i+1})-W(t_i)]\ , \tag{1.7}$$

where

$$\bar{x}(t_i) = \alpha x(t_{i+1}) + (1-\alpha)x(t_i) = x(t_i) + \alpha(x(t_{i+1})-x(t_i))\ . \tag{1.8}$$

Now we see that there are many choices of discretizations that can be chosen with a choice of α being any number from 0 to 1. The Ito interpretation ($\alpha = 0$) is that x in $B(x)$ should be taken right before the jump and is non-anticipating. Stratonovich ($\alpha = 1/2$) assumes that it should be taken halfway between its values before and after the jump. A third choice is to pick the "isothermal" convention ($\alpha = 1$) which is also referred to as the backwards Ito, because it takes the position at the end of the time step [9]. These are just three possible choices and in fact, a Langevin equation does not have meaning without an integration rule [10].

Not only that, which choice we make for α determines not only the equation of motion but also almost every property associated with that equation of motion such as the steady state distributions and the statistics of dynamical observables. These subtleties are not specific to out of equilibrium systems.

Fokker-Planck equation

An equivalent form of the dynamics is given by the time evolution of the probability distribution for the random variable, x, with time written as

$$\frac{\partial P(x,t)}{\partial t} \stackrel{\alpha}{=} -\frac{\partial(F(x,t)P(x,t))}{\partial x} - \frac{\partial(\alpha B'(x,t)B(x,t)P(x,t))}{\partial x} + \frac{1}{2}\frac{\partial^2(B(x,t)^2P(x,t))}{\partial x^2}\ , \tag{1.9}$$

where $D = B^2/2$ is the diffusivity. The drift term $F(x)$ is interpreted in the Ito sense and the second term in Eq. 1.9 comes from expanding $B(\bar{x}, t)$ around $B(x, t)$ (see Appendix Eq. A.1).

This shows that the discretization you choose will determine the drift that enters into the Fokker-Planck equation. These two terms represent the general α drift with reference to the Ito interpretation. This is clear from the fact that we expanded the $B(\bar{x}, t)$ around x (see Appendix A.1). In general, we can represent the drift terms in Eq. 1.9 with a general $F_{\alpha,\bar{\alpha}}(x, t)$ drift that denotes the drift in one α discretization to another $\bar{\alpha}$. In Eq. 1.9, the drift in the first two terms can be written in the $F_{\alpha,\bar{\alpha}}(x, t)$ form with $\bar{\alpha} = 0$ as

$$F_{\alpha,0} = F(x,t) + \alpha B(x,t)\frac{dB(x,t)}{dx} \ , \tag{1.10}$$

and more generally we can write

$$F_{\alpha,\bar{\alpha}}(x,t) = F(x,t) + (\alpha - \bar{\alpha})B(x,t)\frac{dB(x,t)}{dx} \ . \tag{1.11}$$

From this we see that the SDE in Eq. 1.1 can be written as

$$\frac{dx}{dt} \overset{\alpha}{=} F_{\alpha,\bar{\alpha}}(x,t) + B(x,t)\zeta(t) \ . \tag{1.12}$$

An alternate derivation utilizes the Kramers-Moyal Expansion, which is an expansion of the moments of the transition probability. A general expansion for the response is given by [11, 12]

$$\frac{\partial P(x,t)}{\partial t} \overset{\alpha}{=} \sum_{n=1}^{\infty} \frac{(-1)^n}{n!}\frac{\partial^n}{\partial x^n}\left[\kappa_n(x)P(x,t)\right] \ , \tag{1.13}$$

where the κ_n are the cumulants of the Langevin equation given (in α form) by

$$\kappa_n(x) \overset{\alpha}{=} \langle |x_{t+dt} - x_t|^n \rangle \overset{\alpha}{=} \int dx_{t+dt} |x_{t+dt} - x_t|^n P\left(x_{t+dt}|x_t\right) \ . \tag{1.14}$$

We can see now why the cumulants depend on α since we have to discretize the equation of motion. If we use the same drift as in (1.10), we see that we will obtain the same result as the previous section by going up to order $n = 2$ in this expansion (1.13). The first two cumulants are

$$\kappa_1(x) = F(x,t)\Delta t + \alpha B(x,t)\frac{dB(x,t)}{dx}\Delta t \ , \tag{1.15}$$

$$\kappa_2(x) = B^2\Delta t = 2D \ . \tag{1.16}$$

Note that $B(x, t)$ does not go away after averaging over the noise, ζ_t. Thus there is a stochastic contribution from the cumulants that depend on α. For an equilibrium system this should not be the case. We will come back to this point in the next section on maintaining the Boltzmann distribution. For now, we note that (1.9) can be rewritten as

$$\frac{\partial P}{\partial t} \overset{\alpha}{=} \frac{\partial}{\partial x}\left[-F(x,t) + (1-\alpha)B'(x,t)B(x,t) + \frac{1}{2}B^2(x,t)\frac{\partial}{\partial x}\right]P(x,t) \ . \tag{1.17}$$

Discretization determines the steady state distribution even in equilibrium

In Lau and Lubensky [13], they discuss the form of a drift term required for the particular noise interpretation used (α convention) in order to recover the Boltzmann distribution. If we again consider a stochastic differential equation of the form (1.5), and assume that $F(x)$ has a particular form:

$$F(x) = -\mu(x)\frac{\partial \mathcal{H}}{\partial x} + f(x) \ , \tag{1.18}$$

where $\mu(x)$ is the friction coefficient, $\mathcal{H}$ is the Hamiltonian, and $f(x)$ is left unspecified for now. The goal is to determine the correct form for $f(x)$ to obtain the correct equilibrium distribution $P(x,t)$, i.e. that the steady state distribution is

$$P(x,t) \sim e^{-\mathcal{H}/k_{\mathrm{B}}T} \ . \tag{1.19}$$

This can be achieved by deriving the Fokker-Planck equation, as described above and written in (1.17). Lau and Lubensky show that the equilibrium distribution is guaranteed at long times by using the Stokes-Einstein relation of

$$B^2(x) = 2k_{\mathrm{B}}T\mu(x) \ , \tag{1.20}$$

and

$$f(x) = (1-\alpha)B'(x,t)B(x,t) = (1-\alpha)k_{\mathrm{B}}T\mu'(x) \ . \tag{1.21}$$

This drift term (1.21) must be included in (1.18) in order to reach the Boltzmann distribution since the equilibrium distribution should not depend on the discretization we choose for the dynamics. Note that if we want $f(x) = 0$ we need to use the backwards Ito process ($\alpha = 1$). These details are exacerbated out of equilibrium because it is not even known what the underlying steady state distribution will be let alone how to choose a discretization to obtain it.

Many body systems

For an interacting system, the force in Eq. 1.18 would in principle depend on all the particles in the system,

$$F_i(\mathbf{r}^N) = -\mu(\boldsymbol{r_i})\frac{\partial \mathcal{H}(\mathbf{r}^N)}{\partial \boldsymbol{r_i}} + f(\boldsymbol{r_i}) \ . \tag{1.22}$$

The Fokker-Planck equation then involves a sum over all the particles in the system,

$$\frac{\partial P(\mathbf{r}^N,t)}{\partial t} = \sum_{i=1}^{N} -\boldsymbol{\nabla}_i \cdot \left(F_i(\mathbf{r}^N) - D\boldsymbol{\nabla}_i\right) P(\mathbf{r}^N,t) \ , \tag{1.23}$$

where we have made the substitution of $D = B^2/2$. It is, however, possible to turn the many body Fokker-Planck equation into an effective single particle one by defining a single and two particle reduced density as

$$P^{(1)}(\boldsymbol{r}, t) = \frac{N!}{(N-1)!} \int\int d\boldsymbol{r_2} d\boldsymbol{r_3} \dots d\boldsymbol{r_N} \hat{P}(\boldsymbol{r^N}, t) \tag{1.24}$$

and

$$P^{(2)}(\boldsymbol{r}, \boldsymbol{r'}, t) = \frac{N!}{(N-2)!} \int\int d\boldsymbol{r_3} d\boldsymbol{r_4} \dots d\boldsymbol{r_N} \hat{P}(\boldsymbol{r^N}, t) \ . \tag{1.25}$$

Using Eqs. 1.24 and 1.25 and inserting them into the Fokker-Planck equation in Eq. 1.23, we get

$$\frac{\partial P^{(1)}(\mathbf{r}, t)}{\partial t} = -\boldsymbol{\nabla} \cdot \left(\bar{F}(\mathbf{r}) - D_{\mathrm{t}} \boldsymbol{\nabla} \right) P^{(1)}(\mathbf{r}, t) \ , \tag{1.26}$$

where

$$\bar{F}(\mathbf{r}, t) = \int d\boldsymbol{r'} F(\boldsymbol{r}, \boldsymbol{r'}) P^{(2)}(\boldsymbol{r}, \boldsymbol{r'}, t). \tag{1.27}$$

However, we see that this effective single particle equation depends on the two particle density and the two particle density will end up depending on the three particle density, etc. Hence, we see that all of the information of the many body equation is still contained in the hierarchical equations of motion and an approximate closure must be made by defining a radial distribution function (RDF) as

$$g(\boldsymbol{r}, \boldsymbol{r'}, t) = \frac{\hat{P}^{(2)}(\boldsymbol{r}, \boldsymbol{r'}, t)}{\hat{P}^{(1)}(\boldsymbol{r}, t) \hat{P}^{(1)}(\boldsymbol{r'}, t)} \ . \tag{1.28}$$

When the system is homogeneous we can assume it doesn't depend on time and can instead use the relative distance, $r = |\boldsymbol{r} - \boldsymbol{r'}|$. This is an object that can be measured experimentally, measured from simulations, or approximated analytically. This concept of the many body expansion and the approximate closure will be useful in chapter 2.

1.2 Discrete state systems

Many problems are more amenable to a system with discrete states instead of continuous space. This is the case for chemical reactions where there is a finite amount of reactants and products. These systems avoid many of the subtleties of continuous space systems and the different interpretations possible. In the last section, I described the ways to define the dynamics of a system in continuous space. However, for systems in discrete space there are similar ways to write down the dynamics. This will be useful to know for chapter 5 where we build a reaction-diffusion model to understand phase transitions in the cell.

Consider a finite number of configurations, Ω. The probability that the system changes from configuration x to y, with y not equal to x, within a time $[t, t + \Delta t]$, given that the system was in configuration x at time t is

$$P^{\Delta t}(y|x, t) = k_t(x, y)\Delta t + o(\Delta t). \tag{1.29}$$

The transition rates are denoted by $k_t(x, y)$, which are greater than or equal to zero. It is convention to have $k_t(x, x) = 0$. The probability to make more than one jump in Δt is of order $o(\Delta t)$. The probability that the system does not perform a jump within $[t, t + \Delta t]$ is

$$P^{\Delta t}(x|x, t) = 1 - \lambda_t(x)\Delta t + o(\Delta t) \tag{1.30}$$

with the escape rate defined as

$$\lambda_t(x) = \sum_{x \neq y} k_t(x, y). \tag{1.31}$$

Given that the probability that the system is in state x at time t is $p_t(x)$, for all x, then the probability that the system is in another x at time $t + \Delta t$ is

$$p_{t+\Delta t}(x) = p_t(x) \left[1 - \lambda_t(x)\Delta t + o(\Delta t)\right] + \sum_{y \neq x} p_t(y) \left[k_t(y, x)\Delta t + o(\Delta t)\right]. \tag{1.32}$$

There are two contributions. the first term describes the probability that the system was in state x at time t and stayed there over the the time interval. The second term is the probability that it was in any state and jumped to x. This equation can be manipulated to give the master equation as

$$\frac{dp_t(x)}{dt} = \lim_{\Delta t \to 0} \frac{p_{t+\Delta t}(x) - p_t(x)}{\Delta t} = \sum_{y \neq x} \left[p_t(y)k_t(y, x) - p_t(x)k_t(x, y)\right]. \tag{1.33}$$

This is a deterministic equation all of the noise is contained in the probability distributions $p_t(x)$.

Global detailed Balance

When the rates of the markov process are independent of time, $k_t(y, x) = k(y, x)$, it is called time-homogeneous. Given that there exists a distribution $\pi(x)$, which is unique, then all of the distributions $p_t(x)$ converge in the long time limit to be

$$\lim_{t \to \infty} p_t(x) = \pi(x). \tag{1.34}$$

This would solve the master equation and

$$j_\pi(x, y) = \pi(x)k(x, y) - \pi(y)k(y, x). \tag{1.35}$$

In equilibrium $j_\pi = 0$, and detailed balance is obtained for every transition

$$\pi(x)k(x,y) = \pi(y)k(y,x). \tag{1.36}$$

When every node of a reaction network obeys detailed balance this is called global detailed balance which is also an equilibrium system. It means that when we start from detailed balance to develop an algorithm we will only sample equilibrium configurations. Rearranging Eq. 1.36, we get that the transition between two states is given by the exponential of β times the difference in energies between two states,

$$\frac{k(x,y)}{k(y,x)} = \frac{\pi(y)}{\pi(x)} = e^{\beta(E(x)-E(y))}. \tag{1.37}$$

1.3 Dynamical observables and averages

Types of observables

The observables we are concerned with are functions of trajectories. A large class of these can be represented as (in general α form)

$$A_t \overset{\alpha}{=} \frac{1}{t}\int_0^t g(x_t)dt + \frac{1}{t}\int_0^t h[x(s)]dx(s) \tag{1.38}$$

where

$$\int_0^t h[x(s)]dx(s) \overset{\alpha}{=} \lim_{n\to\infty}\sum_{i=0}^{n} h(\bar{x}(t_i))[x(t_{i+1}) - x(t_i)]. \tag{1.39}$$

The first term in Eq. 1.38 is a time-integrated density-like observable because it only depends on the phase space variables at one instance in time. However, the second term in Eq. 1.38 is a current-type observable because it depends on the phase space variables at two instances of time or transitions between them. In Eq. 1.39, it shows that the choice of integration will determine how the second term of 1.38 is interpreted.

One observable is the current which is the net displacement of a quantity such as mass, charge, or heat over some observation time. In terms of the original equation of motion in Eq. 1.1, the empirical mass current is

$$J_t(x_t) \overset{\alpha}{=} \frac{1}{t}\int_0^t \delta(x_t - x)dx. \tag{1.40}$$

We see that this observable is similar to the second term in Eq. 1.38. Another observable considered in my research is the empirical density defined as

$$\rho_t(x_t) = \frac{1}{t}\int \delta(x_t - x)dt. \tag{1.41}$$

In the stationary state this will converge to the reduced single particle density given that it obeys the Ergodic theorem as

$$\mu_t(x) = \lim_{t\to\infty} \rho_t(x_t). \tag{1.42}$$

In discrete space the mass current is written as

$$j_t(y,z) = \int_0^t dt\ \delta_{x(t^-),y}\delta_{x(t^+),z} - \delta_{x(t^-),z}\delta_{x(t^+),y}, \tag{1.43}$$

where the $x(t^{\pm})$ denotes the state before and after a jump.

Hydrodynamic observables

Aside from the microscopic observables described above, we can also equivalently define them in terms of a fluctuating density and current. We can define the general observable in terms of the empirical current and density as

$$\frac{1}{t}\int_0^t f(x_t)dt \stackrel{\alpha}{=} \frac{1}{t}\int_0^t f(x_t)dt \int \delta(y-x_t)dy \stackrel{\alpha}{=} \int dy h(y)\rho_t(y). \tag{1.44}$$

The second term of the observable can be rewritten as

$$\frac{1}{t}\int_0^t h(x_t)dx_t \stackrel{\alpha}{=} \frac{1}{t}\int_0^t h(y)dy \int_0^t \delta(y-x_t)dy \stackrel{\alpha}{=} \int_0^t h(y)J_t(y)dy. \tag{1.45}$$

Hence, the general observable is equivalently written as

$$A_t(\rho_t, J_t) \stackrel{\alpha}{=} \int dy h(y)\rho_t(y) + \int_0^t h(y)J_t(y)dy \tag{1.46}$$

This is the general hydrodynamic observable as a function of the density and current. The probability of observing both the empirical current and density is given by the level 2.5 rate function [14, 15]. This will be useful in chapter 4 when we study a fluctuating density framework for entropy production. As mentioned above, these observables are functions of the trajectory so in the next section I introduce the trajectory ensemble.

The trajectory ensemble

A trajectory is one of the many realizations of a stochastic process or path. It is defined as starting at $x(0)$ and ending at $x(T)$ at a time T as

$$\Gamma = \{x(t)\}_T^0 \tag{1.47}$$

The probability of taking a trajectory, Γ, given the initial condition $x(0)$ is

$$dP_{x(0)}(\Gamma). \tag{1.48}$$

Then the average observable is given by

$$\langle f(\Gamma)\rangle_{x(0)} = \int dP_{x(0)}(\Gamma) f(\Gamma), \tag{1.49}$$

where the integral is over all possible trajectories that start at $x(0)$ at time zero. This can be generalized by considering that there is a distribution of initial configurations that can be chosen. Namely, the probability of taking a trajectory from any starting point from the distribution $\rho_{ss}(x(0))$ is

$$dP_{\rho_{ss}(x(0))}(\Gamma) = \rho_{ss}(x(0)) dP_{x(0)}(\Gamma), \tag{1.50}$$

and the average observable over all initial configurations is

$$\langle f(\Gamma)\rangle_{\rho_{ss}(x(0))} = \int dP_{\rho_{ss}(x(0))}(\Gamma) f(\Gamma). \tag{1.51}$$

Now the integration is over all trajectories, not just those that start at a specific x_0. We can also split up the trajectory to calculate averages over parts of the trajectories. For instance we define a trajectory that starts at time zero and ends at s which is a time smaller than T as

$$\Gamma_1 = \{x_t\}_s^0 \tag{1.52}$$

and another trajectory that starts at time s and ends at time T as

$$\Gamma = \{x_t\}_T^s \ . \tag{1.53}$$

With this same logic, we can also generate trajectories starting from a configuration that is not from the steady state. Hence, even if a system would normally be in equilibrium, non-equilibrium dynamics occur until the system reaches the steady state. In the case of glasses, it takes a prohibitively long time to reach the steady state. This is elaborated on in chapter 5. For a Markov chain, a trajectory is determined by successive configurations as

$$\Gamma = [x(0), .., x(t)] \, . \tag{1.54}$$

The probability of a trajectory in this case given you start at $x(0)$ is

$$P_{x_0}(\Gamma) = \rho_{ss}(x(0)) \prod_{t=0}^{T-1} p(x(t) \to x(t+1)) \ , \tag{1.55}$$

where $p(x(t) \to x(t+1))$ is the transition probability of starting at postion $x(t)$ at time t and in one time step being at position $x(t+1)$ at time $t+1$.

Now that we have defined what a trajectory and a trajectory ensemble is, another question is how to generate it. This can be done by running many realizations of the dynamics in Eq. 1.1, or by the path action.

Path integral formulation: Onsager-Machlup with general discretization

The choice of α is equally important in defining a path probability or trajectories generated by Eq. 1.1. We write the SDE in the Langevin form as the following:

$$\frac{x_{t+dt} - x_t}{dt} \stackrel{\alpha}{=} F(\bar{x}_t) + B(\bar{x}_t)\zeta_t \ , \tag{1.56}$$

with

$$\bar{x}_t = \alpha x_{t+dt} + (1-\alpha)x_t = x_t + \alpha(x_{t+dt} - x_t) \ . \tag{1.57}$$

Without loss of generality, let's consider the probability of starting from $x(0)$ at $t = 0$ and ending up at $x(dt)$ after one time step. The transition probability is written as

$$P(x_{dt}|x_0) = \int d\zeta_0 \delta(x_{dt} - X_1(x_0, \zeta_0)) P(\zeta_0) \ . \tag{1.58}$$

where $X_1(x_0, \zeta_0)$ is a realization of x_{dt} after one time-step starting from t=0, and

$$P(\zeta_0) = e^{\frac{\zeta_0^2 dt}{4D}} \tag{1.59}$$

By using identities for the delta-function, doing a Gaussian integral, and taking the continuous time limit (see Appendix A.2), we get the path integral to be [16]

$$P(x_t|x_0) \stackrel{\alpha}{=} J[x(t)] \exp(-S[x(t)]) \ , \tag{1.60}$$

with

$$J[x(t)] \stackrel{\alpha}{=} \prod_t \left(\frac{1}{2\pi dt}\right)^{1/2} \frac{1}{|B(\bar{x}_t)|}, \tag{1.61}$$

and

$$S[x(t)] \stackrel{\alpha}{=} \int dt \left(\frac{1}{2} \left[\frac{\dot{x}_t - F(x_t) + \alpha B(x_t) B'(x_t)}{B(x_t)} \right]^2 + \alpha F'(x_t) \right) \ . \tag{1.62}$$

There are a couple other ways to write down the path action by introducing auxiliary variables. These other ways are noted in Appendix A.2 but all forms will in principle generate the same paths.

Path integral for discrete state systems

The path probability for a sequence of hops can be written as

$$P[x(t)] = \rho_{ss}(x(0)) \prod_{k=0} k(x_k, x_{k+1}) e^{-\lambda_t(x_k)(t_{k+1} - t_k)} \tag{1.63}$$

where $k(x_{k+1}, x_k)$ are elements of the rate matrix and $\lambda_t(x_i)$ is the sum of all rates exiting site i. The time-reversed path probability can be written as

$$P[\tilde{x}(t)] = \rho_{ss}(x(t)) \prod_{k=0} k(x_k, x_{k+1}) e^{-\lambda_t(x_{k_1})(t_k - t_{k+1})} \tag{1.64}$$

Taking the ratio, we get that the entropy production to be

$$\Omega[x(t)] = \ln \frac{\rho_{ss}(x(0))}{\rho_{ss}(x(t))} + \sum_k \ln \frac{k(x_k, x_{k+1})}{k(x_k, x_{k+1})} \ . \tag{1.65}$$

The first term is a boundary term and does not grow with time. However, The second term grows with time and so it is the entropy production defined as

$$w[x(t)] = \sum_k \ln \frac{k(x_k, x_{k+1})}{k(x_k, x_{k+1})} \tag{1.66}$$

Local detailed balance

However, the principle of detailed balance can also be used for non-equilibrium dynamics where instead of every node on a reaction network obeying detailed balance, we have a pair of nodes in detailed balance without respect to the rest of the network. This is called local detailed balance and is a concept in stochastic thermodynamics [17, 18]. The local detailed balance relates the ratio of rates to the total entropy change of the system as

$$\frac{k(x, y)}{k(y, x)} = e^{\beta(s(x,y))}, \tag{1.67}$$

where $s(x, y)$ is the total entropy change from the transition.

Although the concept of detailed balance was shown for the discrete state system, the same concept can be shown in the continuous space case. When detailed balance is broken at the microscopic level, there will be entropy production. This will be elaborated on in chapter 4.

1.4 Large deviation theory

The mathematical theory of large deviations is concerned with the exponential decay of the probability of extreme events while the number of observations grows [19]. The theory encompasses equilibrium-like observables of steady state properties but the theory also has the the ability to describe dynamical properties [20].

Large deviation principle and level-1 rate functions

We assume that the observable obeys the large deviation principle (LDP) given by

$$P(A_t = a) = \lim_{t\to\infty} \exp(-tI(a) + o(t)) \tag{1.68}$$

which defines the level one rate function as

$$I(a) = \lim_{t\to\infty} t^{-1} \ln[P(A_t = a)] \tag{1.69}$$

If the limit exists, then the observable is said to obey a LDP. In general, t^{-1} is the speed at which fluctuations decay. This could be in size or in time or both. Given that you are in the long time limit all distributions should collapse on to this same curve. LDT works when this is valid. However, sometimes the breaking of the LDP gives information given the LDP held at one point in a similar way that the breaking of the free energy with finite size scaling means that there is a phase transition. The LDP could break down due to non-ergodicity or from non-markovian effects.

In practice the rate function is hard to calculate exactly so we usually calculate the cumulant generating function first and use that to calculate the rate function.

1.5 Cumulant generating function

The cumulant generating function is one of the starting points to large deviation theory. It is defined as the Laplace transform of the path action and is based on the **Gärtner-Ellis Theorem**. Suppose that the scaled cumulant generating function of a random variable A_t defined as

$$\psi(\lambda) = \lim_{t\to\infty} \frac{1}{t} \log e^{t\lambda A_t} \tag{1.70}$$

is differentiable everywhere. Then A_T satisfies an LDP with rate function

$$I(a) = \max_{\lambda\in R} \left(\lambda a - \psi(\lambda)\right). \tag{1.71}$$

This theorem also ensures that the Legendre-Fenchel transform is self inverse for the time intensive observable A_t. This also means that the Legendre-Fenchel transform can be done in reverse to get the CGF from the rate function. It is possible that if the Gartner-Ellis theorem does not rigorously hold for all λ that the theorem is applicable where the CGF is differentiable. However, complete information is only transferred between the two ensembles when the rate function is convex.

1.6 Derivation of the tilted markov generator

The tilted markov generator takes the form of [21, 22, 23]

$$L = L_0 + a(x)\cdot\nabla + b(x), \tag{1.72}$$

where

$$L_0 = (F + \alpha\nabla D)\cdot\nabla + \nabla D\nabla \tag{1.73}$$

This generator corresponds to a process that adds a force, $a(x)$, and shrinks and expands the phase space with $b(x)$. Course-graining the dynamics in the Ito convention for the jacobian and using the Feynman Kac formula for $b(x)$, we get

$$P_{ab}(\Gamma) = exp[\int_0^T dt' \frac{-|\frac{dx}{dt} - F(x) - a(x)|^2}{4D} + b(x)]. \tag{1.74}$$

The original dynamics have the path probability of

$$P(\Gamma) = exp[\int_0^T dt' \frac{-|\frac{dx}{dt} - F(x)|^2}{4D}]. \tag{1.75}$$

By taking the the ratio of the two, we see the extra contribution to the path probability is

$$\frac{P(\Gamma)}{P_{ab}(\Gamma)} = \exp[R_T(x)], \tag{1.76}$$

where

$$R_T(x) = \int_0^T \frac{a(x_T)\cdot dx_t}{2D} + \int_0^T (b - a(x)\cdot\frac{(F + a(x)/2)}{2D})dt'. \tag{1.77}$$

We can use the relationship to convert the observable from Ito to a general alpha discretization as

$$\int_0^t a(x_t)dx_t \stackrel{\alpha}{=} \int_0^t a(x)dx_t + 2D\alpha\int_0^t \nabla\cdot a(x)dt, \tag{1.78}$$

and turn Eq. 1.77 into

$$R_T(x) \stackrel{\alpha}{=} \int_0^T \frac{a(x_t)dx_t}{2D} + \int_0^T (b - a(x)\cdot\frac{(F + a(x)/2)}{2D} - \alpha(\nabla\cdot a))dt'. \tag{1.79}$$

Using the fact that

$$R_T(x) \stackrel{\alpha}{=} \lambda T A_T, \tag{1.80}$$

the forms of a and b can be solved for then put back into Eq. 1.72 and gives the tilted generator to be [24]

$$L_\lambda = F\cdot(\nabla + \lambda h(x)) + D(\nabla + \lambda h(x))^2 + \lambda g(x) + 2D\left(\alpha - \frac{1}{2}\right)\lambda\nabla h(x). \tag{1.81}$$

There are a few limiting cases to consider as they will be done in my work. Notice, that if $h(x) = h$, meaning that it does not depend on position, the last term vanishes. In the first section of my thesis this is the case with the mass current. The last term can also vanish if the Stratonovich convention is chosen.

Generalized Doob transform

The dynamics conditioned on a value of the observable can be done by a control force. In principle, this force is the exact force that generates the trajectories in the actual system but are extremely rare to see in the unbiased system. The left eigenvector corresponding to the largest eigenvalue can be used to generate the control force by

$$F_\lambda(x) = 2D\left(\lambda h(x) + \nabla \log \nu(x)\right). \tag{1.82}$$

When this force is added to the original dynamics, the rare statistics of the observable is obtained [8].

Chapter 2

Current statistics in active matter

Introduction

This chapter is based largely on one of my papers [25].

Persistent currents are the hallmark of a system driven away from equilibrium. One of the simplest and most fundamental problems of nonequilibrium physics is to predict the structure of the fluctuations of currents around a nonequilibrium steady-state and to decode the microscopic information contained in them. Non-equilibrium fluctuation-dissipation relations [26, 27, 28, 29, 30, 31, 32], fluctuation theorems [33, 34, 35, 36, 37, 38, 22], and thermodynamic uncertainty relations [39, 40, 41, 42] are notable examples of successes towards this end. Much of this progress has been underpinned by the study of large deviation functions (LDFs), which supplies a general framework to compute and characterize fluctuations of extensive observables [43, 22]. The LDF of the current can be viewed as the analog of a free energy, making relationships between fluctuations and response to external perturbations transparent [44, 45, 46, 47]. However, the evaluation of LDFs for interacting systems remains challenging. In this chapter, we characterize the fluctuations of currents in a system of interacting active Brownian particles (ABPs) and show how these fluctuations encode the response of the system.

ABPs are a simple model of active matter, a class of systems that convert energy from the environment into directed motion. ABPs evolve nonequilibrium steady states as they break detailed balance at the single particle level due to a constant nonconservative driving force. More than just being non-Boltzmann, their steady-states support unique phenomena such as motility induced phase separation [48, 49]. Laboratory realizations of ABPs include cellular biopolymers [50, 51, 52], bacteria [53, 54, 55, 56, 57, 58, 59], and synthetic colloids [60, 61, 62, 63, 64]. We derive the current LDFs for ABPs and validate it with molecular simulation. We find that small current fluctuations are Gaussian, and the associated linear response obeys Fick's law, as has been shown for noninteracting ABPs [65]. Large current fluctuations are non-Gaussian and the associated nonlinear response results from a change in the particle's orientational correlations, which we characterize with the effective potential that renders those fluctuations typical.

2.1 Fluctuation Dissipation Theorem and diffusion

The botanist Robert Brown discovered what we now call Brownian motion in 1827 by watching pollen suspended in water jiggling under a microscope. The first theoretical work was given by Einstein who explained this irregular motion by the Fluctuation Dissipation Theorem in 1905 and by Smoluchowski in 1906. Langevin followed up on this work in 1908 which introduced noise terms into Newton's second law.

The idea of Brownian motion from a microscopic perspective is that tiny solvent molecules are hitting the object immersed in the solvent. All of these collisions gives rise to random motion. Of course, if we could track all the particles around the immersed object the motion would not be random but would follow Newton's second law. This jiggling motion in the overdamped case can be written in terms of the mean squared displacement of the equation of motion in Eq. 1.5 with no forces,

$$\overline{(x(t) - x(0))^2} = 2D_{\mathrm{t}}t, \tag{2.1}$$

with the Fluctuation Dissipation Theorem relating the diffusion constant to the parameters of the solvent as

$$D_{\mathrm{t}} = k_B T \mu, \tag{2.2}$$

where k_B is Boltzmann's constant, T is the temperature, and μ is the mobility. When interparticle forces are included in the microscopic equations of motion, the self-diffusion defined in Eq. 2.1 becomes dependent on the local density and linearly decreases with increases density [25].

However, one must question whether or not the Fluctuation Dissipation Theorem still holds for nonequilibrium systems such as active matter. In the next section, I define a fundamental variable called the mass current and quantify the fluctuations of this variable which are related to the diffusion coefficient and higher order transport coefficients.

2.2 Mass current in interacting active matter

The equations of motion for active matter considered is of the form of Eq. 1.1. The dynamics of the ith particle is

$$\dot{\mathbf{r}}_i = v\,\mathbf{b}_i + \mu \mathbf{F}_i\left(\mathbf{r}^N\right) + \sqrt{2D_{\mathrm{t}}}\boldsymbol{\eta}_i \ , \tag{2.3}$$

with a non-conservative force $v\boldsymbol{b}$, which is driven by a constant energy supply and has the statistics of $\boldsymbol{b_i} = \{\cos(\theta_i)\hat{\boldsymbol{x}}_i, \sin(\theta_i)\hat{\boldsymbol{y}}_i\}$, where $\hat{\boldsymbol{x}}_i$ and $\hat{\boldsymbol{y}}_i$ are the unit vectors in the x and y directions, respectively. The dynamics of θ_i are Brownian,

$$\dot{\theta}_i(t) = \eta_i^{\theta}(t) \ , \tag{2.4}$$

where η_i^θ is a Gaussian white noise, satisfying $\langle \eta_i^\theta(t) \rangle = 0$ and $\langle \eta_i^\theta(t) \eta_j^\theta(t') \rangle = 2D_\mathrm{r}\delta_{ij}\delta(t-t')$ with D_r the rotational diffusion constant. The interparticle forces are conservative, $\boldsymbol{F}(\boldsymbol{r}^N) = -\nabla U(\boldsymbol{r}^N)$, and in general depend on all N particles' positions, $\boldsymbol{r}^N$. The form of the potential in this section is taken to be the a WCA interparticle potential [66], $U(r) = 4\epsilon\left[\left(\frac{\sigma}{r}\right)^{12} - \left(\frac{\sigma}{r}\right)^{6}\right] + \epsilon$ for $r \leq 2^{1/6}\sigma$ and zero otherwise.

We can generate an ensemble of trajectories of the system from the previous equation as described in Eq. 1.47 with dynamical observables being functions of these trajectories as shown in Eq. 1.38. For instance, a fundamental observable that tells us about transport is the mass current which is the particle's displacement over a period of time. It could be linked to transport via the diffusion constant and higher order transport coefficients which tells us about the phase behavior through the mass continuity equation.

The mass current can be written in terms of the generalized observable in Eq. 1.38 for particle i as

$$\boldsymbol{J}_i = \frac{1}{t}\int_0^t dt'\, \dot{\mathbf{r}}_i(t') = \frac{\mathbf{r}_i(t) - \mathbf{r}_i(0)}{t}, \tag{2.5}$$

where the observation time, t, is assumed to be large and the integration is taken to be in the Ito convention ($\alpha = 0$). The total current for all particles in the system is $\boldsymbol{J}^N = \{\boldsymbol{J}_1, \ldots, \boldsymbol{J}_N\}$. The cumulant generating function of this observable is

$$\psi(\lambda) = \frac{1}{t}\ln\left\langle e^{\boldsymbol{\lambda}\cdot\boldsymbol{J}^N t}\right\rangle \tag{2.6}$$

with the average being taken over $P(r^N, \theta^N, t)$, the joint distribution of observing all of the particles in a particular position and orientation at time t. The time evolution of the generating function is given by

$$\frac{\partial \hat{P}(\boldsymbol{\lambda}, \boldsymbol{r}^N, \boldsymbol{\theta}^N, t)}{\partial t} = L_\lambda^N \hat{P}(\boldsymbol{\lambda}, \boldsymbol{r}^N, \boldsymbol{\theta}^N, t)\ , \tag{2.7}$$

and defines the tilted generator as mentioned in Eq. 1.81. It has two terms, $L_\lambda^N = L_0^N + \Delta L_\lambda^N$, where

$$L_0^N = \sum_{i=1}^N \left(\mu \mathbf{F}_i\left(\mathbf{r}^N\right) + v\,\mathbf{b}_i + D_\mathrm{t}\boldsymbol{\nabla}_i\right)\cdot\boldsymbol{\nabla}_i + D_\mathrm{r}\partial_{\theta_i}^2 \tag{2.8}$$

is conservative and whose adjoint gives the Fokker Planck operator. The $\boldsymbol{\lambda}$ dependent term is

$$\Delta L_\lambda^N = \sum_{i=1}^N \left(\mu \mathbf{F}_i\left(\mathbf{r}^N\right) + v\,\mathbf{b}_i + 2D_\mathrm{t}\boldsymbol{\nabla}_i + D_\mathrm{t}\boldsymbol{\lambda}\right)\cdot\boldsymbol{\lambda} \tag{2.9}$$

and does not conserve probability.

There are two limiting cases of interest to consider. We can consider the total current as the sum over the individual particle currents, by setting $\boldsymbol{\lambda} = \lambda \cdot \mathbb{1}$ where λ is a scalar parameter and $\mathbb{1}$ the identity. However, this case is trivial because the sum of the interparticle

force vanishes and the solution is identical to the non-interacting solution. In this case, the total current CGF is equivalent to N times the CGF for a single ABP. Alternatively, we can consider the current statistics of a single tagged ABP, which has a density dependence from surrounding particles. This is done by setting $\boldsymbol{\lambda}$ to be a vector with a single nonzero element, $\boldsymbol{\lambda} = \{0, 0, 0, \cdots, \lambda, \cdots, 0, 0, 0\}$. This second case contains the first in the limit of low density, and provides additional information on the dependence of current fluctuations on interactions. In my work, I considered the latter definition.

We would like to get an effective single particle tilted generator by integrating out the other particle's degrees of freedom. A generalization of the Bogoliubov-Born-Green-Kirkwood-Yvon–like hierarchy [67] is introduced which is called the weighted many body expansion. Specifically, we define an n-particle reduced generating function

$$\hat{P}^{(n)}(\lambda, \boldsymbol{r}^n, \boldsymbol{\theta}^n, t) = \frac{N!}{(N-n)!} \int\int d\boldsymbol{r}^{(N-n)} d\boldsymbol{\theta}^{(N-n)} \hat{P}(\lambda, \boldsymbol{r}^N, \boldsymbol{\theta}^N, t)\,, \tag{2.10}$$

which combined with Eqs. 2.7-2.9, results in a set of coupled evolution equations for different $\hat{P}^{(n)}$'s.

The single particle generating function depends on the two particle density so closure is needed. Closure is obtained by decomposing the two particle function as

$$g_\lambda(\boldsymbol{r}, \theta, \boldsymbol{r'}, \theta', t) = \frac{\hat{P}^{(2)}(\lambda, \boldsymbol{r}, \theta, \boldsymbol{r'}, \theta', t)}{\hat{P}^{(1)}(\lambda, \boldsymbol{r}, \theta, t)\hat{P}^{(1)}(\lambda, \boldsymbol{r'}, \theta', t)} \tag{2.11}$$

where $g_\lambda(\boldsymbol{r}, \theta, \boldsymbol{r'}, \theta', t)$ is the pair distribution function conditioned on a given current through λ [68, 69]. When the system is in a homogeneous state, with rotational and translational invariance, the radial distributon function can be written in terms of relative positions and orientations as $g_\lambda(\boldsymbol{r}, \theta, \boldsymbol{r'}, \theta', t) \approx g_\lambda(r, \phi)$, where ϕ is the angle of the displacement vector of two particles relative to the orientation of the particle at the origin. This closure to the many-body hierarchy was introduced previously for the case of $\lambda = 0$ [6, 70, 71, 72].

The single particle generating function will depend on the average interparticle force. This force is decomposed into components in the parallel and perpendicular direction of the self-propulsion, however this will result in an average force that depends on both the relative angle between the interparticle displacement vector and the tagged particle's orientation. The component perpendicular to the orientation is approximated as that parallel to the surface of the tagged particle which uncouples these two terms allowing for the expansion to be closed [6]. For $v \gg 1$, this decomposition gives quantitatively accurate results.

In a homogeneous system, both x and y coordinates will have the same statistics individually. Hence, without loss of generality we focus on the statistics in the x direction with the effective single particle operator for a mass current bias being

$$L_\lambda = V_\lambda(\rho)\cos(\theta)(\partial_x + \lambda) + D_{\mathrm{t}}(\rho)(\partial_x + \lambda)^2 + D_{\mathrm{r}}\partial_\theta^2, \tag{2.12}$$

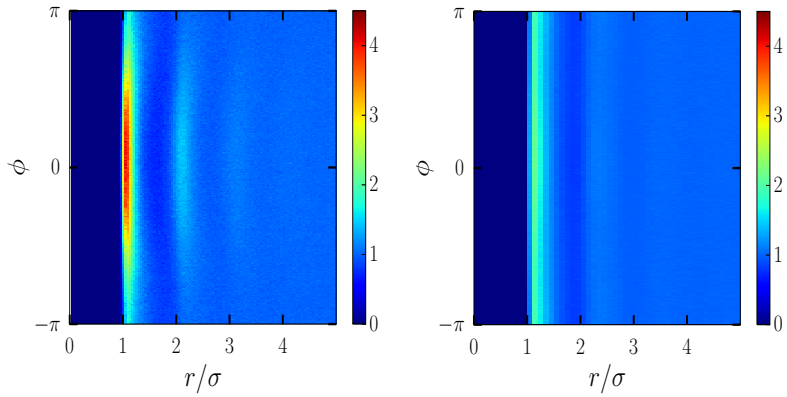

Figure 2.1: The 2 dimensional radial distribution function as a function of the relative position and angle at $\lambda = 0$ and $\lambda = 20$. The first peak is reduced at high large λ showing polar alignment.

which has the same drift-diffusion form as an independent ABP, but with a density-dependent propulsion speed, $V_\lambda(\rho)$, and translational diffusion constant, $D_\mathrm{t}(\rho)$, where ρ is the local density, and is taken to be equal to the bulk density. The adjoint of the operator in Eq. 2.12 evaluated at $\lambda = 0$ yields the propagator for the single particle density. The density dependent diffusion constant, $D_\mathrm{t}(\rho)$, describes the diffusion of passive particles in an interacting system with the mean field form being $D_\mathrm{t}(\rho) \approx D_\mathrm{t}(1-\rho)$ [71]. The density dependent propulsion speed has the form $V_\lambda(\rho) = v - \rho\zeta_\lambda(\rho)$ with $\rho\zeta_\lambda(\rho)$ is an effective drag. This drag is calculated by an integral over the interparticle force

$$\zeta_\lambda(\rho) = \int_0^\infty dr \int_0^{2\pi} d\phi\, r\cos(\phi) g_\lambda(r,\phi) F(r) \tag{2.13}$$

weighted by the pair distribution function. This coefficient describes the decrease in the effective velocity of a tagged particle due to the increased density of impenetrable particles in the direction of self-propulsion [6]. An example of how the 2D radial distribution function looks like, as described in Eq. 2.13, for $v = 10$ and two different $\lambda's$ is given in Fig. 2.1 which shows that higher currents are achieved by avoiding collisions. The drag coefficient has a number of known limiting forms. By construction, for independent particles or $\rho \to 0$, the drag $\rho\zeta_\lambda(\rho) \to 0$. We find that for all v, this approach is linear in ρ. Similarly, for $v \to 0$, the system becomes isotropic and $\zeta_\lambda(\rho) \to 0$. For large v, $\zeta_0(\rho) \approx v/\rho^*$ where $\rho^* \approx 1.2$, corresponding to an effective closed-packing density. We find that for $v > 30$, this approximation is within 1%, but even for $v \approx 5$, this form is within 10% of the computed value.

Using the theory defined above we solve for the mean-field CGF for current fluctuations by solving the eigenvalue equation, $L_\lambda \nu_\lambda = \psi(\lambda)\nu_\lambda$, with $\psi(\lambda)$ being the CGF and ν_λ its corresponding right eigenvector. The solution to this differential equation is the zeroth

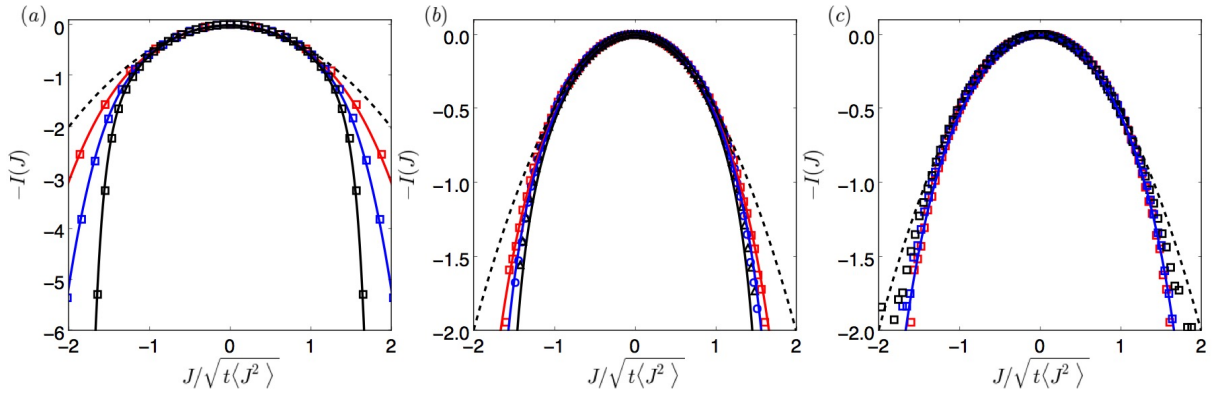

Figure 2.2: Comparison between the analytical rate function and its numerical evaluation. (a) Rate functions for $\rho = 0$ and $v = 5$ (red), 10 (blue), and 60 (black). (b) Rate functions for $\rho = 0.1$ and $v = 10$ (red), 30 (blue), and 60 (black). (c) Rate functions for $v = 10$ with $\rho = 0.1$ (red), 0.3 (blue), and 0.5 (black). Shown are the Legendre transforms of Eq. 2.14 (solid lines), numerical simulations (symbols) and reference Gaussian (dashed line).

characteristic function of Mathieu's equation [73], with a small λ representation given by the expansion,

$$\psi(\lambda) = D_{\mathrm{t}}(\rho)\lambda^2 + D_{\mathrm{r}}\left[\frac{z_\lambda^2(\rho)}{2} - \frac{7z_\lambda^4(\rho)}{32} + \frac{29z_\lambda^6(\rho)}{144}\right] + \mathcal{O}(\lambda^8) \tag{2.14}$$

with $z_\lambda(\rho) = V_\lambda(\rho)\lambda/D_{\mathrm{r}}$. For the case where there is no self-propulsion, $z_\lambda(\rho) = 0$, and $\psi(\lambda)$ reduces to that for Brownian motion with a density dependent diffusion constant $D_{\mathrm{t}}(\rho)$. In the infinite dilution limit our results reduce to those obtained previously [74].

As mentioned at the outset we want to calculate the probability distribution for observing a current within a period of time. Now with the CGF, the rate function is given by $I(J) = \max_\lambda[\lambda J - \psi(\lambda)]$, and $I(J)$ is minus the logarithm of the probability of J divided by the observation time.

In figure 2.2 the quantitative accuracy is shown and compared to simulations of $\psi(\lambda)$ for a variety of different ρ's and v's. Fluctuations close to the mean, $J = 0$, are Gaussian but larger fluctuations are more rare than expected from a Gaussian distribution. As v increases the non-Gaussian deviations become larger as shown in Fig. 2.2 with the x-axis scaled by $\sqrt{t\langle J^2\rangle}$. As shown, increasing the density slows the particles down and changes the effective self-propulsion.

2.3 Bias on rare current fluctuations

As shown in Fig. 2.2, the large deviations are markedly non-Gaussian. We can understand the nature of these fluctuations by making the rare fluctuations common by calculating control forces. By the so-called doob transform we can condition current fluctuations to reach a rare value of the current on average [43]. The doob transform is a transformation of the tilted generator so that probability is now conserved,

$$\begin{aligned}\mathcal{L}_\lambda &= \nu_\lambda(\theta)^{-1} L_\lambda \nu_\lambda(\theta) - \psi(\lambda) \\ &= L_0 + 2D_{\mathrm{t}}(\rho)\lambda\partial_x + 2D_{\mathrm{r}}\partial_\theta \ln \nu_\lambda(\theta)\,\partial_\theta \end{aligned} \tag{2.15}$$

which does not change the diffusion and adds a drift that is λ dependent. The dynamics with the control force for a tagged particle is

$$\dot{\mathbf{r}}(t) = \mu \mathbf{F}_i\left(\mathbf{r}^N\right) + v\,\mathbf{b} + 2D_{\mathrm{t}}(\rho)\lambda\hat{\boldsymbol{x}} + \boldsymbol{\eta}_{\mathrm{t}}(t)\,. \tag{2.16}$$

The control force for the orientation creates a torque on the orientation, $F_\lambda(\theta) = 2D_{\mathrm{r}}\partial_\theta \ln \nu_\lambda(\theta)$, for small λ is

$$\dot{\theta}_i(t) = -2V_\lambda(\rho)\lambda\sin(\theta) + \eta_{\mathrm{r}}(t) \tag{2.17}$$

and has an amplitude that depends on the λ dependent effective self propulsion containing the friction coefficient, $\zeta_\lambda(\rho)$. The friction can also be measured directly from the exact biased dynamics [75].

The control force on the orientation causes the tagged particle to have a preferred swim direction as shown in Fig. 2.3a), which shows the preferred directions at $\theta = 0$ and π. Additionally, It is seen that the effective drag is significantly reduced with an increasing magnitude of λ as shown in Fig. 2.3b), where $\zeta_\lambda(\rho)$ is computed from the molecular simulations for a variety of densities. At large $|\lambda|$, $\zeta_\lambda(\rho)$ eventually goes to zero meaning that the particles surrounding the tagged particles align their orientations with the tagged particle. This shows that the mechanism to have high currents is to eliminate interactions through alignment.

We can directly change the average current of the tagged particle to a nonzero average from the current bias. The prediction for this response is seen from the derivatives of $\psi(\lambda)$ which provide the cumulants of J, $d^n\psi(\lambda)/d\lambda^n = C^n_\lambda$. The first cumulant, $C^1_\lambda = \langle J\rangle_\lambda$, yeilds the average current and the second predicts the variance to be $C^2_\lambda = t\langle(J - \langle J\rangle_\lambda)^2\rangle_\lambda$. When these cumulants are evaluated at $\lambda = 0$ they represent the unbiased dynamics. When $\lambda \neq 0$ this gives the prediction for the rare fluctuations in the tails of $I(J)$ as shown in Figs. 2.3c) and d). Those figures show the biased currents at a nonzero λ from the exact solution of the eigenvalue equation and from evaluating Eq. 2.5 directly from simulations of the auxiliary process defined in Eqs. 2.16 and 2.17. At small λ, the current is linear with a slope proportional to the diffusion constant representing Gaussian fluctuations. At large λ, there is a nonlinear response which is marked by another linear region with a reduced slope. The slope of this secondary response is dependent on the $D_{\mathrm{t}}(\rho)$ only. This is because when

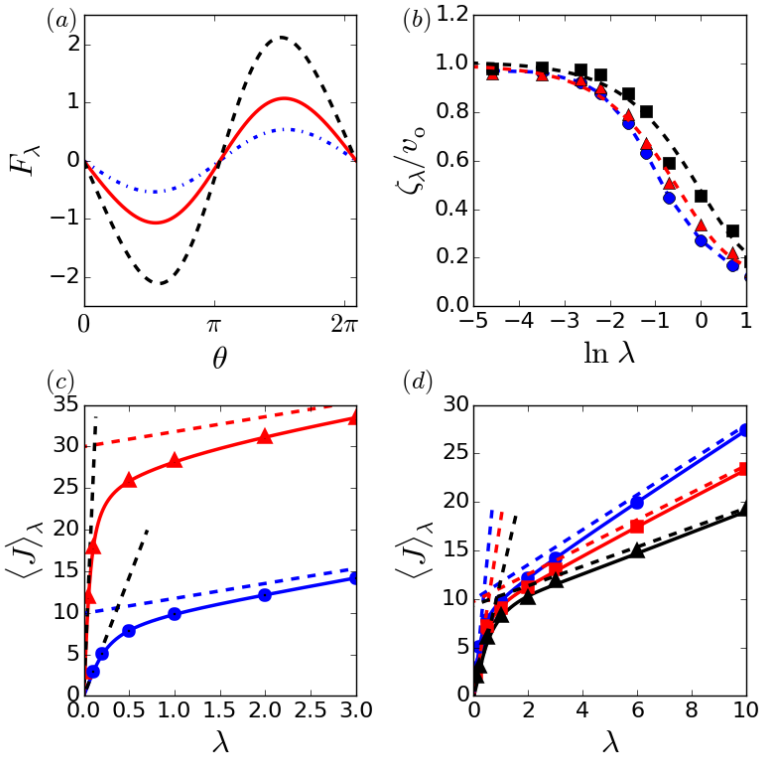

Figure 2.3: Analysis of the auxiliary process. (a) The effective forces for v=10, $\rho = 0.1$ and $\lambda = 0.1$ (blue), 0.3 (red), and 0.5 (black). (b) Damping coefficient, ζ_λ, as a function of λ for v=10 and $\rho = 0.1$ (blue), 0.3 (red), and 0.5 (black). Dashed lines are a guide to the eye. (c,d) The average current from the auxiliary process. (c) $\langle J \rangle_\lambda$ for $\rho = 0.1$ and v=10 (blue) and 30 (red). (d) $\langle J \rangle_\lambda$ for v=10, and $\rho = 0.1$ (blue), 0.3 (red) and 0.5 (black). The symbols are the results from simulations. The solid lines represent the derivative of the CGF and the dotted lines represent its limiting behavior.

all of the particles are moving in the same direction, the system behaves as an equilibrium system in a reference frame moving at v. The CGF in this limit is given by

$$\psi(\lambda) = D_t(\rho)\lambda^2 \pm v\lambda, \quad \lambda \to \pm\infty, \tag{2.18}$$

This analysis shows that a simple effective temperature mapping to equilibrium systems would not explain the non-Gaussian fluctuations and response [76, 77, 78, 79]. Further, The idea of two diffusion constants has the same qualiative features recently observed in active biopolymers, with the second diffusion constant being larger than the first [80, 81].

Effective temperature

As mentioned in the previous section, there is often mention of an equilibrium mapping by defining an effective temperature [82, 83]. Here, I will briefly describe the arguments for how one could approximately define an effective temperature which is based on calculating the pressure.

In equilibrium, the pressure P of a fluid can be defined in three equivalent ways: as the mechanical force per unit area on the walls of the container, from thermodynamics as the derivative of a free energy, and as the trace of the hydrodynamic stress tensor of the fluid, which in turn represents the momentum flux in the system. In equilibrium, all three definitions give the same expression and the pressure is a state function. This is not true in general for non-equilibrium systems.

The total pressure of an active gas has three contributions and can be written as

$$P = P_0 + P_D + P_s \tag{2.19}$$

where P_0 is the ideal contribution and the contribution from interparticle interactions to the pressure is represented by P_D. Self propelled particles have an additional contribution to the pressure that describes the flux of self-propulsion force across a unit line, P_s. This contribution is unique to active systems and was termed 'active' or 'swim' pressure. It was shown that the swim pressure can be written in a virial-type form as

$$P_S = \frac{\rho}{2}\langle \boldsymbol{r} \cdot v\,\mathbf{b}\rangle = \frac{vV(\rho)\gamma}{2D_{\mathrm{r}}}\rho. \tag{2.20}$$

In the absence of interactions $P_D = 0$, we can approximate the pressure of an ideal active gas as

$$P_s^0 = P_s + P_0 = \rho T + P_S = \rho T + \frac{vV(\rho)\gamma}{2D_{\mathrm{r}}}\rho = \rho T_{\mathrm{eff}}, \tag{2.21}$$

where

$$T_{\mathrm{eff}} = T + \frac{vV(\rho)\gamma}{2D_{\mathrm{r}}}. \tag{2.22}$$

In other words, the swim pressure of an ideal active gas is simply the pressure of an ideal gas at the temperature T_{eff}. This mapping is made to try to make reference to the powerful equilibrium framework. However, we have already shown that this is not rigorously true. Nonetheless, this swim pressure is also relevant to the entropy production which takes a similar form to the active pressure. This will be talked about further in chapter 4.

2.4 Linear transport

As mentioned in the introduction, we can also calculate transport coefficients from the CGF. The second cumulant is

$$C_0^2(\rho) = 2D_{\mathrm{t}}(\rho) + \frac{V_0^2(\rho)}{D_{\mathrm{r}}} \equiv 2\mathcal{D}(\rho)\,, \tag{2.23}$$

which we define as twice a collective diffusion constant, $\mathcal{D}(\rho)$. In Fig. 2.4, numerical results obtained from simulations of the mean-squared displacement are plotted in excellent agreement with predictions from Eq. 2.23. This form of the diffusion coefficient has been shown to agree with simulations previously, and was derived by a moment expansion of the joint position and orientation distribution [84, 85, 86, 48]. This density dependence of $\mathcal{D}(\rho)$ was shown by others [70, 6, 77] to correctly predict the spinodal instability signaling the onset of motility induced phase separation.

The current fluctuations encoded by $\mathcal{D}(\rho)$ provide the response of a hydrodynamic current, J_ρ, generated from a slowly varying spatial density, $\rho(x)$. From the Kramer's Moyal expansion [87], J_ρ can be generally expressed as a gradient expansion

$$J_\rho = -\sum_{n=1}^{\infty} \frac{(-1)^n}{n!} \partial_x^{n-1} M^n[\rho(x)]\rho(x) \tag{2.24}$$

where $M^n[\rho(x)]$ is the local density-dependent nth moment of the current, $\langle (J - \langle J \rangle)^n \rangle$. To first order, the mass current is linear in the density gradient and is given by Fick's law, $J_\rho \approx -\mathcal{D}(\rho)(\partial\rho/\partial x)$, where $\mathcal{D}(\rho)$ is the proportionality constant relating the current to the gradient resulting from identifying the second moment with the second cumulant. Since for small average currents we have have $\langle J \rangle_\lambda \approx 2\mathcal{D}(\rho)\lambda$, which shows that at linear response, λ can be related to an affinity for this nonequilibrium system. We have computed $\mathcal{D}(\rho)$ from $-J_\rho/(\partial\rho/\partial x)$ by simulating an open channel in contact with two reservoirs. As shown in Fig. 2.4, we find good agreement with $\mathcal{D}(\rho)$ computed in this way and from $\psi(\lambda)$. From $\psi(\lambda)$, we have access to all moments of J, and together with its ρ dependence this framework allows us to quantify higher order responses that are not naturally considered in standard field theoretic treatments of ABPs.

While our focus has been on ABPs, the framework we have presented is general and allows for the quantification of current fluctuations, and the calculation of transport coefficients for continuous interacting systems. For ABPs, we found that large current fluctuations near the mean are not representative of rarer fluctuations which are restricted as a result of coherent active movement. These specific results are consistent with deviations from Gaussian behavior that have been reported in recent experimental studies of active colloids [88, 89]. Furthermore, there are a number biological systems that are modeled by ABPs, such as cellular biopolymers that exhibit two types of transport characterized by two different diffusion constants for small and large fluctuations [80, 81]. Our analysis may help understand these observations. Finally, while we have focused on current fluctuations, our development of the weighted many body expansion provides a way to calculate the CGF of other relevant quantities for nonequilibriums systems such as activity [90, 91, 92, 69, 93, 94], entropy production [95, 96, 97, 98], the density, and other counting statistics that are currently difficult to estimate [99]. This framework will also be revisited in subsequent chapters on the density and entropy production.

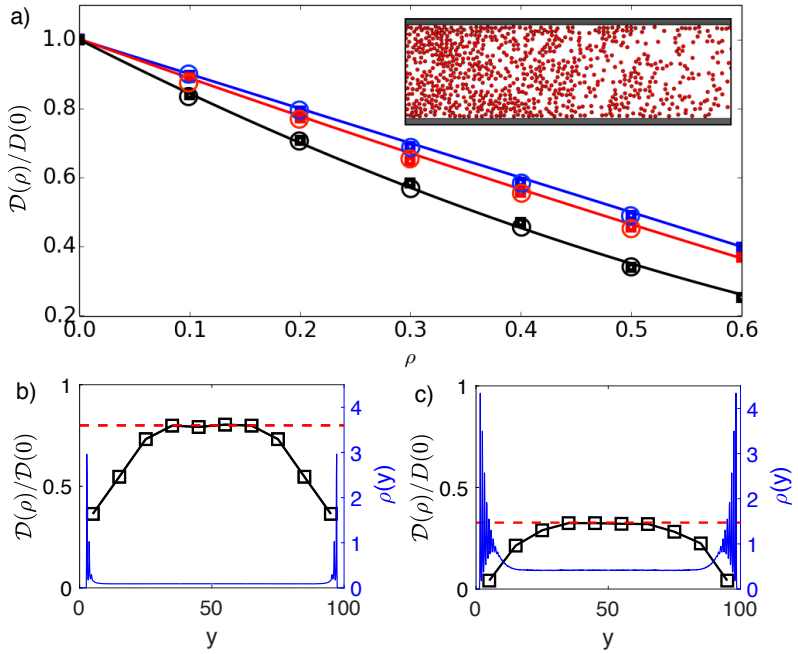

Figure 2.4: Density dependent effective diffusion constant for v= 0 (blue), 1 (red), and 60 (black). The symbols are the results from simulations. The squares are from the mean squared displacement, open circles are from an imposed density gradient and the solid lines from Eq. 2.23. Inset shows a snapshot of the simulation with an imposed density gradient.

Relation between λ and affinity

In the previous section, the density dependence of the diffusion constant was neglected. However, the diffusion constant could vary with position along the channel. When the effective diffusion constant is considered to be positionally dependent, then the hydrodynamic current becomes

$$J_\rho \approx -\left[\frac{\rho V_0(\rho)}{D_r}\frac{\partial V_0(\rho)}{\partial \rho} + \mathcal{D}\left(\rho\right)\right]\frac{\partial \rho}{\partial x} \tag{2.25}$$

where the first term was neglected in the previous expression for Fick's Law. The diffusion due to thermal fluctuations is neglected. Since the effective swim speed in the first term is a decreasing function with increasing density, it is negative and provides a prediction for phase separation noted previously [48, 6, 86, 100, 84].

By defining a density dependent chemical potential,

$$\mu_0(\rho) = \ln(\rho V_0^2(\rho)), \tag{2.26}$$

the hydrodynamic current can be rewritten as

$$J_\rho = -\mathcal{D}(\rho)\rho\frac{d\mu_0(\rho)}{dx} \tag{2.27}$$

which is an affinity that drives the hydrodynamic current. We can relate this to λ from the first derivative of the CGF with λ, giving the average current at small λ to be

$$\langle J\rangle_\lambda = 2\mathcal{D}(\rho)\lambda + \mathcal{O}(\lambda^3). \tag{2.28}$$

Hence, at small λ we can relate it to an affinity,

$$\lambda = -\frac{\rho}{2}\frac{d\mu_0(\rho)}{dx}. \tag{2.29}$$

More generally, away from linear response, λ and the affinity are still related, but this relation is more complicated [101, 102, 103, 104, 47, 105, 106, 107, 108, 109, 110, 111, 112].

2.5 Nonlinear transport

We can continue the Kramers Moyal expansion to the next non-zero term in Eq. 2.24, which would include the fourth moment, $M^4 = C_0^4 - 3(C_0^2)^2$. To this order, the hydrodynamic current would be given by

$$J_\rho = -\mathcal{D}(\rho)\rho\left(\frac{d\mu_0(\rho)}{dx} + \frac{d\mu_1(\rho)}{dx}\right) \tag{2.30}$$

which includes an additional contribution to the effective chemical potential, $\mu_1(\rho)$ given by

$$\mu_1(\rho) = \alpha(\rho)\left(\frac{d\rho}{dx}\right)^2 + \beta(\rho)\frac{d^2\rho}{dx^2}, \tag{S18}$$

with $\alpha(\rho)$ and $\beta(\rho)$ being coefficients that depend on the density, v_0, D_t and D_r. Keeping the first order in the derivatives of the density we get

$$\begin{aligned}\alpha(\rho)\mathcal{D}(\rho)\rho =& \frac{(-7+4D_r)}{4D_r^3}\left[V_0^3(\rho)\frac{\partial V_0}{\partial\rho} + \frac{3V_0^2(\rho)\rho}{2}\left|\frac{\partial V_0}{\partial\rho}\right|^2\right] \\ &+ \frac{\partial V_0}{\partial\rho}\left[\frac{2V_0(\rho)}{Dr} + \frac{\rho}{D_r}\frac{\partial V_0}{\partial\rho}\right]\end{aligned}$$

$$\begin{aligned}\beta(\rho)\mathcal{D}(\rho)\rho =& \frac{1}{2} + \frac{\partial\mathcal{D}(\rho)}{\partial\rho} + \\ &\frac{(-7+4D_r)}{8D_r^3}\left[\frac{V_0^4(\rho)}{4} + \frac{\rho V_0^3(\rho)}{8}\frac{\partial V_0}{\partial\rho}\right]\end{aligned}$$

which shows that our framework allows us to quantify higher order response with the next order response containing non-gradient terms that would give rise to interfacial energy-like terms necessary to stabilize two phases, $d^2\rho/dx^2$ and $|d\rho/dx|^2$ [113, 48, 6].

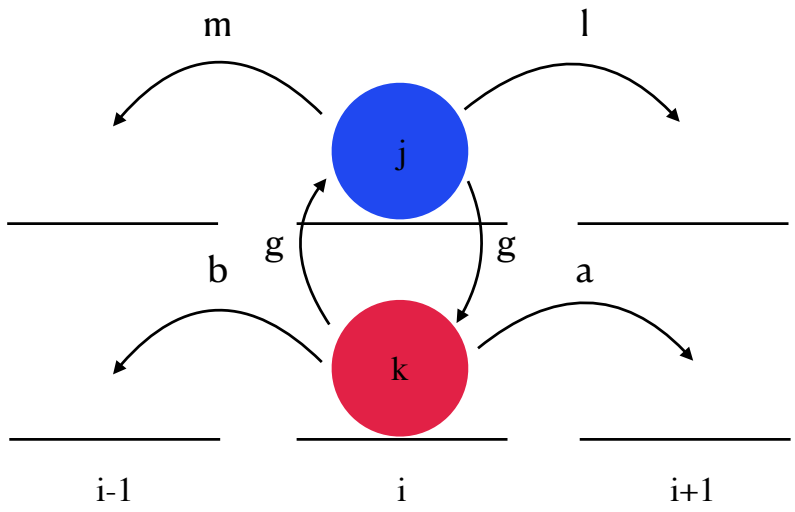

Figure 2.5: Lattice model of active matter. There are two types of particles j and k. Particle j hops forward on the lattice with rate l and backwards with rate m. Likewise, particle k hops forward on the lattice with rate a and backwards with rate b.

2.6 Relationship of on-lattice and off-lattice fluctuations

Sometimes it has proven useful to study active matter on a lattice instead of in the continuum. In this section, I will describe a microscopic version of ABPs and a discrete version of the mass current and solve the eigenvalue problem.

Instead of continuous space motion, particles on a lattice hop from one site to another. The mass current is defined as the number of directed hops. Over a time t, we measure the amount of hops from state y to state z and vice versa written as

$$J_T = \frac{1}{T}\int_0^T q[\delta_{x(t^-),y}\delta_{x(t^+),z} - \delta_{x(t^-),z}\delta_{x(t^+),y}]dt. \tag{2.31}$$

Here q is the lattice spacing and the $x(t^{\pm})$ denotes the state before and after a jump. In the long time limit, the current will go to a steady-state distribution of

$$J_{y,z} = k(y,z)\pi(z) - k(z,y)\pi(y)\ . \tag{2.32}$$

Similarly to the continuum case there is a tilted generator that is derived in a similar way to the continuum case for dynamics biased on the number of directed hops given by

$$\frac{d\pi(i)}{dt} = e^{+\lambda}k(i,i+1)\pi(i+1) + e^{-\lambda}k(i-1,i)\pi(i) - r(i)\pi(i). \tag{2.33}$$

Now that we understand how to bias the dynamics, we are left to determine a consistent way to calculate the rates that describes the equations of motion for ABPs. To enforce this constraint, we construct the transition rates in such a way that the first two jump moments give the correct drift and diffusion by solving

$$q(k(i,i+1) - k(i+1,i)) = M_1 \tag{2.34}$$

$$q^2(k(i,i+1) + k(i+1,i)) = M_2. \tag{2.35}$$

In a similar way, we can define an active lattice model with two particle types, j and k. Particle j hops forward on the lattice with rate l and backwards with rate m. Particle k hops forward on the lattice with rate a and backwards with rate b. Additionally, particle j can turn into particle k with rate g. The summary of the rates for each particle is displayed in Fig. 2.5. We can solve for these rates in terms of the continuous space equations by solving for the rates from Eqs. 2.34-2.35 for position and orientation given by

$$q(l-m) = v, \tag{2.36}$$

$$q^2(l+m) = 2D_{\mathrm{t}}, \tag{2.37}$$

$$q(a-b) = -v, \tag{2.38}$$

$$q^2(a+b) = 2D_{\mathrm{t}}, \tag{2.39}$$

$$q^2(g+g) = 2D_{\mathrm{r}}. \tag{2.40}$$

In the long time limit particle j and Particle k have a drift of v and $-v$. In this way, particle j and k are the same particle with different self-driven velocities in equal and opposition directions. This makes the assumption that in the long time limit only 1 and -1 survive from the orientation vector. By solving Eqs. 2.36-2.40, we get that

$$l = \frac{v}{2q} + \frac{D_{\mathrm{t}}}{q^2}, \tag{2.41}$$

$$m = \frac{-v}{2q} + \frac{D_{\mathrm{t}}}{q^2}, \tag{2.42}$$

$$b = \frac{+v}{2q} + \frac{D_{\mathrm{t}}}{q^2}, \tag{2.43}$$

$$a = \frac{-v}{2q} + \frac{D_{\mathrm{t}}}{q^2}, \tag{2.44}$$

and

$$g = \frac{D_{\mathrm{r}}}{q^2}. \tag{2.45}$$

The CGF for this system on a ring is given by the largest eigenvalue of the tilted rate matrix with the rates described. We find that the CGF on the lattice is

$$\psi(\lambda) = \frac{2D_{\mathrm{t}}}{q^2}(-1 + \cosh(\lambda q)) - \frac{D_{\mathrm{r}}}{q^2} + \sqrt{\frac{D_{\mathrm{r}}^2}{q^4} + v^2 \sinh^2(\lambda q)} \tag{2.46}$$

Taking the continuum limit where $q \to 0$ means we expand the hyperbolic sine and cosine and the terms that survive are

$$\psi(\lambda) = D_{\mathrm{t}}^2 \lambda^2 - D_{\mathrm{r}} + \sqrt{D_{\mathrm{r}}^2 + \frac{v^2\lambda^2}{2}} \tag{2.47}$$

We are interested to know how well does this capture the fluctuations in relation to the exact answer. Taking two derivatives of $\psi(\lambda)$ defined in Eq. 2.47 with respect to λ and evaluating it at $\lambda = 0$ gives us a diffusion constant that matches the CGF in Eq. 2.23 when $\rho = 0$ representing infinite dilution.

Up until this point, we have only considered non-interacting ABPs on the lattice. We can perturbatively correct the noninteracting solution by considering particle interactions on a ring [68]. The exact expression for the large deviation function for current for the interacting system is

$$\psi(\lambda) = \left[\frac{2D_{\mathrm{t}}}{q^2}(-1 + \cosh(\lambda q)) - \frac{D_{\mathrm{r}}}{q^2} + \sqrt{\frac{D_{\mathrm{r}}^2}{q^4} + v^2 \sinh^2(\lambda q)}\right] \rho(1 - < n_i n_{i+1} >)), \tag{2.48}$$

where n_i is the indicator function which is 1 when a particle is at site i and zero when the site is empty. Taking the limit that $q \to 0$ gives us the mean field approximation given as

$$\psi(\lambda) = \left(D_{\mathrm{t}}^2 \lambda^2 - D_{\mathrm{r}} + \sqrt{D_{\mathrm{r}}^2 + \frac{v^2\lambda^2}{2}}\right)(\rho(1 - \rho^2)). \tag{2.49}$$

This gives the local collective diffusion constant as

$$D(\rho) = \left(D_{\mathrm{t}} + \frac{v^2}{2D_{\mathrm{r}}}\right)(1 - \rho) \approx D_{\mathrm{t}}(\rho) + \frac{vV_0(\rho)}{2D_{\mathrm{r}}} \tag{2.50}$$

which is similar the the density dependent diffusion constant in Eq. 2.23 but with the friction coefficient, ζ, equal to 1.

The lattice description has proven to be accurate up to the diffusion term. However, higher order statistics when compared to the exact result deviate. This is not too surprising since the rates were calculated from the first two moments of the equations of motion. In principle, higher order statistics might be accurate in the lattice model if higher order moments were used to calculate the rates.

Chapter 3

Density fluctuations and phase separation

Introduction

In a grand canonical ensemble in equilibrium, there is a precise relationship between the chemical potential of the particle bath, the distribution of density of the system, and the free energy.

Out of equilibrium, there has been some work to extend these ideas to a nonequilibrium steady states. For a homogeneous system, the large deviation function for density fluctuations acts like a free energy and a chemical potential of the bath can be defined to quantify the density fluctuations in active systems [85]. When there is phase separation, there have also been several works to quantify the phase diagram of 2D active systems with an effective free energy which is bimodal at the two densities in coexistance [114, 2].

There is much success in characterizing the steady state density profile of homogeneous and phase separated systems. One question I will answer is how this phase transition is related to a dynamical phase transition. Specifically, we aim to understand what information do we gain by including spatial and dynamical information. First, I will give theory developed to understand dynamical density fluctuations for non-interacting systems. Then, I will use the concepts learned from those cases to apply to interacting active matter near criticality.

3.1 Time integrated equilibrium density fluctuations in one dimension

Open boundaries

This section is primarily a summary of the work in a previous paper [115]. We will consider the open boundaries case first because of its close relationship with textbook quantum me-

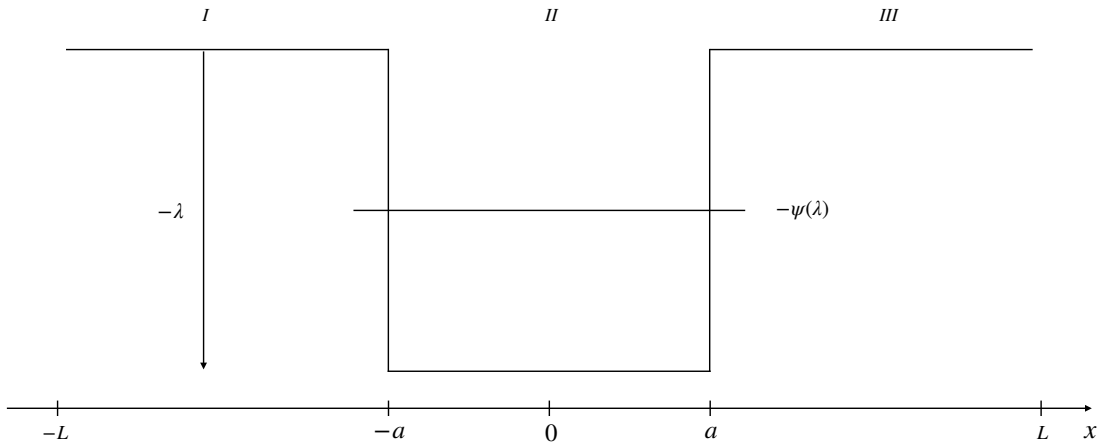

Figure 3.1: An illustration of the system for a bias on density to be in region II and it's equivalence to the finite square well problem in quantum mechanics.

chanics. This will make the case of periodic boundaries easier to explain afterwards which is my specific contribution.

For a single particle system in 1 dimension, we consider a bias on a single particle to be in a region of space for a fraction of time defined as

$$\rho_t = \frac{1}{t}\int_0^t h(x(t))dt, \tag{3.1}$$

where $h(x_t)$ is 1 when the particle is within the sub system at time t, and is zero when it is outside of it. As shown in Fig. 3.1 , we consider the observable of a particle being in a region of space of $-a \leq x \leq a$, denoted region II, where $2a$ is the length of the subsystem. The total system size is $2L$ which for the first example is taken to be much larger than subsystem, $L \gg a$. Given that the Fokker-Planck equation for Brownian motion is

$$\frac{\partial \rho(x,t)}{\partial t} = D_{\mathrm{t}}\nabla^2\rho(x,t). \tag{3.2}$$

The operator of this equation is

$$L_0^{\dagger} = D_{\mathrm{t}}\nabla^2, \tag{3.3}$$

and the tilted version based on Eq. 3.3 is

$$L_0 = D_{\mathrm{t}}\nabla^2 + \lambda h(x_t). \tag{3.4}$$

It has been noted that solving for the largest eigenvalue of this operator is identical to solving the finite square well problem in 1 dimension [115, 116]. The eigenvalue problem we wish to solve is the following:

$$L_\lambda \nu_\lambda(x) - \psi(\lambda)\nu_\lambda(x) = 0, \tag{3.5}$$

where $\nu_\lambda(x)$ is the λ and x dependent eigenvector corresponding to the largest eigenvalue. We must solve this equation for the region inside the subsystem and outside. We show the three cases below:

$$\begin{cases} \nabla^2\nu_\lambda(x) - \frac{\psi(\lambda)}{D_\mathrm{t}}\nu_\lambda(x) = 0 & x < -a \\ \nabla^2\nu_\lambda(x) + \frac{\lambda-\psi(\lambda)}{D_\mathrm{t}}\nu_\lambda(x) = 0 & -a \le x \le a \\ \nabla^2\nu_\lambda(x) - \frac{\psi(\lambda)}{D_\mathrm{t}}\nu_\lambda(x) = 0 & x > a \end{cases} \tag{3.6}$$

The general solution for the eigenvector is

$$\nu_\lambda(x) = \begin{cases} Ae^{k_1 x} + Ee^{-k_1 x} & x < -a \\ B\cos(k_2 x) + C\sin(k_2 x) & -a \le x \le a \\ De^{-k_1 x} + Fe^{+k_1 x} & x > a \end{cases} \tag{3.7}$$

where

$$k_1^2 = \frac{\psi(\lambda)}{D_\mathrm{t}}, \tag{3.8}$$

and

$$k_2^2 = \frac{[\lambda - \psi(\lambda)]}{D_\mathrm{t}}. \tag{3.9}$$

In order for the eigenvectors to be normalizable, it must be the case that $E = F = 0$ and the general solution becomes

$$\nu_\lambda(x) = \begin{cases} Ae^{k_1 x} & x < -a \\ B\cos(k_2 x) + C\sin(k_2 x) & -a \le x \le a \\ De^{-k_1 x} & x > a \end{cases}. \tag{3.10}$$

There are still five unknowns which are the CGF, $\psi(\lambda)$, and A, B, C,and D. To solve for the other four constants we must note that the other boundary conditions are

$$\begin{cases} \nu_\lambda^I(x=-a) = \nu_\lambda^{II}(x=-a) & (i) \\ \frac{d\nu_\lambda^I(x=-a)}{dx} = \frac{d\nu_\lambda^{II}(x=-a)}{dx} & (j) \\ \nu_\lambda^{II}(x=a) = \nu_\lambda^{III}(x=a) & (k) \\ \frac{d\nu_\lambda^{II}(x=a)}{dx} = \frac{d\nu_\lambda^{III}(x=a)}{dx} & (l) \end{cases} \tag{3.11}$$

From Eqs. 3.11i and 3.11j, we find that

$$Ae^{-k_1 a} = B\cos(k_2 a) - C\sin(k_2 a) \tag{3.12}$$

and

$$k_1 Ae^{-k_1 a} = k_2 B\sin(k_2 a) + k_2 C\sin(k_2 a). \tag{3.13}$$

By defining $\theta^2 = k_2^2 a^2 = \frac{[\lambda - \psi(\lambda)]a^2}{D_\mathrm{t}}$ and dividing Eq. 3.12 by Eqs. 3.13, we find that

$$k_1 = k_2 \left(\frac{B\sin(\theta) + C\sin(\theta)}{B\cos(\theta) - C\sin(\theta)} \right). \tag{3.14}$$

Now by doing the same calculation for Eqs. 3.11k and 3.11l, we get

$$k_1 = k_2 \left(\frac{B\cos(\theta) - C\sin(\theta)}{B\sin(\theta) + C\sin(\theta)} \right). \tag{3.15}$$

We now have two equations for k_1 and by setting Eqs. 3.14 and 3.15 equal we get

$$\left(B^2 + C^2\right)\sin(\theta)\cos(\theta) + BC = \left(B^2 + C^2\right)\sin(\theta)\cos(\theta) - BC \tag{3.16}$$

This equation has two solutions. Either $BC = -BC$ or $BC = 0$. Hence, it must be the case that either $C = 0$ or $B = 0$. This represents the fact that solutions for bound states have to be either even or odd. The case of $B = C = 0$ is not possible for this reason.

The largest eigenvalue is given by the first order quantum solution which is the symmetric solution. The symmetric solution is obtained when $C = 0$. Then Eq. 3.10 reduces to

$$\nu_\lambda(x) = \begin{cases} Ae^{k_1 x} & x < -a \\ B\cos(k_2 x) & -a \leq x \leq a. \\ De^{-k_1 x} & x > a \end{cases} \tag{3.17}$$

Applying the same boundary conditions in Eq. 3.11 , we find that

$$\frac{k_1}{k_2} = \tan(\theta). \tag{3.18}$$

This equation cannot be solved analytically but we can find the roots for a given λ, by rewriting the left hand side as

$$\frac{k_1}{k_2} = \sqrt{\frac{\psi(\lambda)}{\lambda - \psi(\lambda)}} = \sqrt{\frac{\theta_0^2}{\theta^2} - 1}, \tag{3.19}$$

with

$$\theta_0^2 = \frac{\lambda a^2}{D_\mathrm{t}}. \tag{3.20}$$

Combining Eqs. 3.18 and 3.19 , the final equation to be solved for the CGF is

$$\sqrt{\frac{\theta_0^2}{\theta^2} - 1} = \tan(\theta). \tag{3.21}$$

If we denote the roots of this equation as $\theta^*(\lambda)$, the CGF is

$$\psi(\lambda) = \lambda - \frac{D_\mathrm{t}\left(\theta^*(\lambda)\right)^2}{a^2}. \tag{3.22}$$

Note that since the system has open boundaries, it is quite uncommon for the particle to stay within the box and on average

$$\left.\frac{d\psi(\lambda)}{d\lambda}\right|_{\lambda=0} = \langle\rho\rangle_{\lambda=0} = 0. \tag{3.23}$$

Also, the force as a function of lambda on the particle is

$$F_\lambda(x) = \begin{cases} \sqrt{4D_{\rm t}\psi(\lambda)} & x < -a \\ -\sqrt{4D_{\rm t}(\lambda-\psi(\lambda))}\tanh(\sqrt{\frac{(\lambda-\psi(\lambda))}{D_{\rm t}}}x) & -a < x < a \\ -\sqrt{4D_{\rm t}\psi(\lambda)} & x > a \end{cases}. \tag{3.24}$$

For positive λ, inside the subsystem the force traps the particle in a bound state with the depth increasing as a function of λ. These were the results of previous papers [115, 116].

In the next section, I describe my notable contributions to the problem by deriving the CGF for periodic systems in which case the average density will be the bulk density of the system. This will then help us to incorporate orientation and interactions in subsequent sections.

Periodic boundaries

As mentioned previously, for infinite boundary conditions, $L \gg a$, we would set $E = F = 0$ to make the eigenvectors normalizable. Since our system has periodic boundary conditions we have to keep these coefficients. We now consider the case where a/L is order 1. Namely, the fraction will give us the average occupancy in the system as

$$\langle\rho\rangle_0 = \frac{a}{L}. \tag{3.25}$$

In the periodic case the boundary conditions are different. We have 6 equations to solve for our 7 coefficients which are the following:

$$\begin{cases} \nu_\lambda^I(x=-a) = \nu_\lambda^{II}(x=-a) & (i) \\ \frac{d\nu_\lambda^I(x=-a)}{dx} = \frac{d\nu_\lambda^{II}(x=-a)}{dx} & (j) \\ \nu_\lambda^{II}(x=a) = \nu_\lambda^{III}(x=a) & (l) \\ \frac{d\nu_\lambda^{II}(x=a)}{dx} = \frac{d\nu_\lambda^{III}(x=a)}{dx} & (k) \\ \nu_\lambda^I(x=-L) = \nu_\lambda^{III}(x=L) & (m) \\ \frac{d\nu_\lambda^I(x=-L)}{dx} = \frac{d\nu_\lambda^{III}(x=L)}{dx} & (n) \end{cases} \tag{3.26}$$

Using the same procedure in the previous section, we find that the root equation in this case is

$$\frac{k_1}{k_2} = \frac{\tan(k_2 a)}{\tanh\left[k_1\left(L-a\right)\right]} = \sqrt{\frac{\lambda}{\lambda-\psi(\lambda)} - 1}. \tag{3.27}$$

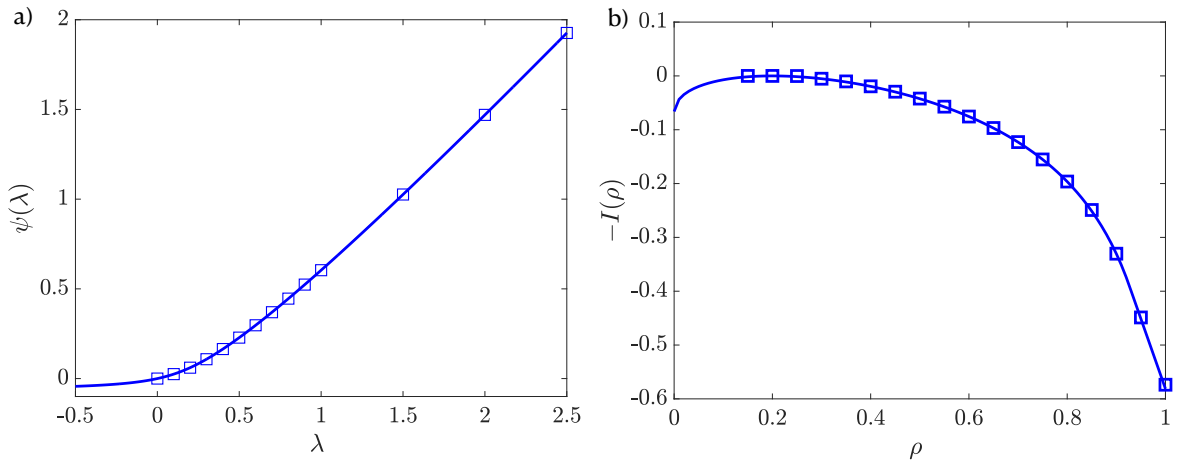

Figure 3.2: The exact large deviation functions for the Brownian walker with periodic boundaries (solid line) compared with cloning results (square symbols). a) the CGF for a wide range of λ's. b) The corresponding rate function for density fluctuations. Both a) and b) are with $D_{\rm t} = 1/2$, $a = 1$, and $L = 5$.

This result generalizes Eq. 3.18. Note that when we take the limit that $L \to \infty$, our result reduces back to the open boundaries case. By solving the root equation as a function of λ, we find the CGF plotted in Fig. 3.2a). The main difference seen in the CGF from the open boundaries case is that there has to be negative CGF values for negative λ to give a nonzero average density in the distribution shown in Fig. 3.2b) which is obtained by the Legendre transform defined in Eq. 1.71. Also, note that in the distribution of density, it is clear that this distribution is non Gaussian in the tails. However, close to the mean there will be a Gaussian with a variance proportional to the diffusion constant.

We can also calculate the forces to realize these rare density fluctuations which is what we do in the next subsection.

Auxiliary force

The auxiliary force is given by

$$F_\lambda(x) = 2D_{\rm t}\frac{d\ln[\nu_\lambda(x)]}{dx}, \tag{3.28}$$

with the eigenvector written as

$$\nu_\lambda = \begin{cases} \frac{B\cos(k_2 a)}{\exp(k_1(2L-a)+k_1 a)}\left[\exp(k_1(2L+x)-k_1 x)\right] & x < -a \\ B\cos(k_2 x) & -a < x < a. \\ \frac{B\cos(k_2 a)}{\exp(k_1(2L-a)+k_1 a)}\left[\exp(k_1(2L-x)+k_1 x)\right] & x > a \end{cases} \tag{3.29}$$

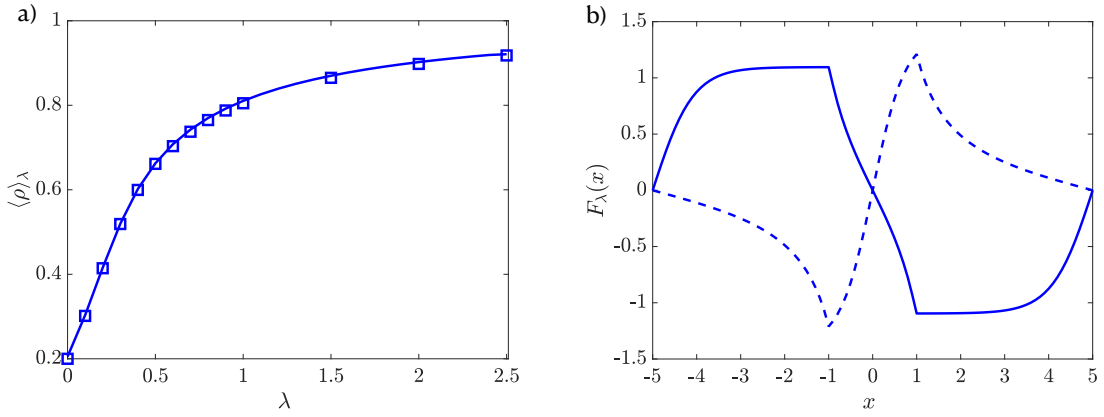

Figure 3.3: Biasing the density. The response of the a) density as a function of λ and b) an example of the control force for $\lambda = 1$ (solid) and -1(dotted). Both a) and b) are with $D_\mathrm{t} = 1/2$, $a = 1$, and $L = 5$.

Inserting the eigenvector we get that

$$F_\lambda(x) = \begin{cases} \sqrt{4D_\mathrm{t}\psi(\lambda)}\tanh(\sqrt{\frac{\psi(\lambda)}{D_\mathrm{t}}}(L+x)) & x < -a \\ -\sqrt{4D_\mathrm{t}(\lambda-\psi(\lambda))}\tanh(\sqrt{\frac{(\lambda-\psi(\lambda))}{D_\mathrm{t}}}x) & -a < x < a. \\ -\sqrt{4D_\mathrm{t}\psi(\lambda)}\tanh(\sqrt{\frac{\psi(\lambda)}{D_\mathrm{t}}}(L-x)) & x > a \end{cases} \tag{3.30}$$

The control force is plotted in Fig. 3.3b) for two lambda values. Note the differences between the open boundaries case in Eq. 3.24. The force within the subsystem is the same but outside the box, the only difference is there is a hyperbolic tangent function that makes the force continuous at the boundaries. This principle will be useful in constructing approximate control forces in cases that are not exactly solvable.

By inserting the force in Eq. 3.30 into the equations of motion and measuring the density observable in Eq. 3.1, we see in Fig. 3.3a) that it agrees well with the exact answer from the first derivative of the CGF shown in Eq. 3.27.

Importance sampling methods

In practice, we can apply the exact force in Eq. 3.30 or an approximate one to importance sample fluctuations in the cloning algorithm [75]. Given that we have a Langevin equation in the Ito convention from Eq. 1.1 as

$$\frac{dx}{dt} = F(x,t) + B(x,t)\zeta(t)\ , \tag{3.31}$$

with a path action of

$$P[X] = \rho(x_0)e^{-\int_0^t \mathcal{L}(x(t),\dot{x}(t))dt} \tag{3.32}$$

with

$$\mathcal{L}(x(t),\dot{x}(t)) = \frac{1}{2}\left[\dot{x} - F(x,t)\right]\left(B(x,t)B(x,t)^T\right)^{-1}\left[\dot{x} - F(x,t)\right]. \tag{3.33}$$

The diffusion coefficient then is defined as

$$D = \frac{B(x,t)B(x,t)^T}{2}, \tag{3.34}$$

We can define a general time integrated density-type observable

$$A_t = \frac{1}{t}\int_0^t a(x(t))dt \tag{3.35}$$

with $a(x(t)) = h(x(t))$ being an indicator function as mentioned above. Within the cloning algorithm we want to calculate the large deviation function by

$$\psi(\lambda) = \frac{1}{t}\ln\left\langle e^{-\lambda A_t}\right\rangle. \tag{3.36}$$

The brackets indicate an ensemble average over the paths generated by Eq. 3.32. If we have the exact solution for the cumulant generating function and its corresponding eigenvector we can use the cloning algorithm with only 1 walker because no branching is needed. When we have an approximate eigenvector and cumulant generating function we can use this to enhance the sampling and decrease the number of walkers needed in the cloning algorithm. Next we will outline the steps to use the approximate guiding force to enhance the sampling. The approximate auxiliary force, $F_\lambda(x)$, is added to the equation of motion of the original system as

$$\frac{dx}{dt} = F(x,t) + F_\lambda(x) + B(x,t)\zeta(t)\ . \tag{3.37}$$

The path action for this dynamics is

$$P_\lambda[X] = \rho(x_0)e^{-\int_0^t \mathcal{L}_\lambda(x(t),\dot{x}(t))dt} \tag{3.38}$$

with

$$\mathcal{L}_\lambda(x(t),\dot{x}(t)) = \frac{1}{2}[\dot{x}(t) - F(x,t) - F_\lambda(x)](B(x,t)B(x,t)^T)^{-1}[\dot{x}(t) - F(x,t) - F_\lambda(x)]. \tag{3.39}$$

However, we want to add a force that helps sample the original dynamics so we must manipulate the action so that we still sample the original distribution. We can rewrite the brackets of the cumulant generating function as

$$\langle\cdots\rangle = \int\cdots dX P[X] = \int\cdots dX P_\lambda[X]\left(\frac{P[X]}{P_\lambda[X]}\right). \tag{3.40}$$

Hence when we add the extra force we add

$$\ln\left(\frac{P[X]}{P_\lambda[X]}\right) = \int \mathcal{L}(x(t),\dot{x}(t)) - \mathcal{L}_\lambda(x(t),\dot{x}(t))dt \tag{3.41}$$

to the weight in the exponential of Eq. 3.36. The weight will only contain terms that contain the guiding force, given by

$$\ln\left(\frac{P[X]}{P_\lambda[X]}\right) = \frac{1}{2B^2}\int |F_\lambda(x)|^2 + 2F(x,t)F_\lambda(x) - 2\dot{x}(t)F_\lambda(x). \tag{3.42}$$

The last term can be re written using Ito's lemma,

$$\frac{dU(x)}{dt} = \dot{x}(t)\frac{dU(x)}{dx} + \frac{B^2}{2}\frac{d^2}{dx^2}U(x), \tag{3.43}$$

and the definition of the auxiliary force as an approximate guiding force (with $F_\lambda = B^2\frac{d}{dx}U_\lambda(x)$),

$$\frac{1}{2B^2}\int -2\dot{x}(t)F_\lambda(x)dt = \int -\dot{x}\frac{d}{dx}U_\lambda(x)dt, \tag{3.44}$$

to be

$$\int -\dot{x}(t)\frac{d}{dx}U_\lambda(x)dt = U_\lambda(x(0)) - U_\lambda(x(t)) + \int \frac{B^2}{2}\frac{d^2}{dx^2}U_\lambda(x_t)dt. \tag{3.45}$$

Using these results for an arbitrary force, the reweighting factor is

$$\ln\left(\frac{P[X]}{P_\lambda[X]}\right) = \frac{1}{2B^2}\int |F_\lambda(x)|^2 + 2F(x,t)F_\lambda(x) + B^4\frac{d^2}{dx^2}U_\lambda(x(t))dt\ , \tag{3.46}$$

with

$$F_\lambda = B^2\frac{d}{dx}U_\lambda(x). \tag{3.47}$$

If the guiding force was the exact auxiliary force($U_\lambda(x) = \ln(\nu_\lambda(x))$ then Eq. 3.45 would be

$$\int -\dot{x}\frac{d}{dx}\ln(\nu_\lambda(x))dt = \ln\left(\frac{\nu_\lambda(x(0))}{\nu_\lambda(x(t))}\right) + \int \frac{B^2}{2}\frac{d^2}{dx^2}\ln(\nu_\lambda(x(t)))dt, \tag{3.48}$$

with $\nu_\lambda(x)$ being the eigenvector of the corresponding CGF. The final expression for the weight in the exact case is

$$\ln\left(\frac{P[X]}{P_\lambda[X]}\right) = \frac{1}{2B^2}\int |F_\lambda(x)|^2 + 2F(x,t)F_\lambda(x) + B^4\frac{d^2}{dx^2}\ln(\nu_\lambda(x(t)))dt. \tag{3.49}$$

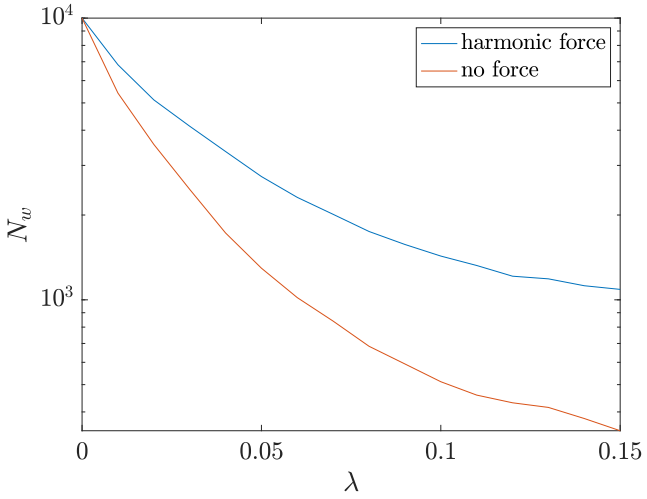

Figure 3.4: Number of walkers as a function of λ with and without an approximate control force. For all λ values studied with $D_t = 1/2$, $a = 1$, $L = 5$, and 10^4 walkers.

Less than optimal control force

We have found the exact force for the brownian walker case. However, many times we cannot calculate this force exactly. In this section, we study how approximate forces to bias the density accelerate the convergence of the cloning algorithm. Based on intuition we expect that a harmonic potential at the center of the square well will lead to faster convergence compared to the results without control forces. Using a harmonic force in the well and a decaying function outside we can write an approximate force as

$$F_\lambda(x) = \begin{cases} \lambda \tanh(L+x) & x < -a \\ -\lambda x & -a < x < a \\ -\lambda \tanh(L-x) & x > a \end{cases} \tag{3.50}$$

The efficiency with and without this approximate control force is shown in Fig. 3.4 which shows better efficiency with walker number for all λ's studied. All of the runs were done with 10^4 walkers. This proves that the force that realizes rare density fluctuations is similar to a harmonic well. This also provides an approximate force we can later apply to interacting active matter systems for better convergence.

In the next section our goal is to use this intuition to understand density bias in active matter.

3.2 Bias on active matter fluctuations

We would like to calculate the CGF for an active particle to be confined to a region of space similar to what we did in the previous section for single Brownian particles. It is intractable to keep both the orientation fluctuations and the Brownian fluctuations, so in this section we study an active Brownian particle in the absence of thermal noise given by

$$\dot{x}(t) = v\,\cos(\theta), \tag{3.51}$$

and

$$\dot{\theta}(t) = \sqrt{2D_{\mathrm{r}}}\eta(t) \tag{3.52}$$

with statistics of $\eta(t)$ having a zero mean and a variance of 1 on average. The tilted generator for this system of equations with a bias on density is

$$L_\lambda = v\,\cos(\theta)\frac{\partial}{\partial x} + D_{\mathrm{r}}\frac{\partial^2}{\partial\theta^2} + \lambda h(x_t). \tag{3.53}$$

Similar to Eq. 3.6, we must solve the eigenvalue equation in the three regions of space,

$$\begin{cases} v\,\cos(\theta)\frac{\partial}{\partial x}\nu_\lambda(x,\theta) + D_{\mathrm{r}}\frac{\partial^2}{\partial\theta^2}\nu_\lambda(x,\theta) - \psi(\lambda)\nu_\lambda(x,\theta) = 0 & x < -a \\ v\,\cos(\theta)\frac{\partial}{\partial x}\nu_\lambda(x,\theta) + D_{\mathrm{r}}\frac{\partial^2}{\partial\theta^2}\nu_\lambda(x,\theta) - (\psi(\lambda) - \lambda)\,\nu_\lambda(x,\theta) = 0 & -a \le x \le a \\ v\,\cos(\theta)\frac{\partial}{\partial x}\nu_\lambda(x,\theta) + D_{\mathrm{r}}\frac{\partial^2}{\partial\theta^2}\nu_\lambda(x,\theta) - \psi(\lambda)\nu_\lambda(x,\theta) = 0 & x > a \end{cases} \tag{3.54}$$

We can solve these equations by separation of variables,

$$\nu_\lambda(x,\theta) = \rho(x)f(\theta), \tag{3.55}$$

which gives us

$$\frac{\partial_x\rho(x)}{\rho(x)} = \frac{-D_{\mathrm{r}}}{v\cos(\theta)f(\theta)}\left[\partial_\theta^2 f(\theta) - \frac{mf(\theta)}{D_{\mathrm{r}}}\right] = -g \tag{3.56}$$

where g is a constant to be determined and the variable m is equal to $\psi(\lambda)$ outside of the subsystem and equal to $(\psi(\lambda) - \lambda)$ inside the the subsystem. This gives two equations to solve for the two eigenfunctions for space and orientation which are

$$\partial_x\rho(x) = -g\rho(x), \tag{3.57}$$

and

$$\partial_\theta^2 f(\theta) - \frac{mf(\theta)}{D_{\mathrm{r}}} = \frac{g\ v\cos(\theta)f(\theta)}{D_{\mathrm{r}}}. \tag{3.58}$$

The equation for the density will just be exponential like in the previous section. However, to find the value for g we must solve the differential equation for θ. The solution is just Mathieu's equation. Hence, the value for g is found from

$$\frac{4m}{D_{\mathrm{r}}} = a_0(\frac{2gv}{D_{\mathrm{r}}}), \tag{3.59}$$

where $a_o(x)$ is the zeroth order eigenvalue of Mathieu's equation. This is a common procedure in sedimentation papers [117, 118, 119]. By inverting this equation we get to leading order in g that

$$g = \pm\sqrt{\frac{m}{D}}, \tag{3.60}$$

where

$$D = \frac{v^2}{2D_{\mathrm{r}}}. \tag{3.61}$$

Note that the solution for g is only approximate since the solution is an infinite series in g and we have only taken the leading order term which is quadratic. Analytically, it is also possible to solve for g at fourth order for more precise estimates. On the other hand, numerically it is possible to solve for g to arbitrary order to get an exact estimate for g by using a basis set expansion [25].

By putting our value of g back into the the position eigenvalue equation, we get the same equations as for the Brownian particle as

$$\nu_\lambda(x) = \begin{cases} Ae^{k_1 x} + Ee^{-k_1 x} & x < -a \\ B\cos(k_2 x) + C\sin(k_2 x) & -a \le x \le a \\ De^{-k_1 x} + Fe^{+k_1 x} & x > a \end{cases} \tag{3.62}$$

with the coefficients being

$$k_1^2 = \frac{\psi(\lambda)}{D}\ , \tag{3.63}$$

and

$$k_2^2 = \frac{[\lambda - \psi(\lambda)]}{D}. \tag{3.64}$$

We see that the solution for the time integrated density is identical to the Brownian particles solution in Eq. 3.27,

$$\frac{k_1}{k_2} = \frac{\tan(k_2 a)}{\tanh\left[k_1\left(L-a\right)\right]} = \sqrt{\frac{\lambda}{\lambda - \psi(\lambda)} - 1}, \tag{3.65}$$

but with a modified diffusion coefficient. In practice, it would be a small step to assume that thermal fluctuations could be put back in by using the diffusion constant of

$$\mathcal{D} = D_{\mathrm{t}} + \frac{v^2}{2D_{\mathrm{r}}}. \tag{3.66}$$

This follows from the fact that we have proven that the solution only changes the magnitude of the diffusion in the exponential solution. The CGF compared to simulations is shown

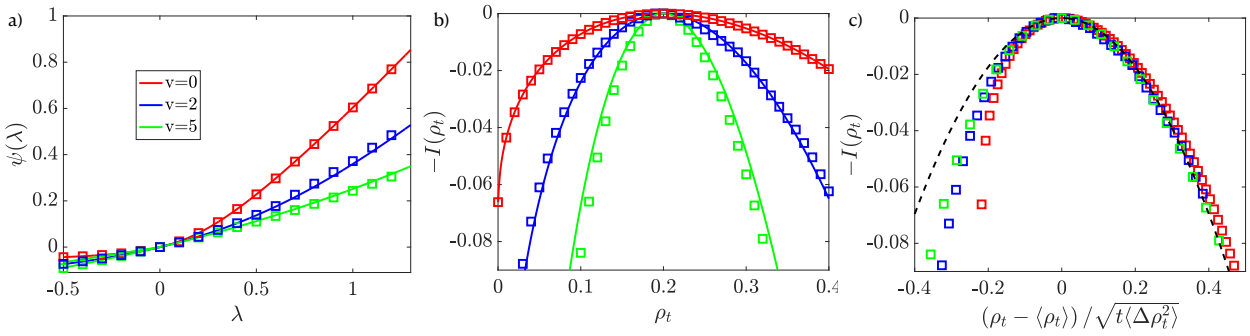

Figure 3.5: Density fluctuations as a function of self-propulsion. a) The cumulant generating function for $v = 0, 2, 5$ and b) the rate function for the same self-propulsion values with the solid lines representing the predictions and the symbols showing cloning results. c) the same data in b) but with the x-axis shifted by the mean and scaled by the variance to highlight non-Gaussian fluctuations. The black dotted line shows a fitted Gaussian distribution. All data is with $D_\mathrm{t} = 0.5$, $D_\mathrm{r} = 3$, and $a/L = 0.2$.

in Fig. 3.5a) which shows good agreement for a few different self-propulsion values. The corresponding rate function of density fluctuations is shown in Fig. 3.5b). We see that increasing self-propulsion causes a decrease in the variance. This comes from the fact that in Eq. 3.22 increasing the diffusion constant causes the CGF to have a lesser value for a corresponding λ and creates smaller fluctuates with increasing self-propulsion.

In Fig. 3.5c), the data in Fig. 3.5b) is re-plotted but with the x-axis shifted by the mean and scaled by the square root of the variance to highlight deviations from a Gaussian distribution shown by the dotted line. It is seen that the the distributions become more Gaussian with increasing self-propulsion. This is because distributions become non-Gaussian for fluctuations close to a zero density which becomes increasingly improbable with increasing propulsion.

3.3 Dynamical density fluctuations in interacting active matter

We have only considered non-interacting systems thus far. Based on our intuition from those examples we would like study interacting active matter in 2 dimensions. We would expect any system that has a steady state phase transition would also have a dynamical phase transition. However, the precise nature in which adding time changes the statistics has not been studied before.

Before we discuss the dynamical density fluctuations in interacting active matter. We will first show why we know from theory that there is a phase transition in this nonequilibrium system.

Linear instability analysis

We can show that there is a dynamical instability in the dynamics by noting that the continuity equation for a tagged active particle, from the adjoint of Eq. 2.12 evaluated at $\lambda = 0$, is

$$\frac{\partial \rho(\boldsymbol{r},\theta,t)}{\partial t} = -\nabla \cdot [V_0(\rho)\boldsymbol{b}(\theta)\rho(\boldsymbol{r},\theta,t)] + D_{\mathrm{t}}(\rho)\nabla^2\rho(\boldsymbol{r},\theta,t) + D_{\mathrm{r}}\partial_\theta^2\rho(\boldsymbol{r},\theta,t). \tag{3.67}$$

We introduce the mass density and polarization to be

$$\rho(\boldsymbol{r},t) = \int \rho(\boldsymbol{r},\theta,t)d\theta, \tag{3.68}$$

and

$$\boldsymbol{p}(\boldsymbol{r},t) = \int \boldsymbol{b}(\theta)\rho(\boldsymbol{r},\theta,t)d\theta. \tag{3.69}$$

Combining Eqs. 3.67-3.69, we find that the equations of motion for the mass density and polarization are

$$\frac{\partial \rho(\boldsymbol{r},t)}{\partial t} = -\nabla \cdot [V_0(\rho)\boldsymbol{p}(\boldsymbol{r},t)] + D_{\mathrm{t}}(\rho)\nabla^2\rho(\boldsymbol{r},t), \tag{3.70}$$

and

$$\frac{\partial \boldsymbol{p}(\boldsymbol{r},t)}{\partial t} = -\nabla\frac{V_0(\rho)\rho(\boldsymbol{r},t)}{2} + D_{\mathrm{t}}(\rho)\nabla^2\boldsymbol{p}(\boldsymbol{r},t) - D_{\mathrm{r}}\boldsymbol{p}(\boldsymbol{r},t). \tag{3.71}$$

These equation of motion ignore higher order orientation fields in order to have a closed set of equations [6]. We can consider dynamical fluctuations from the homogeneous density profile by defining a mean and a linear fluctuation term as

$$\rho(\boldsymbol{r},t) = \bar{\rho} + \delta\rho(\boldsymbol{r},t). \tag{3.72}$$

The polarization is zero on average for this system so a nonzero polarization would result from a dynamical fluctuation. By inserting solutions of the form

$$\boldsymbol{p}, \delta\rho = e^{\sigma(k)t + i\boldsymbol{k}\cdot\boldsymbol{r}} \tag{3.73}$$

into Eqs. 3.70 and 3.71, we get a dispersion of

$$\sigma(k) = -\frac{1}{2} - D_{\mathrm{t}}(\rho)k^2 + \frac{1}{2}\sqrt{1 - 2\left(v - \bar{\rho}\zeta\right)\left(v - 2\bar{\rho}\zeta\right)k^2}. \tag{3.74}$$

This equation quantifies the growth rate from a perturbation. There are fluctuations as a function of k that cause the dispersion to be positive which denotes a fluctuation will not decay and continue to grow leading to a dynamical instability.

Phase separated systems

We now consider a modified density observable to be

$$\rho_{a,t} = \frac{1}{4a^2 t} \int \sum_{i=1}^{N} h(\boldsymbol{r_i}(t)) dt \tag{3.75}$$

which is similar to Eq. 3.1 in that it is time integrated but now the average density is set by the number of particles in the subvolume at an instance in time, $\bar{\rho}_a = \frac{N_a}{4a^2}$, where the subsystem still has dimensions of $2a$. This defines the number of particles in the subsystem at time t to be

$$N_a = \sum_{i=1}^{N} h(\boldsymbol{r_i}(t)). \tag{3.76}$$

For a homogeneous system the density within the subsystem will be the same as the total system

$$\bar{\rho}_a = \bar{\rho}. \tag{3.77}$$

The CGF cloning is plotted in Fig. 3.6 for various subsystem sizes, $a = 2$, 3, and 4, at the state points $v = 120$ and $\rho = 0.25$. To obtain points in Fig. 3.6a), $N_w = 10^3 - 10^7$ walkers was used. These state points would be phase separated in the infinite time limit but a nucleation event would take a prohibitively long time to happen. The complete system including the bath has N=400-600 particles depending on the system size with square box dimensions to give the bulk density of $\bar{\rho} = 0.25$. All results are with an observation time of $t = 5\Delta t$, a rotational diffusion constant of $D_\mathrm{r} = 3$, and a translational diffusion constant of $D_\mathrm{t} = 0.5$.

In Fig. 3.6a), the critical λ, λ_c, is at the point at which the curvature of the CGF changes. The critical lambda moves closer to zero as the size of the subsystem grows. In Fig 3.6b), the distributions for various subsystem sizes are plotted. There are clear finite size effects with the dense phase becoming more probable with increasing system size. In the thermodynamic limit, we expect the dilute phase to still be more probable since the state point is closer to the dilute phase of MIPS. At a phase point that is directly equidistant from both the dense and dilute phases we would expect equal probable dynamical phases but that is not what is studied here.

From the distribution in Fig. 3.6b), we can calculate the average density as a function of λ by

$$\langle \rho \rangle_\lambda = \int \rho \; e^{-4a^2 t[I(\rho)+\lambda\rho]} d\rho. \tag{3.78}$$

Similarly, the fluctuations can be calculated by a derivative of the λ dependent density with respect to λ,

$$4a^2 \langle (\delta\rho)^2 \rangle_\lambda \sigma^2 = \sigma^2 \frac{\langle \rho \rangle_\lambda}{d\lambda}. \tag{3.79}$$

Both the average and the variance is plotted in Fig. 3.7. The inset of Fig. 3.7b) shows scaling consistent with a first order dynamical phase transition with a critical lambda that

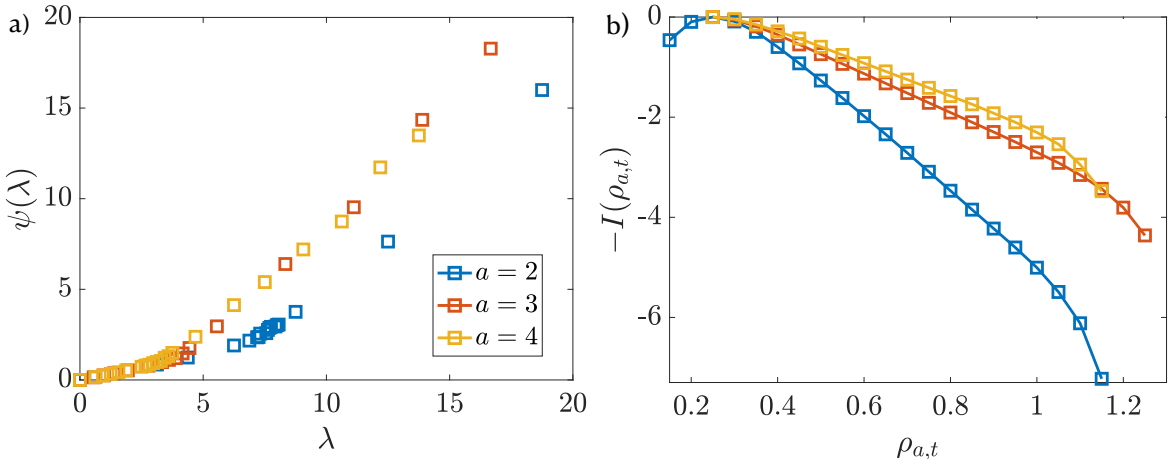

Figure 3.6: Large deviation functions for interacting active matter at the state point of $v = 120$ and $\rho = 0.25$. a) The CGF and b) the rate function as a function of subsystem sizes of 4×2^2, 4×3^2, and 4×4^2.

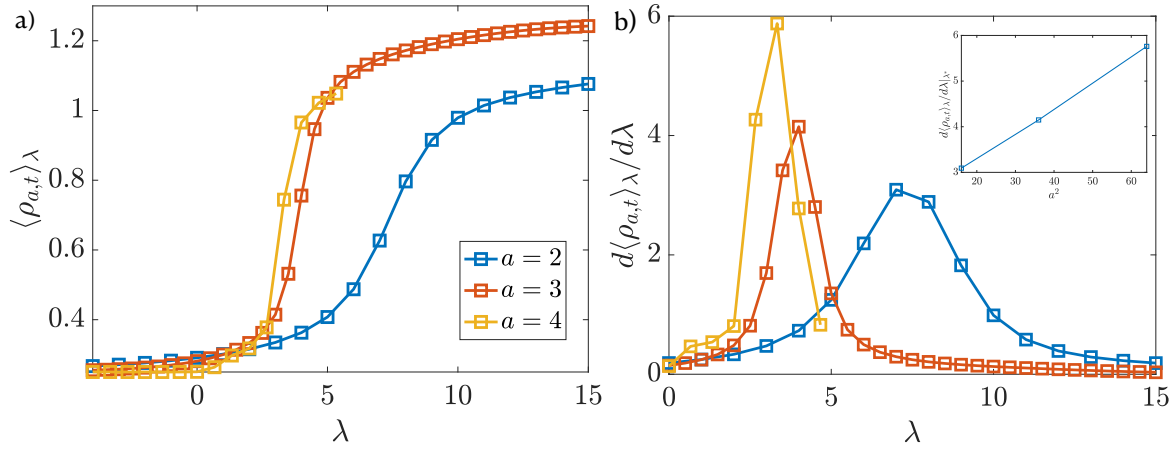

Figure 3.7: The response of the a) density as a function of λ and b) the size intensive variance showing a peak growing with size and becoming narrower. The inset shows the scaling of the peak height with probe area.

scales linearly with system size. The two density phases in Fig. 3.7a) are close to those measured in MIPS [114].

Future works will try to derive an approximate CGF and control forces for 2D interacting homogeneous systems. There are ways to map 2 dimensional circular wells to a pseudo 1 dimensional problem when there is no angular momentum in quantum mechanics. This may provide insight into this study. We would also like to understand the differences between the crystallization transition which does not rely on motility to happen, MIPS which does, and how motility changes the crystallization transition [120]. Another interesting avenue is seeing if there are universal bounds on density fluctuations just as there are for current fluctuations [40].

Chapter 4

Energy dissipation and self-assembly

introduction

This section mainly consists of my work in [42].

The active matter systems considered are away from equilibrium due to non-conservative forces that generate self-propulsion. The constant energy dissipation is associated with the entropy production and is deeply connected to their dynamic and structural properties [121, 122, 123, 124, 125, 126, 127, 128, 96, 129].

Additionally, by understanding the different sources of entropy production in active matter will lead the way in manipulating their collective behavior [130, 131, 132, 133, 134, 135, 136, 137, 138], designing active metamaterials with novel responses [139, 140, 141, 142], and building active heat engines [143, 144, 145, 146, 147, 148, 149].

Stochastic thermodynamics provides a framework for studying entropy production and has supplied general theories that constrain its statistics [37, 35, 38, 46, 150] and its role in nonequilbrium response [102, 103, 104, 47, 105, 106, 107, 151, 152, 108, 109, 110, 111, 153, 112]. Here, we provide a general bound on the distributions of entropy production for interacting active matter using stochastic thermodynamics and large deviation theory [8]. While not as universal as the thermodynamic uncertainty principle [39, 154], the specific consideration of active matter admits a bound that in some cases is tighter, and one in which deviations can be physically understood. The bound we present is valid arbitrarily far from equilibrium for self-propelled particles and is saturated in the limit that the interparticle contribution to the entropy production is small. Near phase transitions, the bound is weak as fluctuations are enhanced due to emergent effective long-ranged interactions that we quantify. This work provides a link between entropy production fluctuations and collective phenomena in active matter and ways to control them.

All of the active matter considered are of the form

$$\dot{\boldsymbol{r}}_i = v\,\boldsymbol{b}_i + \mu \boldsymbol{F}_i\left(\boldsymbol{r}^N\right) + \sqrt{2D_{\mathrm{t}}}\boldsymbol{\eta}_i \ , \tag{4.1}$$

where $\boldsymbol{r}_i$ denotes the position of the ith particle, v and $\boldsymbol{b}_i$ set the typical magnitude and direction of self-propulsion, μ is a single particle mobility, and $\boldsymbol{\eta}_i$ is a Gaussian white noise

with $\langle \eta_i^\alpha(t) \rangle = 0$ and $\langle \eta_i^\alpha(t) \eta_j^\beta(t') \rangle = \delta_{ij}\delta_{\alpha,\beta}\delta(t-t')$ for the α and β components of the random force. The translational diffusion coefficient, D_t, satisfies a fluctuation-dissipation relation, $D_\mathrm{t} = \beta^{-1}\mu$ where β^{-1} is the temperature times Boltzmann's constant. Throughout, we take $\mu = D_\mathrm{t} = 1$. The interparticle forces are conservative, $\boldsymbol{F}(\boldsymbol{r}^N) = -\nabla U(\boldsymbol{r}^N)$, and in general depend on all N particles' positions, $\boldsymbol{r}^N$. This class of active matter has a non-conservative self-propulsion term, $v\boldsymbol{b}$, which is driven by a constant energy supply. Our formulation is independent of the statistics and dynamics of the self propulsion vector, $\boldsymbol{b}$, and may be correlated due to aligning interactions. The dynamics of the orientation vector $\boldsymbol{b}$ are model specific discussed in the next section but our results are largely independent of its form. For concreteness, below we will consider collections of interacting active Brownian particles (ABPs), active dumbbells (ADPs), run and tumble particles (RTPs), and active Ornstein-Uhlenbeck particles (AOUPs).

4.1 Form of the active force

ABPs and RTPs

For both ABPs and RTPs the orientation vector has a fixed magnitude, so in two dimensions it can be uniquely parameterized by an angle θ. For the ith particle, $\boldsymbol{b_i} = \{\cos(\theta_i)\hat{\boldsymbol{x}}_i, \sin(\theta_i)\hat{\boldsymbol{y}}_i\}$, where $\hat{\boldsymbol{x}}_i$ and $\hat{\boldsymbol{y}}_i$ are the unit vectors in the x and y directions, respectively. For ABPs, the dynamics of θ_i are Brownian,

$$\dot{\theta}_i(t) = \eta_i^\theta(t) \tag{4.2}$$

where η_i^θ is a Gaussian white noise, satisfying $\langle \eta_i^\theta(t) \rangle = 0$ and $\langle \eta_i^\theta(t) \eta_j^\theta(t') \rangle = 2D_\mathrm{r}\delta_{ij}\delta(t-t')$ with D_r being the rotational diffusion constant. We take $D_\mathrm{r} = 3D_\mathrm{t}/\sigma^2$ throughout the main text.

The dynamics of θ for RTPs are piecewise constant over waiting times, τ, satisfying a Poisson process [82, 155]. The waiting time distribution is given by an exponential distribution,

$$P(\tau) = \gamma e^{-\gamma\tau}, \tag{4.3}$$

with constant reorientation rate γ. We take $\gamma = D_\mathrm{t}/\sigma^2$. At each τ, the particles reorient by drawing a new θ chosen uniformly over the range $[0, 2\pi]$.

ADPs

Each ADP is composed of two particles that are tethered together by a harmonic bond. The additional harmonic bond potential is given by $U_\mathrm{H}(r) = k(r-l)^2/2$, where k is the spring constant, l is the rest length, and r is the displacement between the two bonded particles. In the main text, we take $k = 100\ \epsilon/\sigma^2$ and $l = 1.5\ \sigma$. The self-propulsion direction is along the bond vector. For the ith ADP, composed of monomers 1 and 2, $\boldsymbol{b}_i = \hat{\boldsymbol{r}}_{i,12}$ where $\hat{\boldsymbol{r}}_{i,12}$ is the unit displacement vector between monomers 1 and 2. The time evolution of the orientation

vector is given by the time evolution of the displacement vector between the two composite particles as dictated by their individual equations of motion [156, 157].

AOUPs

For AOUPs, the self propulsion vector changes both its magnitude and direction. Its equation of motion is of the form of an Ornstein-Uhlenbeck process and given by

$$\dot{\boldsymbol{b}}_{\boldsymbol{i}} = -D_{\mathrm{r}}\boldsymbol{b}_i + \boldsymbol{\xi}_{\boldsymbol{i}} \tag{4.4}$$

where $\boldsymbol{\xi}_{\boldsymbol{i}}$ is a Gaussian random variable which has a zero mean, $\langle \xi_{i,\alpha}(t)\rangle = 0$, and a variance of $\langle \xi_i^{\alpha}(t)\xi_j^{\beta}(t')\rangle = 2D_{\mathrm{a}}D_{\mathrm{r}}^2/v^2\delta_{ij}\delta_{\alpha,\beta}\delta(t-t')$ for each α,β component and D_{a} sets the scale of fluctuations in the magnitude of $\dot{\boldsymbol{b}}_{\boldsymbol{i}}$ [96, 111]. We take $D_{\mathrm{r}} = D_{\mathrm{t}}/\sigma^2$, $v = \sqrt{2D_{\mathrm{a}}D_{\mathrm{r}}}$, and study a range of D_{a}'s.

4.2 Derivation of entropy production

The entropy production is derived from time reversal symmetry properties of the path action in stochastic thermodynamics [158, 36, 159, 160, 161], $\Delta S = \ln P[\Gamma]/P[\tilde{\Gamma}]$, where $P[\Gamma]$ is the probability of a forward trajectory $\Gamma = \{\boldsymbol{r}^N(t), \boldsymbol{b}^N(t)\}$ and $P[\tilde{\Gamma}]$ is the probability of observing the time-reversed trajectory.

Without a specific source for how the self-propulsion arises, we use the convention that the parameter v is even under time-reversal which agrees with previous work [162, 163, 164, 165, 166]. Within this convention, non-interacting particles have an entropy production that is proportional to their propulsion squared, v^2. The choice of convention for time reversal without an underlying microscopic model of self-propulsion is somewhat arbitrary [167]. However, all of the collective phenomena reported below are independent of the convention [168]. The convention we follow is analogous to the active work [164] and can be derived independently from mechanical considerations.

ABPs

The probability of observing a path for a system of ABPs with conservative interactions in the Stratonovich convention ($\alpha = 1/2$ in Eq. 3.32) is

$$P[\Gamma] \propto \exp\left[-\sum_{i=1}^{N}\int_0^t dt' \, \frac{\left(\dot{\boldsymbol{r}}_i - v\,\boldsymbol{b}_i - \mu\boldsymbol{F}_i\left(\boldsymbol{r}^N\right)\right)^2}{4D_{\mathrm{t}}} + \frac{\boldsymbol{\nabla}_{\boldsymbol{r}_i}\cdot\left(\mu\boldsymbol{F}_i\left(\boldsymbol{r}^N\right)\right)}{2} + \frac{\dot{\boldsymbol{b}}_i^2}{4D_{\mathrm{r}}}\right], \tag{4.5}$$

where the gradient term in the second line follows from the Stratonovich convention. After performing the time reversal operation and taking a ratio of path probabilities, the entropy

production then becomes

$$\Delta S = \frac{1}{D_{\rm t}} \sum_{i=1}^{N} \int_0^t dt' \, \left[v \, \boldsymbol{b}_i \circ \dot{\mathbf{r}}_i(t') + \dot{\mathbf{r}}_i \circ \mu \boldsymbol{F}_i \left(\boldsymbol{r}^N \right) \right] \quad , \tag{4.6}$$

which is a sum of two terms. However, since we are using the Stratonovich convention the chain rule is preserved and the term

$$\sum_{i=1}^{N} \int_0^t dt' \dot{\mathbf{r}}_i \circ \boldsymbol{F}_i \left(\boldsymbol{r}^N \right) = U(\boldsymbol{r}^{\boldsymbol{N}}(0)) - U(\boldsymbol{r}^{\boldsymbol{N}}(t)) \ , \tag{4.7}$$

does not grow with time, unlike the first term. In the long time limit it will become negligible, and can be neglected in the entropy production.

AOUPs

For AOUPS using the Stratonovich convention, the derivation of the form of the entropy production follows similarly as for the other models. Specifically, the path probability is

$$P[\Gamma] \propto \exp \Bigg[- \sum_{i=1}^{N} \int_0^t dt' \frac{\left(\dot{\boldsymbol{r}}_i - v \, \boldsymbol{b}_i - \mu \boldsymbol{F}_i \left(\boldsymbol{r}^N \right) \right)^2}{4 D_{\rm t}} + \frac{\boldsymbol{\nabla}_{\boldsymbol{r}_i} \cdot \left(\mu \boldsymbol{F}_i \left(\boldsymbol{r}^N \right) \right)}{2} + \frac{v^{\,2} \left(\dot{\boldsymbol{b}}_i + D_{\rm r} \boldsymbol{b}_i \right)^2}{4 D_{\rm a} D_{\rm r}^2} - \frac{\boldsymbol{\nabla}_{\boldsymbol{b}_i} \cdot D_{\rm r} \boldsymbol{b}_i}{2} \Bigg] , \tag{4.8}$$

where the additional force on $\boldsymbol{b}_i$ results in the last two terms. After performing the time reversal operation, the entropy production is

$$\Delta S = \sum_{i=1}^{N} \int_0^t dt' \left(\frac{v \, \boldsymbol{b}_i \circ \dot{\mathbf{r}}_i}{D_{\rm t}} + \frac{\dot{\mathbf{r}}_i \circ \mu \boldsymbol{F}_i \left(\boldsymbol{r}^N \right)}{D_{\rm t}} - \frac{v^{\,2} \dot{\boldsymbol{b}}_i \circ \boldsymbol{b}_i}{D_{\rm a} D_{\rm r}} \right) , \tag{4.9}$$

where the first two terms are analogous to the ABPs. Both the second term and third term do not grow with time, and so in the long time limit the entropy production reduces to

$$\Delta S = \frac{v}{D_{\rm t}} \sum_{i=1}^{N} \int_0^t dt' \ \boldsymbol{b}_i \circ \dot{\boldsymbol{r}}_i \ , \tag{4.10}$$

which is equivalent to the form found for the ABPs.

4.3 Bound on entropy production fluctuations

As shown in the previous section all models, under an even time reversal for the self-propulsion term, have the same form for entropy production as

$$\Delta S = \frac{v}{D_{\mathrm{t}}} \sum_{i=1}^{N} \int_0^t dt' \; \boldsymbol{b}_i \circ \dot{\boldsymbol{r}}_i \quad . \tag{4.11}$$

For the time and system size intensive entropy production, $s = \Delta S/(Nt)$, the CGF is defined as,

$$\psi(\lambda) = \frac{1}{tN} \ln \left\langle e^{\lambda s(\Gamma) Nt} \right\rangle_0 , \tag{4.12}$$

where $\langle \dots \rangle_0$ denotes average over paths and λ is the counting variable that probes rare fluctuations of the entropy production when nonzero. Cumulants of the entropy production are computable from $\psi(\lambda)$ through derivatives with respect to λ.

Calculating $\psi(\lambda)$ or $I(s)$ exactly for interacting systems is difficult because of many-body correlations. However, we find that $\psi(\lambda)$ can generally be rewritten by factoring out the single particle part,

$$\psi(\lambda) = \psi_f(\lambda) + \frac{1}{Nt} \ln \left\langle e^{\lambda \Delta W} \right\rangle_{\boldsymbol{u}_\lambda} \quad , \tag{4.13}$$

where $\psi_f(\lambda)$ is the CGF for an isolated active particle. The remaining contribution to $\psi(\lambda)$ represents interparticle correlations and is given by the CGF of

$$\Delta W = \beta v \sum_{i=1}^{N} \int_0^t dt' \; \boldsymbol{b}_i \cdot \boldsymbol{F}_i \; , \tag{4.14}$$

averaged over an ensemble with an additional force $\boldsymbol{u}_\lambda$. The force $\boldsymbol{u}_\lambda$ is the optimal control force to realize rare entropy production fluctuations for an isolated particle and its model specific form is considered below. The observable ΔW is the dimensionless work done on the surrounding particles due to self-propulsion. By applying Jensen's inequality to Eq. 4.13,

$$\psi(\lambda) \geq \psi_f(\lambda) + \beta \lambda v \left\langle \boldsymbol{b} \cdot \boldsymbol{F} \right\rangle_{\boldsymbol{u}_\lambda} \quad , \tag{4.15}$$

$\psi(\lambda)$ is bounded (see section 4.4). The correction over the single particle CGF can be interpreted as $\beta\lambda v$ times the effective drag a tagged particle feels in the direction of the self-propulsion due to the surrounding particles [6]. This is the same friction introduced in the context of current fluctuations in chapter 2. This gives rise to an effective velocity that is smaller than v and dependent on the density and λ [25].

Inserting the bound on the CGF in Eq. 4.15 into the Legendre-Fenchel transform, we derive a bound on the distribution of the entropy production, $I_b(s)$,

$$I(s) \leq I_b(s) = \max_{\lambda} \left[\lambda s - \psi_f(\lambda) - \beta \lambda v \left\langle \boldsymbol{b} \cdot \boldsymbol{F} \right\rangle_{\boldsymbol{u}_\lambda} \right] . \tag{4.16}$$

By construction the bound recovers the correct mean dissipation and is tight far into the tails of the distribution in the limit that fluctuations in ΔW are small and the saddle point approximation to its CGF is accurate. Data in Fig. 4.1 confirms the upper bound for all of the active matter models studied. Throughout, $I(s)$ is computed using the cloning algorithm [169, 75] and $I_b(s)$ by computing $\langle \Delta W \rangle_{\boldsymbol{u}_\lambda}$ from direct simulations. All simulations are done with a WCA interparticle potential [66], $U(r) = 4\epsilon\left[\left(\frac{\sigma}{r}\right)^{12} - \left(\frac{\sigma}{r}\right)^{6}\right] + \epsilon$ for $r \leq 2^{1/6}\sigma$ and zero otherwise. The parameter ϵ is the energy scale of the interactions and σ is the particle diameter. ADPs have an added harmonic potential between composite particles. Our results are presented with a non-dimensional v in units of D_t/σ, γ and D_r in units of D_t/σ^2, and bulk density ρ in units of $1/\sigma^2$ in two dimensions. Also, D_t, and β are set to 1. Data in Fig. 4.1a shows that there are large parameter regimes where the bound is tight. In practice, the bound is accurate when the system is away from dynamical phase transitions, this is valid when $\rho(v/D_\mathrm{r})^2 < 1$. Nevertheless, even when $\rho(v/D_\mathrm{r})^2 \approx 1$ we find the bound is still reasonably tight.

The detailed forms for $I(s)$ and $I_b(s)$ are distinct for different models of active matter. For ABPs, ADPs, and RTPs, the entropy production fluctuations are Gaussian for isolated particles, with $\psi_f(\lambda) = v^2\lambda(1+\lambda)/D_\mathrm{t}$ (see section 4.4). The corresponding control force, $\boldsymbol{u}_\lambda = 2\lambda v\boldsymbol{b}$, is appended to the existing forces in Eq. 4.29 such that rare entropy production fluctuations are realized by a renormalized velocity, $v_\lambda = v(1+2\lambda)$. This $\psi_f(\lambda)$ gives rise to a bound that is nearly Gaussian, as shown in Fig. 4.1b. For low densities and low velocities, $I(s) \approx I_b(s)$. Increasing v, the bound weakens for smaller than average entropy production fluctuations, $s < \langle s \rangle_0$. Fluctuations that result in larger than average entropy production, $s > \langle s \rangle_0$, for large v are more probable than predicted by the bound due to neglecting contributions from interparticle correlations. However, the relative error between the entropy production distribution and the bound decreases into the tails due to the increasingly independent particle behavior elaborated upon below.

For isolated AOUPs, the entropy production fluctuations are generically non-Gaussian and $\psi_f(\lambda) = D_\mathrm{r}\left(1 - \sqrt{1 - 2v^2\lambda(1+\lambda)/D_\mathrm{t}D_\mathrm{r}}\right)$, where D_r is the rotational diffusion constant (see Appendix 4.4). The fluctuations in s are Gaussian only near the mean and are asymmetric [164]. This is in contrast to the Gaussian distribution that would be predicted by the thermodynamic uncertainty relations, and reflects the finite memory in the self-propulsion vector. In this case, with specific consideration to the details of the system we obtain a tighter bound. The control force includes the same renormalized velocity as for ABPs, but in addition includes a force on the particle's orientation, $\boldsymbol{u}_\lambda = \psi_f(\lambda)\boldsymbol{b}$ which modulates the self propulsion speed. In Fig. 4.1c, we see that the bound gives an accurate prediction of the fluctuations across the densities and v's considered. The fluctuations are still enhanced relative to the bound for $s < \langle s \rangle_0$, though less so than in Fig. 4.1b.

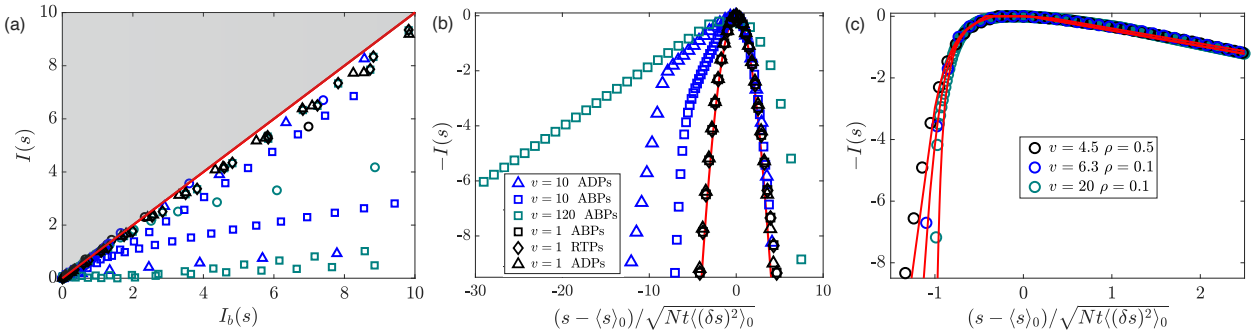

Figure 4.1: Entropy production fluctuations for a variety of active matter systems. (a) Rate function obtained by importance sampling versus the bound in Eq. 4.16 with the symbols corresponding to the labels in (b) and (c). (b) Entropy production fluctuations for $\rho = 0.1$, ABPs with $D_{\mathrm{r}} = 3$, ADPs with spring constant $k = 100\ \epsilon/\sigma^2$ and rest length $l = 1.5\sigma$, and RTPs with a tumble rate $\gamma = 1$ for different self-propulsion values. (c) Entropy production fluctuations for AOUPs for different parameter ranges and $D_{\mathrm{r}} = 1$. In all panels the red line denotes $I_b(s)$ and the errorbars are smaller than the symbols.

4.4 Free particle CGFs, optimal control forces, and bound derivation

The bound in the previous section relies on knowing the non-interacting CGF for entropy production. In this section, it is detailed how this is calculated. The free particle CGF is computable from the solution of a generalized eigenvalue equation of the form

$$L_\lambda \nu_\lambda = \psi_f(\lambda)\nu_\lambda \ , \tag{4.17}$$

where L_λ is the Lebowitz-Spohn, or tilted, operator and ν_λ and $\psi_f(\lambda)$ are the maximum eigenvector eigenvalue pair. The tilted operator is derivable from the time evolution of the CGF and the relation to the spectrum of L_λ and the CGF follows from the long time limit. Generically, for a current-type variable [158, 8] the optimal control force that realizes rare entropy production fluctuation is given by

$$\boldsymbol{u}_\lambda = 2\lambda v \boldsymbol{b} + 2\boldsymbol{D} \cdot \nabla \ln \nu_\lambda \ , \tag{4.18}$$

where $\boldsymbol{D}$ is a matrix of diffusion constants in define in space crossed with the self-propulsion vector dimension and $\nabla = \{\nabla_{\boldsymbol{r}}, \nabla_{\boldsymbol{b}}\}$. The optimal control force is encoded in the maximum eigenvector associated with L_λ [8].

In order to fully solve the eigenspectrum it is necessary to solve the eigenvalue problem for the adjoint tilted operator [170]

$$L_\lambda^\dagger q_\lambda = \psi_f(\lambda) q_\lambda \ . \tag{4.19}$$

since in general L_λ is not Hermitian. The boundary conditions of the eigevectors must obey a normalization boundary condition $\nu_\lambda(\boldsymbol{b})q_\lambda(\boldsymbol{b}) \to 0$ as $b \to \infty$ [170]. The boundary condition can equivalently be written as

$$\int d\boldsymbol{b}\; q_\lambda(\boldsymbol{b})\nu_\lambda(\boldsymbol{b}) = 1, \tag{4.20}$$

and for convenience we impose that

$$\int d\boldsymbol{b}\; q_\lambda(\boldsymbol{b}) = 1. \tag{4.21}$$

ABPs

The tilted generator for the entropy production of an isolated ABP is

$$L_\lambda = v\,\boldsymbol{b}\cdot\left[\nabla_{\boldsymbol{r}} + \lambda\frac{v\,\boldsymbol{b}}{D_\mathrm{t}}\right] + D_\mathrm{t}\left[\nabla_{\boldsymbol{r}} + \lambda\frac{v\,\boldsymbol{b}}{D_\mathrm{t}}\right]\cdot\left[\nabla_{\boldsymbol{r}} + \lambda\frac{v\,\boldsymbol{b}}{D_\mathrm{t}}\right] + \boldsymbol{\nabla}_{\boldsymbol{b}}^2 D_\mathrm{r}\ ,$$

which can be solved on a periodic domain by a constant eigenvector, $\nu_\lambda = \text{const}$. This is equivalent to assuming that the stationary state is uniform and isotropic for all λ. The CGF follows by noting $\boldsymbol{b}\cdot\boldsymbol{b} = 1$ and is

$$\psi_f(\lambda) = \lambda\frac{v^2}{D_\mathrm{t}} + \lambda^2\frac{v^2}{D_\mathrm{t}}\ , \tag{4.22}$$

and that the control force that realizes the rare dynamics reduces to $\boldsymbol{u}_\lambda = 2\lambda v\,\boldsymbol{b}$. The corresponding equation of motion is

$$\dot{\boldsymbol{r}}_i = v\,(1+2\lambda)\;\boldsymbol{b}_i + \sqrt{2D_\mathrm{t}}\boldsymbol{\eta}_i\ , \tag{4.23}$$

where we see explicitly that the control force acts to renormalize the self-propulsion velocity.

AOUPs

The tilted generator for the entropy production of an isolated AOUP is

$$L_\lambda = v\,\boldsymbol{b}\cdot\left[\nabla_{\boldsymbol{r}} + \lambda\frac{v\,\boldsymbol{b}}{D_\mathrm{t}}\right] + D_\mathrm{t}\left[\nabla_{\boldsymbol{r}} + \lambda\frac{v\,\boldsymbol{b}}{D_\mathrm{t}}\right]\cdot\left[\nabla_{\boldsymbol{r}} + \lambda\frac{v\,\boldsymbol{b}}{D_\mathrm{t}}\right] + \frac{D_\mathrm{a}D_\mathrm{r}^2}{v^2}\nabla_{\boldsymbol{b}}^2 - D_\mathrm{r}\boldsymbol{b}\cdot\nabla_{\boldsymbol{b}}\ , \tag{4.24}$$

which contains an additional convective term in $\boldsymbol{b}$ due to the constant restoring force. Assuming the system maintains a uniform and isotropic state at all λ, such that the eigenvector does not depend on $\boldsymbol{r}$, we can simplify the tilted operator,

$$L_\lambda = \lambda\frac{v^2|\boldsymbol{b}|^2}{D_\mathrm{t}} + \lambda^2\frac{v^2|\boldsymbol{b}|^2}{D_\mathrm{t}} + \frac{D_\mathrm{a}D_\mathrm{r}^2}{v^2}\nabla_{\boldsymbol{b}}^2 - D_\mathrm{r}\boldsymbol{b}\cdot\nabla_{\boldsymbol{b}}\ , \tag{4.25}$$

where b is the magnitude of the vector $\boldsymbol{b}$. The domain of b is from 0 to ∞, the eigenvector from equation (4.17) is

$$\nu_\lambda(\boldsymbol{b}) = \exp\left(\frac{v^2|\boldsymbol{b}|^2\psi_f(\lambda)}{4D_\mathrm{a}D_\mathrm{r}^2}\right) , \tag{4.26}$$

and its corresponding eigenvalue is

$$\psi_f(\lambda) = D_\mathrm{r}\left(1 - \sqrt{1 - \frac{4D_\mathrm{a}}{D_\mathrm{t}}\lambda(1+\lambda)}\right) , \tag{4.27}$$

which can be verified by inserting $\nu(\boldsymbol{b})$ back into Eq. 4.25 and noting that since it's in two dimensions it is split up into the x and y dimensions with $|\boldsymbol{b}|^2 = \boldsymbol{b}\cdot\boldsymbol{b} = b_x^2 + b_y^2$ and $\nabla_{\boldsymbol{b}}^2 = \nabla_{b_x}^2 + \nabla_{b_y}^2$. The left eigenvector can also be solved to obtain the normalization constant but it is not needed for the control force calculations.

The optimal control force in the $\boldsymbol{r}$ and $\boldsymbol{b}$ directions, $\boldsymbol{u}_\lambda = \{\boldsymbol{u}_\lambda^{\boldsymbol{r}}, \boldsymbol{u}_\lambda^{\boldsymbol{b}}\}$ are

$$\boldsymbol{u}_\lambda = \{2\lambda v\,\boldsymbol{b}, \boldsymbol{b}\psi_f(\lambda)\} , \tag{4.28}$$

which is the result in the main text for the control force for non-interacting AOUPs. The biased equations of motion become

$$\dot{\boldsymbol{r}}_i = v\,(1+2\lambda)\;\boldsymbol{b}_i + \sqrt{2D_\mathrm{t}}\boldsymbol{\eta}_i , \tag{4.29}$$

and

$$\dot{\boldsymbol{b}}_i = -D_\mathrm{r}\boldsymbol{b}_i\,(1 - \psi_f(\lambda)/D_\mathrm{r}) + \sqrt{2D_\mathrm{a}D_\mathrm{r}^2/v^2}\boldsymbol{\xi}_i , \tag{4.30}$$

where the former is identical for ABPs and the latter is specific to AOUPs.

In simulations, we relate AOUPs to ABPs by setting $v = \sqrt{2D_\mathrm{a}D_\mathrm{r}}$ as shown in section 4.3.

Entropy bounds from Girsonov transformation

One of the main results being the bound in Eq. 4.15 is obtained by manipulating the path action so the derivation is detailed in this section. The CGF for the entropy production can be rewritten as an average over the biased ensemble by performing a change of measure, or Girsonov transformation, from the original path ensemble with probability $P[\Gamma]$,

$$\begin{aligned}
\psi(\lambda) &= \frac{1}{tN}\ln\int \mathcal{D}[\Gamma]P[\Gamma]e^{\lambda\Delta S} \\
&= \frac{1}{tN}\ln\int \mathcal{D}[\Gamma]\frac{P[\Gamma]}{P_{\boldsymbol{u}_\lambda}[\Gamma]}P_{\boldsymbol{u}_\lambda}[\Gamma]e^{\lambda\Delta S} \\
&= \frac{1}{tN}\ln\left\langle\frac{P[\Gamma]}{P_{\boldsymbol{u}_\lambda}[\Gamma]}e^{\lambda\Delta S}\right\rangle_{\boldsymbol{u}_\lambda} ,
\end{aligned} \tag{4.31}$$

where $P_{\boldsymbol{u}_\lambda}[\Gamma]$ denotes a path ensemble with an additional force $\boldsymbol{u}_\lambda$ added to the original equations of motion, and $\langle \dots \rangle_{\boldsymbol{u}_\lambda}$ denotes an ensemble average with respect to that measure. Using Jensen's inequality, we find a general bound within an arbitrary control ensemble [171],

$$\psi(\lambda) \geq \frac{1}{tN} \left(\lambda \langle \Delta S \rangle_{\boldsymbol{u}_\lambda} + \left\langle \ln \frac{P[\Gamma]}{P_{\boldsymbol{u}_\lambda}[\Gamma]} \right\rangle_{\boldsymbol{u}_\lambda} \right) , \tag{4.32}$$

which need not be tight. However, below we show how in the systems studied by choosing $\boldsymbol{u}_\lambda$ to be the optimal control force for the free particle, we can arrive at the tight bound on the entropy production introduced in section 4.3.

ABPs

The relative actions with and without the single particle control force for a system of interacting ABPs is

$$\ln \frac{P[\Gamma]}{P_{\boldsymbol{u}_\lambda}[\Gamma]} = \sum_{i=1}^{N} \int_0^t dt' \, \frac{v^2 \lambda(1+\lambda)}{D_\mathrm{t}} - \frac{v}{D_\mathrm{t}} \lambda \boldsymbol{b}_i \circ \dot{\boldsymbol{r}}_i + \beta v \lambda \boldsymbol{b}_i \cdot \boldsymbol{F}_i \left(\boldsymbol{r}^N \right) , \tag{4.33}$$

which employs the identity $\boldsymbol{b} \cdot \boldsymbol{b} = 1$. We recognize the first term on the right hand side as $\psi_f(\lambda)$, the second term as the negative of the entropy production, and the final term as ΔW. Inserting this relative action into Eq. 4.31, we note that the entropy production terms cancel, and we can pull the constants out of the average. The bound can be shown to work analogously for the ADP and RTP models since the added control force does not change the statistics of the orientation, $\boldsymbol{b}$, and only changes the positional degrees of freedom.

AOUPs

The relative actions with and without the single particle control force for a system of interacting AOUPs is

$$\begin{aligned} \ln \frac{P[\Gamma]}{P_{\boldsymbol{u}_\lambda}[\Gamma]} = \int_0^t dt' \left(\frac{\lambda(1+\lambda)}{D_\mathrm{t}} - \frac{\psi_f(1 - \psi_f / 2D_\mathrm{r})}{2 D_\mathrm{a} D_\mathrm{r}} \right) v^2 b^2 \\ + \psi_f(\lambda) - \frac{v}{D_\mathrm{t}} \lambda \boldsymbol{b}_i \circ \dot{\boldsymbol{r}}_i + v \beta \lambda \boldsymbol{b_i} \cdot \boldsymbol{F}_i \left(\boldsymbol{r}^N \right) , \end{aligned} \tag{4.34}$$

which is more complicated than for the ABPs due to the fluctuating magnitude of the self-propulsion vector. We still can identify the same structure as before, with the free particle CGF, negative of the entropy production, and ΔW, however there is an additional first term in the parenthesis. Inserting the definition of ψ_f from Eq. 4.27 we find that the term proportional to $v^2 b^2$ is identically 0. This leaves us with the result for the bound in the main text.

4.5 Maximizing dissipation and collectively moving phase

In order to understand the origins of the deviations from the bound and the connections to collective behavior in active matter, we consider in detail a system of ABPs at conditions near and far from its motility induced phase separation (MIPS) transition. Additionally, the asymmetry of entropy production fluctuations about its average, motivates us to consider separately fluctuations of $s > \langle s \rangle_0$ and $s < \langle s \rangle_0$. In Fig. 4.2, the distributions for $s > \langle s \rangle_0$ are shown for $v = 10$ and $v = 120$, for a variety of system sizes at fixed density, $\rho = 0.1$. While the probability is larger than predicted by the bound, it can be perturbatively corrected. Specifically, we can expand Eq. 4.13 up to the second cumulant, $\psi(\lambda) \approx \psi_f(\lambda) + (\lambda \langle \Delta W \rangle_0 + \lambda^2 \langle \delta \Delta W^2 \rangle_0 / 2) / Nt$. The result of this approximation to the rate function is shown in Figs. 4.2 a) and b). For $v = 10$ the fluctuations are well described by the cumulant approximation, while for $v = 120$ asymptotic entropy production fluctuations are narrower than predicted. The Gaussian fits for small fluctuations for $v = 10$ and $v = 120$ is $\langle s \rangle_0 = v^2(1 - 0.84\rho)$, $\langle (\delta s)^2 \rangle = 3v^2$, and $\langle s \rangle_0 = v^2(1 - 0.63\rho)$, and $\langle (\delta s)^2 \rangle = 12v^2$ with $\rho = 0.1$ which are represented by black dotted lines. There is not a clear size dependence for the system sizes studied here and we have found that all three system sizes considered have the same best fit.

The asymptotic behavior for $s \gg \langle s \rangle_0$ is well described by free particle motion for all v's. This can be seen by considering $d\psi/d\lambda = \langle s \rangle_\lambda$ from $\langle s \rangle_\lambda = \int ds\, s \exp\{Nt[-I(s) + \lambda s - \psi(\lambda)]\}$, which is a direct probe of the tails of $I(s)$. As shown in Figs. 4.2 c) and d), for both large and small v, $\langle s \rangle_\lambda$ exhibits a crossover from Gaussian statistics. Near $\lambda = 0$, $\langle s \rangle_\lambda$ varies linearly with λ with a slope given by the variance $\langle \delta s^2 \rangle_0$. For $\lambda \gg 0$, $\langle s \rangle_\lambda$ varies linearly with λ with a slope given by the free particle variance. An analogous crossover has been noted in the current statistics of an interacting tagged ABP described in chapter 2 [25]. The asymptotic free behavior implies that the most likely way for the system to produce large amounts of entropy is to suppress density correlations and decrease ΔW. This behavior results from the system adopting a net orientation for the particles' self-propulsion vector [163, 172]. If the net orientation persists in the thermodynamic limit, it would represent a spontaneous symmetry breaking [173].

4.6 Minimizing dissipation and phase separation

Fluctuations for $s < \langle s \rangle_0$ are much larger than predicted by the bound and are collective in origin. Fig. 4.3 shows the distributions of entropy production and $\langle s \rangle_\lambda$ for $v = 10$ and $v = 120$ at $\rho = 0.1$ for 3 system sizes. The distributions in Figs. 4.3 a) and b) show significant finite size effects for $s < \langle s \rangle_0$. In Figs. 4.3 c), and d), this is evident by a transition between two types of behavior that sharpens with increasing N and occurs at larger λ with increasing v over the limited range of system sizes we can study numerically. These features are a hallmark of a dynamical phase transition, in this case between a dilute

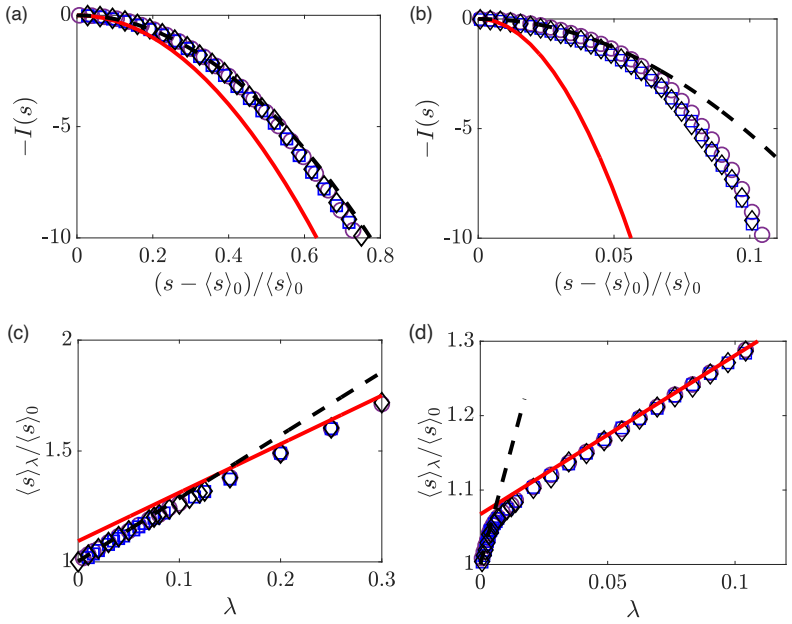

Figure 4.2: Larger than average entropy production fluctuations for ABPs with $N = 10$ (purple circles), 20 (blue squares), and 40 (black diamonds). Distribution of entropy production for a) $v = 10$ and b) $v = 120$ with $\rho = 0.1$. In a) and b), the red lines are $I_b(s)$ and the dashed black lines are fits at $\lambda = 0$ to extract the second cumulant. The average entropy production at finite λ for c) $v = 10$ and d) $v = 120$ with $\rho = 0.1$. The dashed lines are from the cumulant fits in a) and b), and the red line is the non-interacting rate function.

phase and a phase separated state reminiscent of MIPS [114, 48, 174]. As has been found previously [163], this shows that the most likely way for the system to produce little entropy is to condense, decreasing the particles' displacement by increasing the effective drag. We find we can describe $I(s)$ by explicitly assuming that each dynamical phase is well approximated by a Gaussian distribution. Specifically, assuming $\psi_i(\lambda)Nt = \lambda\langle\Delta S\rangle_i + \lambda^2\langle\delta\Delta S^2\rangle_i/2$ for $i = d, c$ being the dilute and condensed phases, the rate function can be computed from a contraction principle [43] for the CGF, $\psi(\lambda) = \max_\lambda[\psi_c(\lambda), \psi_d(\lambda)]$. The result is a Maxwell construction and is shown in Fig. 4.3 to be a good approximation in the infinite system size limit.

The Gaussian fit for the phase separated peak in Fig. 4.3 is given by $\langle s\rangle_0 = v^2(1-0.84\rho)$, $\langle(\delta s)^2\rangle = 2v^2$ for v=10 with $\rho = 0.58$, and $\langle s\rangle_0 = v^2(1-0.84\rho)$, $\langle(\delta s)^2\rangle = 2v^2$ for v=120 with $\rho = 1.12$. Note that the variance for both v's considered for the phase separated system is given by the non-interacting CGF. The averages used in the Maxwell construction and those in Fig. 4.3 c, and d of the main text are slightly different due to the shift in the mean in the thermodynamic limit given by $\langle s\rangle_{\lambda_c} = \langle s\rangle_0 + \lambda_c\langle(\delta s)^2\rangle_0$ but the slopes are identical.

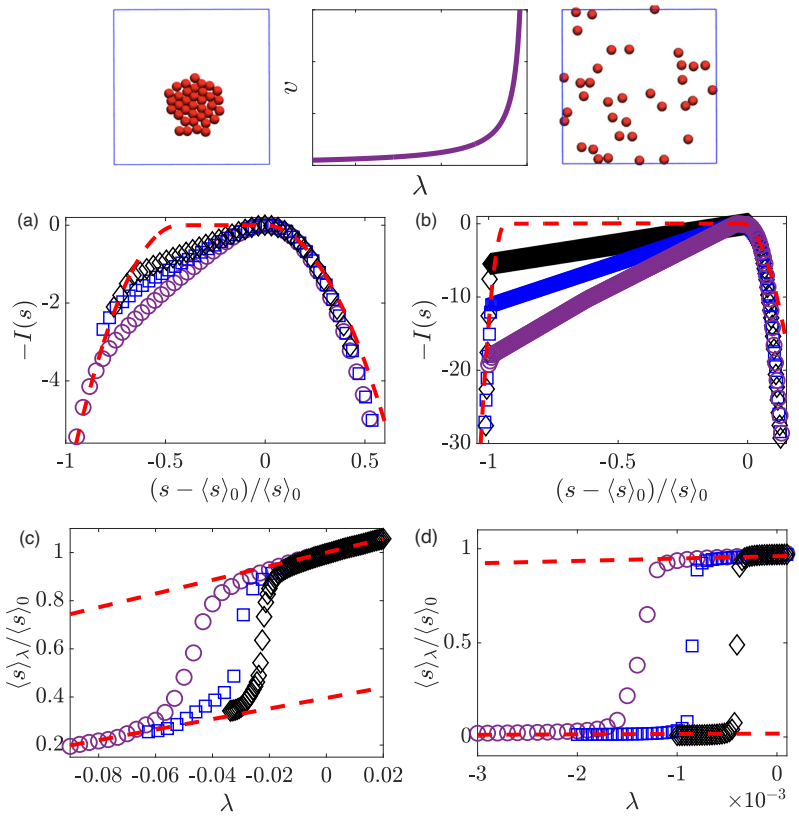

Figure 4.3: Smaller than average entropy production fluctuations and dynamical phase transition for ABPs for different system sizes $N = 10$ (purple circles), 20 (blue squares), and 40 (black diamonds). The phase diagram and example structures are illustrated at the top with phase separation on the left of the phase diagram and a homogeneous state on the right. Distribution of entropy production for a) $v = 10$ and b) $v = 120$ with $\rho = 0.1$. In a) and b), the dashed red lines are a Maxwell construction for the dynamical phases. The average entropy production at finite λ for c) $v = 10$ and d) $v = 120$ with $\rho = 0.1$. The dashed red lines are from the Gaussian fits in a) and b) used in the Maxwell construction.

4.7 Controlling phase separation

Entropy production from coarse-grained density field

For $s < \langle s \rangle_0$, it is not sufficient to perturbatively correct the bound even for $v = 10$, which is far from the MIPS transition. To understand this behavior we have developed a coarse-grained theory. We define a fluctuating density field as $\rho(\boldsymbol{r}, t) = \sum_{i=1}^{N} \delta[\boldsymbol{r} - \boldsymbol{r}_i(t)]$.

Assuming that the important contributions to the inter-particle entropy production comes from forces that directly oppose self-propulsion, we approximate $\boldsymbol{b}_i \cdot \boldsymbol{F}(\boldsymbol{r}_{ij}) \approx -F(r_{ij})$ where $\boldsymbol{F}(\boldsymbol{r}_{ij})$ is the contribution of the ith particle's force due to particle j and $\boldsymbol{r}_{ij}$ is the dis-

placement vector between particles i and j with magnitude r_{ij}. Under this approximation the fluctuations of ΔW depend only on the time evolution of the density field and can be written in terms of $\rho(\boldsymbol{r},t)$, $\Delta W \approx -\beta v \int dt \int d\boldsymbol{r} d\boldsymbol{r}' \rho(\boldsymbol{r},t) F(|\boldsymbol{r}-\boldsymbol{r}'|)\rho(\boldsymbol{r}',t)/2$, which is a convolution of two points of the density field with the interparticle force. For simplicity we have assumed that $F(0)=0$. Further assuming that the force can be Fourier transformed, we find

$$\Delta W = -\frac{\beta v}{2}\int dt \int dk\, |\hat{\rho}(k,t)|^2 \hat{F}(k)\,, \tag{4.35}$$

where $\hat{\rho}(k,t)$ is the Fourier transformed isotropic density field and $\hat{F}(k)$ the Fourier transformed force.

Below we first derive an approximate equation of motion for the density, in the limit of small k and small fluctuations from its mean. Then we describe the approximate calculation of the cumulant generating function and control force.

Equation of motion for the density

We are interested in the density fluctuations with the added control force which changes the self propulsion speed proportional to lambda as $v_\lambda = v(1+2\lambda)$. To arrive at an effective equation of motion for the density we first define the instantaneous density field as,

$$\rho(\boldsymbol{r},t) = \sum_{i=1}^{N} \delta[\boldsymbol{r}-\boldsymbol{r}_i(t)]\ , \tag{4.36}$$

and corresponding polarization field as

$$\boldsymbol{P}(\boldsymbol{r},t) = \sum_{i=1}^{N} \delta[\boldsymbol{r}-\boldsymbol{r}_i(t)]\boldsymbol{b_i}(t)\ , \tag{4.37}$$

where δ are Dirac's delta function. In principle, higher order multipoles in the orientation field are needed to completely describe the dynamics, however we neglect quadrupole and higher fields. For the homogeneous states considered, this has been shown to be a good approximation [77, 70]. Following the standard procedures [175, 82] a set of coupled stochastic equation of motion for both fields. For the density field,

$$\frac{\partial \rho(\boldsymbol{r},t)}{\partial t} = -\nabla_{\boldsymbol{r}}\left[\mu\rho(\boldsymbol{r},t)\int d\boldsymbol{r}'\boldsymbol{F}(\boldsymbol{r}-\boldsymbol{r}')\rho(\boldsymbol{r}',t) + v_\lambda \boldsymbol{P}(\boldsymbol{r},t)\right] + D_t\nabla^2_{\boldsymbol{r}}\rho(\boldsymbol{r},t) + \nabla_r\sqrt{2\Delta_\lambda}\boldsymbol{\eta_\rho}(\boldsymbol{r},t) \tag{4.38}$$

where $\Delta_\lambda = D_{\mathrm{t}}\rho(\boldsymbol{r},t)$ is the mobility and the noise obeys the statistics $\langle \boldsymbol{\eta_\rho}(\boldsymbol{r},t)\rangle = 0$ and $\langle \eta^\alpha_\rho(\boldsymbol{r},t)\eta^\beta_\rho(\boldsymbol{r}',t')\rangle = \delta_{\alpha,\beta}\delta(t-t')\delta(\boldsymbol{r}-\boldsymbol{r}')$. For the polarization field,

$$\frac{\partial \boldsymbol{P}(\boldsymbol{r},t)}{\partial t} = -\nabla_{\boldsymbol{r}}\left[\mu\boldsymbol{P}(\boldsymbol{r},t)\int d\boldsymbol{r}' F(\boldsymbol{r}-\boldsymbol{r}')\rho(\boldsymbol{r}',t)\right] - \nabla_{\boldsymbol{r}}\frac{v_\lambda\rho(\boldsymbol{r},t)}{2} + D_t\nabla^2_{\boldsymbol{r}}\boldsymbol{P}(\boldsymbol{r},t) - D_{\mathrm{r}}\boldsymbol{P}(\boldsymbol{r},t) + \nabla_{\boldsymbol{r}}\sqrt{2\Lambda_P}\boldsymbol{\eta_P}(\boldsymbol{r},t) \tag{4.39}$$

where $\boldsymbol{\eta_P}(\boldsymbol{r},t)$ has the same noise statistics as $\boldsymbol{\eta}_\rho$ and $\Lambda_P = D_t\boldsymbol{P}(\boldsymbol{r},t)$.

We assume there is a separation of time scales between the density field, which we assume to be slow, and the polarization field, which we assume to relax quickly. Further we assume that on the scale of density fluctuations, the polarization is constant and homogeneous [6]. These so-called adiabatic assumptions are standard in the treatment of instabilities in the ABP system. Under these assumptions, the polarization is stationary and can be averaged separately from the density and we can neglect its gradient terms. Rearranging the remaining terms, we have an explicit relation between the polarization and density fields,

$$P(\boldsymbol{r},t) = -\frac{v_\lambda}{2D_\mathrm{r}}\nabla_{\boldsymbol{r}}\rho(\boldsymbol{r},t)\ , \tag{4.40}$$

which effectively separates the evolution of the two fields. Inserting this into Eq. (4.38) we arrive at a closed equation of motion for the density,

$$\frac{\partial\rho(\boldsymbol{r},t)}{\partial t} = -\nabla_{\boldsymbol{r}}\left[\mu\rho(\boldsymbol{r},t)\int d\boldsymbol{r'}\boldsymbol{F}(\boldsymbol{r}-\boldsymbol{r'})\rho(\boldsymbol{r'},t)\right] + \mathcal{D}_\lambda\nabla^2_{\boldsymbol{r}}\rho(\boldsymbol{r},t) + \nabla_{\boldsymbol{r}}\sqrt{2\Delta_\lambda}\boldsymbol{\eta}_\rho(\boldsymbol{r},t) \tag{4.41}$$

with $\mathcal{D}_\lambda = D_\mathrm{t} + v_\lambda^2/2D_\mathrm{r}$ as the effective diffusion constant.

While the equation is closed, it is still nonlinear due to the fluctuating convective term from the interparticle interactions. While more sophisticated expansions exist, for low densities, we can linearize the evolution equation by simply dropping the second order term in the density,

$$\frac{\partial\rho(\boldsymbol{r},t)}{\partial t} = \mathcal{D}_\lambda\nabla^2_{\boldsymbol{r}}\rho(\boldsymbol{r},t) + \nabla_{\boldsymbol{r}}\sqrt{2\Delta_\lambda}\eta_\rho(\boldsymbol{r},t)\ , \tag{4.42}$$

which results in a standard fluctuating diffusion equation. Corrections due to interactions can be included phenomenologically by making $\mathcal{D}_\lambda$ and Δ_λ depend on the mean density. Introducing the Fourier transforms, for the density

$$\hat{\rho}(\boldsymbol{k},t) = \int d\boldsymbol{r}e^{-i\boldsymbol{k}\cdot\boldsymbol{r}}\rho(\boldsymbol{r},t)\ , \tag{4.43}$$

and the noise,

$$\hat{\boldsymbol{\eta}}(\boldsymbol{k},t) = \int d\boldsymbol{r}e^{-i\boldsymbol{k}\cdot\boldsymbol{r}}\boldsymbol{\eta}(\boldsymbol{r},t)\ , \tag{4.44}$$

we can arrive at the equation of motion in Fourier space to be

$$\partial_t\hat{\rho}(k,t) = -k^2\mathcal{D}_\lambda\hat{\rho}(k,t) + \sqrt{2\Delta_\lambda k^2}\hat{\eta}(k,t)\ , \tag{4.45}$$

where, since the system is isotropic, the Fourier transform of the density and noise can be represented as scalar functions. The $\mathcal{D}_\lambda$, is the effective diffusion constant, Δ_λ is the effective mobility, and $\hat{\eta}_\rho$ is a complex noise [6, 2, 85, 48, 176]. We have also redefined $\hat{\eta}(k,t) \to i\hat{\eta}(k,t)$ as an imaginary noise to get our final form, where

$$\langle\eta(k,t)\eta^*(k,t')\rangle = \delta(t-t')\ , \tag{4.46}$$

are its statistics that are local in k-space and $*$ denoted complex conjugate.

The equation of motion for the Fourier transformed density in Eq. 4.45 takes the form of a set of uncoupled, complex Ornstein-Uhlenbeck processes for each wavevector. The large deviations of such a system for observables similar to ΔW have been considered in detail previously [176]. The method to quantify the fluctuations of ΔW involves solving the eigenspectrum of the tilted operator defined as

$$\mathcal{L}_\lambda = \sum_{k>0} -k^2\mathcal{D}_\lambda\hat{\rho}_k\nabla_{\hat{\rho}_k} + k^2\Delta_\lambda\nabla^2_{\hat{\rho}_k} - \lambda\frac{\beta v_\lambda}{2}\hat{F}(k)\left|\hat{\rho}_k\right|^2 \ , \tag{4.47}$$

which has to be solved for both the real and imaginary parts of $\hat{\rho}_k$. The CGF for ΔW can be solved exactly within this approximate linearized dynamics. Defining $\Delta\psi = \psi - \psi_f$,

$$\Delta\psi(\lambda) = \frac{1}{N}\sum_{k>0}\Delta\psi_k(\lambda) \ , \tag{4.48}$$

where for each k,

$$\Delta\psi_k(\lambda) = k^2\mathcal{D}_\lambda\left[1 - \sqrt{1 + \frac{\beta\lambda v_\lambda\hat{F}(k)\Delta_\lambda}{\mathcal{D}_\lambda^2 k^2}}\right] \ , \tag{4.49}$$

and the corresponding eigenvector

$$\nu_\lambda = \prod_{k>0}\exp\left[\frac{\left|\rho(k,t)\right|^2}{2\Delta_\lambda k^2}\Delta\psi_k(\lambda)\right] \ , \tag{4.50}$$

factorizes into a product of independent modes, each quadratic in the density. For a density type variable, the optimal control force is a gradient force, and so can be written as a potential.

From this result we can obtain a more accurate bound than Eq. (4.15) by including the contribution from interparticle correlations. This correction is valid for all positive λ, but becomes unstable at a critical value $\lambda_c \leq 0$ reflecting the breakdown in the linearized evolution equation for $\hat{\rho}(k,t)$. For a finite system with largest wavevector $k = 2\pi\sqrt{\rho/N}$, the location of the instability is found by setting the discriminant to zero, $\lambda_c \approx -4\pi^2\mathcal{D}_0^2\rho/\beta v\hat{F}(0)\Delta_0 N$ where for the short ranged forces considered, we can approximate the force as $\hat{F}(0)$ and we can neglect the λ dependence in $v_\lambda, \mathcal{D}_\lambda$, and Δ_λ. This instability signals the dynamical phase transition that occurs at $\lambda_c = 0^-$ in the thermodynamic limit and whose influence on the dynamics of active matter increases with v, and with increasing proximity to MIPS, consistent with the results in Fig. 4.3. In a phase separated state, ΔW is a large negative number which counteracts the free particle contribution and reduces the entropy production.

The origin of phase separation can be understood by noting that the optimal control potential which gives rise to rare entropy fluctuations is, for large interparticle separations $r/\sigma \gg 0$ and in the limit λ approaches zero,

$$\hat{V}_\lambda \approx -\frac{\beta v\lambda}{N\mathcal{D}_0}\sum_{k>0}\frac{\left|\hat{\rho}(k,t)\right|^2}{2k^2}\hat{F}(k) \ . \tag{4.51}$$

The inverse Fourier transform will involve a convolution between the WCA force and $1/k^2$ which gives rise to a Bessel Function. Since the WCA potential quickly decays, the long range contribution in real space is a logrithmic potential,

$$V_\lambda(r) \approx -\frac{\beta\lambda v}{\mathcal{D}_0} \ln r/2 \ , \tag{4.52}$$

which is attractive for $\lambda < 0$ with a magnitude that depends on v and the control force is $\boldsymbol{u}_\lambda \approx (\beta\lambda v/\mathcal{D}_0)\nabla \ln r/2$. For negative enough λ or large enough v, this force will give rise to phase separation. This optimal control force is similar to other passive models near diffusive instabilities [177, 178, 176].

The long-ranged effective force demonstrates how effective attractions are introduced by self-propulsion in order to minimize the entropy production. This force is unique and encodes the way in which self-propelled particles interact provided the condition of obtaining a lower than average value of the entropy production. As such, it provides a sharp relationship between entropy production and emergent collective behavior in active matter. Correlations between entropy production and motility induced phase separation have been observed previously at the level of the mean behavior [179, 121, 180], however this work codifies that relationship on the level of fluctuations.

For both MIPS and the dynamical transition we discuss, phase separation is the result of a diffusive instability where density accumulates due to unbalanced fluxes made possible by the system being kept from thermal equilibrium. We have shown such collective behavior results from the reduction of entropy production and enhancement of density correlations. Large entropy production by contrast, arises through the suppression of density correlations. Thus, our results show how the structure of entropy production fluctuations are intimately connected to long-ranged correlations in active matter. We expect that deviations from the bound derived here can serve as a guide to identify criticality and novel phases of active matter generally.

Chapter 5

Phase separation in the cell

Introduction

In an equilibrium system, the steady state structures are usually those that minimize the surface area. This is why, for instance, that during liquid-vapor phase separation the equilibrium liquid phase usually forms a large macroscopic circular droplet. However, multiple 3 dimensional membraneless organelles defy this logic and can coexist in the cell by a theorized phenomenon called liquid-liquid phase separation (LLPS) [181, 182]. Within this framework multiple liquid-like droplets are considered to be in equilibrium and can coexist because of supersaturation [183, 184]. Recently, it has been a question whether LLPS will be a unifying theory to connect 2 dimensional and 3 dimensional condensates [185]. However, there has been a dearth of detailed characterization of 2 dimensional protein phase transitions from either the kinetic or thermodynamic aspects. Interestingly, a recent study recognized that attaching proteins to the membrane, by posing diffusive limitations and stabilizing the condensates, drastically altered the phase transition outcome of a protein/mRNA system from its 3D LLPS results [186]. With these observations, one may question whether LLPS is the only method in which phase separation in the cell occurs. In this section I will introduce a minimal model that has all the necessary biological details based on an experimental study of 2 dimensional condensates from our collaborators. This will then allow the construction of a minimal model to understand the mechanism of aggregation in 2 dimensions.

5.1 LAT assembly: experimental motivations

LAT is an intrinsically disordered protein that contains many modifiable sites that become active by phosphorylation. When Growth Factor Receptor-Bound Protein 2 (Grb2), and Son of Sevenless (SOS) are added to LAT, the system undergoes a phase transition which is associated with amplification of T cell signal transduction [5, 4]. Specifically, Fig. 5.1a shows the engagement of TCR with pMHC results in phosphorylation of LAT, which triggers assembly reactions on the cytoplasmic side of the plasma membrane by recruiting Grb2 and

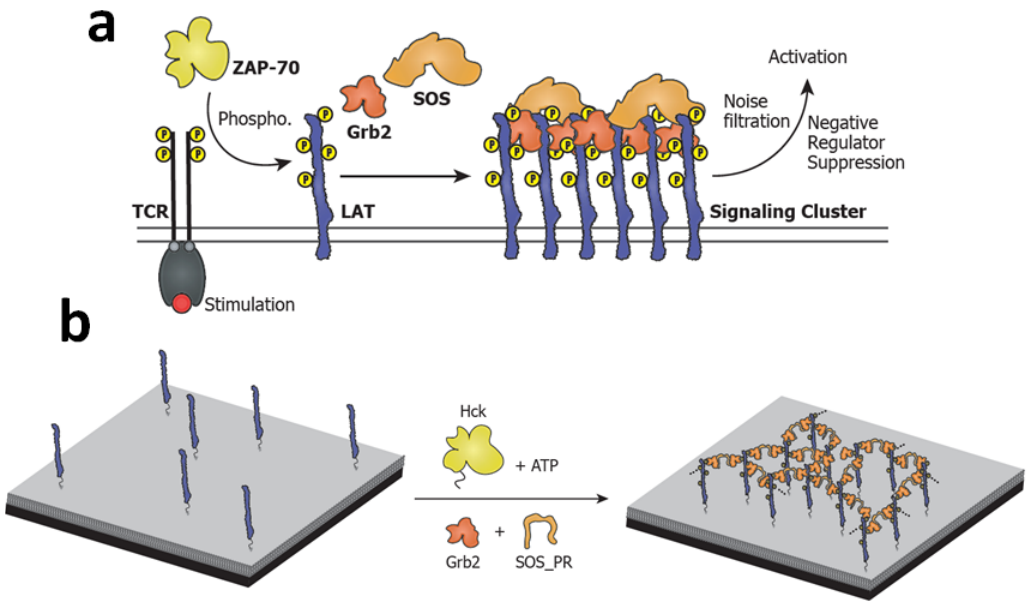

Figure 5.1: Schematic illustration of the LAT-Grb2-SOS condensation phase transition system: a) The TCR signaling pathway which involves assembly formation with LAT-Grb2-SOS. b) In vitro reconstitution of the LAT-Grb2-SOS condensation phase transition on a supported lipid bilayer, where the assembly eventually condenses to a disordered state.

SOS. The recruited and activated SOS leads to further propagation of downstream signals. This assembly is formed through a number of multivalent interactions across the protein components, specifically, the binding of the SH2 domain of Grb2 with three phosphorylated tyrosine residues on LAT and the interactions between the SH3 domains of Grb2 and potentially five proline-rich domains of SOS [187, 188, 189]. Moreover, both LAT-Grb2 and Grb2-SOS interactions exhibit relatively fast binding kinetics [3]. By applying the reductionist approach of *in vitro* reconstitution and attaching LAT molecules to a model lipid membrane (Fig. 5.1b), the progress of the condensation can be tracked over time by total internal reflection fluorescence microscopy (TIRFM). In Fig. 5.2a), the fluorescence images of LAT-555 before and after the phase transition is shown. In the time course of 70 minutes, the LAT-Grb2-SOS network went through a macroscopic phase transition and reached the final state with two types of domains displaying distinctly different fluorescence intensities: the heterogeneously shaped bright regions with high LAT concentration (defined as the "condensed" domains) and the dark regions with low LAT concentration (defined as "dispersed" domains). Before introducing SOS, the fluorescence intensity distribution of the homogeneous LAT layer showed a histogram profile well fitted to a single Gaussian peak. During the course of the phase transition, there was a time-dependent broadening of the histogram profile. After the two domains reached the steady state, the fluorescence intensity distri-

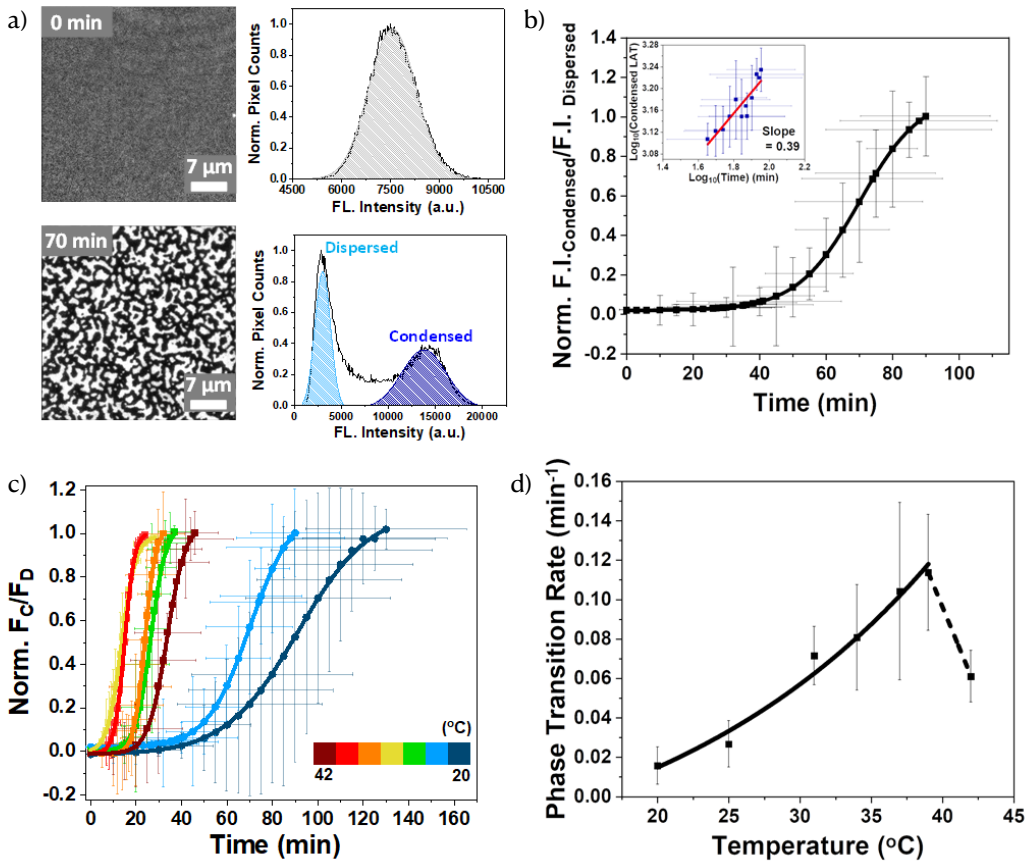

Figure 5.2: Kinetic characterization of the LAT-Grb2-SOS phase transition. a) On the left are TIRF images of the LAT-555 layer before and after phase transition with 5.8 µM Grb2 + 1.45 µM SOS. On the right are corresponding fluorescence intensity histograms with the 0 min profile fitted to a single Gaussian peak (grey shades) and the 70 min profile showing two well separated Gaussian peaks (light blue and royal blue shades). b) Kinetic profile of the phase transition at 25 °C. The inset shows the LAT density in the condensed domains during the phase transition as a function of time plotted in the log-log scale. The fitted slope of the linear trendline is 0.39. Error bars represent the standard deviation from eight individual experiments. c) LAT-Grb2-SOS phase transition kinetic profiles in a temperature range from 20 °C to 42 °C, and the curves are color-coded according to the temperatures. Error bars represent the standard deviation from at least three repeats of experiments. d) Extracted phase transition rate as a function of temperature.

bution showed two prominent and well separated peaks, the positions of which correspond to the average fluorescence intensity in the condensed domains and the dispersed domains. The positions of these two peaks were monitored as the phase transition progressed and quantitatively analyzed in Fig. 5.2b). The kinetic profile of the phase transition fits well to a sigmoidal function, with a lag stage (40 min) and a transition stage. By simultaneously analyzing area fraction of the two domains during the phase transition, the LAT concentration in the condensed domains can be tracked over time (Fig. 5.2b), inset), which exhibited a power law increase with a time exponent of 0.39. It is worth noting that the phase transition can be completely and quickly ($<$ 2 min) reversed by adding a promiscuous phosphatase. In Fig. 5.2c), the kinetics of the phase transition as a function of temperature is analyzed for a range from 20 °C to 42 °C with LAT concentrations at 1200 ± 600 molecules/μm^2. It is clearly shown that increasing temperature drastically sped up the phase transition. The phase transition rate was quantified as the steepest slope on the sigmoidal curves. In Fig. 5.2d), the extracted phase transition rates were plotted against the temperature. From 20 °C to 39 °C, there was an exponential increase of k_{PT} by almost an order of magnitude. While above 39 °C, a sharp decrease of k_{PT} was observed.

5.2 Model

To single out the necessary physics and biology of this phase transition observed in experiments, a minimal microscopic model was developed for the equation of motion of LAT molecules and the bonding kinetics between LAT molecules. In the model, the equation of motion of the ith LAT molecule is given by

$$\dot{\boldsymbol{r}}_i = \mu \boldsymbol{F}_i \left(\boldsymbol{r}^N\right) + \sqrt{2k_B T \mu}\, \boldsymbol{\eta}_i \ , \tag{5.1}$$

where the mobility, μ, and Boltzmann's constant, k_B, are both set to unity. Additionally, each LAT molecule is assumed to be circular with a radius $\sigma = 10$ nm, which for comparison to experiments is the radius of gyration of LAT. The first term on the right of Eq. 5.1 is the intermolecular forces each LAT feel. Depending on whether they are bound or unbound they will have different forces. Unbound LAT have an excluded volume force between molecules given by a Weeks-Chandler-Anderson potential with a characteristic energy scale given by ϵ which is set to unity. Bound LAT have additionally an attractive harmonic force with a spring constant $k = 100\epsilon/\sigma^2$, and a rest bond length between pairs of LAT at 1.5σ. The forces in equation form are

$$U(r) = \begin{cases} U_{WCA}(r) & \text{unbound} \\ U_{WCA}(r) + U_H(r) & \text{bound} \end{cases} \ , \tag{5.2}$$

where

$$U_H(r) = \frac{1}{2} k \left(r - 1.5\sigma\right)^2 \ , \tag{5.3}$$

and

$$U_{WCA}(r) = \begin{cases} 4\epsilon \left[\left(\frac{\sigma}{r}\right)^{12} - \left(\frac{\sigma}{r}\right)^{6} \right] + \epsilon & r \leq 2^{1/6}\sigma \\ 0 & \text{otherwise} \end{cases} . \tag{5.4}$$

Also, the rates to make, k_{on}, and break bonds, k_{off}, are the product of a prefactor rate, k_{b}, which sets the time scale of bond formation, multiplied by the kinetic constraints which are that each LAT can form at most three bonds with other LAT molecules, and bonds are formed and broken within a reactive distance set to $R_{\text{react}} = 2\sigma$. The rates are related by a local detailed balance relation,

$$\frac{k_{\text{on}}}{k_{\text{off}}} = e^{-\beta E_B(r)} , \tag{5.5}$$

and the energy to make a bond is composed of a constant term plus the energy to make a harmonic bond written as

$$E_B(r) = -4 + U_H(r) . \tag{5.6}$$

We have now completely specified the model. In order to sample the dynamics in a consistent way, we must understand what local detailed balance means and an algorithm to implement it.

Local detailed balance

We would like to make and break bonds in a thermodynamically consistent way. This is ensured when the kinetics of this reaction follow detailed balance. Before I introduce how LAT make or break bonds in the model, I will explain the idea of local detailed balance and show the composition of the rates. Let's consider two generic states A and B. For instance, these two states could be the number of bonds of a LAT molecule. The transitions between states A and B obeys local detailed balance if [190]

$$P(A)k(A \to B) = P(B)k(B \to A) , \tag{5.7}$$

where $P(A)$ and $P(B)$ are the probabilities to be in state A and state B. Also, $k(A \to B)$ and $k(B \to A)$ are the rates to go from state A to state B and vice versa. Rearranging Eq. 5.7, we get

$$\frac{P(A)}{P(B)} = \frac{k(B \to A)}{k(A \to B)} . \tag{5.8}$$

For a system in equilibrium, the ratio of states is just a change in the Boltzmann weight shown as

$$\frac{P(A)}{P(B)} = e^{\beta[E(A)-E(B)]} . \tag{5.9}$$

The rate constants can be decomposed into a product of a proposal rates and acceptance probabilities:

$$k(A \to B) = \alpha(A \to B)P_{acc}(A \to B) \tag{5.10}$$

and

$$k(B \to A) = \alpha(B \to A) P_{acc}(B \to A). \tag{5.11}$$

The α in both reactions is the proposal rate or the prefactor rate represented as

$$\alpha = 1 - e^{-k_b \Delta t} \approx k_b \Delta t. \tag{5.12}$$

The P_{acc} is the acceptance probability of the proposed move and is represented in the Metropolis-Hastings algorithm [190] in both cases as

$$P_{acc} = \min\left[1, e^{\beta \Delta E}\right]. \tag{5.13}$$

Bonding

To incorporate the kinetic constraints of our LAT model in a realistic way, the detailed balance has to be slightly modified to account for bond making and breaking. Now the relation for detailed balance becomes [191, 192, 193, 191]

$$P(A) k(A \to B) h_{\text{reac}}(r) h_{\text{bond}}(A) = P(B) k(B \to A) h_{\text{reac}}(r) h_{\text{bond}}(B), \tag{5.14}$$

where

$$h_{\text{reac}}(r) = \begin{cases} 1 & \text{for } r \leq R_{\text{react}} \\ 0 & \text{otherwise .} \end{cases} \tag{5.15}$$

and

$$\{h_{\text{bond}}(A), h_{\text{bond}}(B)\} = \begin{cases} 1 & \text{for two or less bonds making another} \\ 0 & \text{three bonds making another} \\ 1 & \text{three or less bonds breaking a bond} \end{cases} \tag{5.16}$$

Hence, the rates are modified to account for the constraint that the bonds can only be made if two LAT molecules are within a reactive distance, R_{reac}, and they both have no more than two bonds each. Also, the contraint will be unity for any bonded LAT molecule proposing to break a bond. The rates to make or break bonds then become the following:

$$k(A \to B) = \alpha(A \to B) P_{\text{acc}}(A \to B) h_{\text{reac}}(r) h_{\text{bond}}(A) \tag{5.17}$$

and

$$k(B \to A) = \alpha(B \to A) P_{\text{acc}}(B \to A) h_{\text{reac}}(r) h_{\text{bond}}(B) \ . \tag{5.18}$$

This algorithm for bond making/breaking can be done by the Metropolis algorithm. At each step in the Monte Carlo algorithm, a pair of particles that are either bonded or capable of being bound are selected at random. If the randomly selected pair is bonded then there is a proposal of breaking a bond with $\alpha = 1 - \exp(-k_b \Delta t)$ and acceptance of breaking a bond with the Boltzmann weight with energy

$$E_B(r) = -4 + U_H(r) \ . \tag{5.19}$$

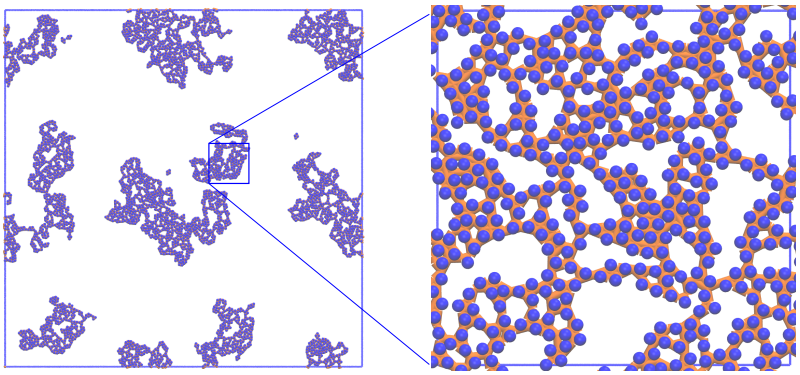

Figure 5.3: Snapshot of the LAT model system with LAT shown in blue and the orange are the bonds. On the left, is a system snapshot of 4000 particles at a density of $\rho\sigma^2 = 0.1$ and reduced temperature of $T/\bar{E}_B = 0.14$. On the right is a zoomed in snapshop of the dense phase.

5.3 Results

A snapshot of dynamics of the model are shown in Fig. 5.3. The system in Fig.5.3a) has 4000 particles and in Fig.5.3b) shows a zoomed in portion showing a single condensed phase region. We would like to study the dynamics and steady state properties of the dense phase.

Similarly to the the experiments, there are temperatures and densities where this system will phase separate and where the system is homogeneous. Before we go through a detailed study of the dynamics, we seek to understand the phase diagram and the steady state properties of the system. In Fig. 5.4a), the phase diagram is shown with the critical point represented as the red star at about $\rho\sigma^2 \approx 0.16$ and $T/\bar{E}_B \approx 0.19$. Above this critical temperature for all densities the system is observed to be in a homogeneous state. Below this critical temperature, phase separation is observed with the dilute phase represented by the light blue squares and the dense phase represented by the dark blue circles. The dense phase gets denser as the temperature decreases within the coexistance curve until about $T/\bar{E}_B \approx 0.1$ when the density plateaus at $\rho\sigma^2 = 0.38$. Surprisingly, there was no solid phase observed but instead even at temperatures very close to zero the system is observed to be dynamic with no long range order.

The coexistance curves were characterized by both setting up a slab with dimensions of $L_x = 6L_y$ and fitting the profile to a sigmoidal function and by a subsystem analysis as shown in Fig. 5.4b) and c) for $T/\bar{E}_B \approx 0.18$ and probe radii of d = 6σ, 8σ, 10σ, 12σ, and 14σ. Subsystem distributions of the total system were taken by moving a circular probe area, $a = \pi \mathrm{d}^2$, with radius d around the system and making a histogram of the local density, ρ_a. Systems with two coexisting phases will have a bimodal subsystem distribution with each peak representing the densities of the dense and dilute phases while the probe area is on the

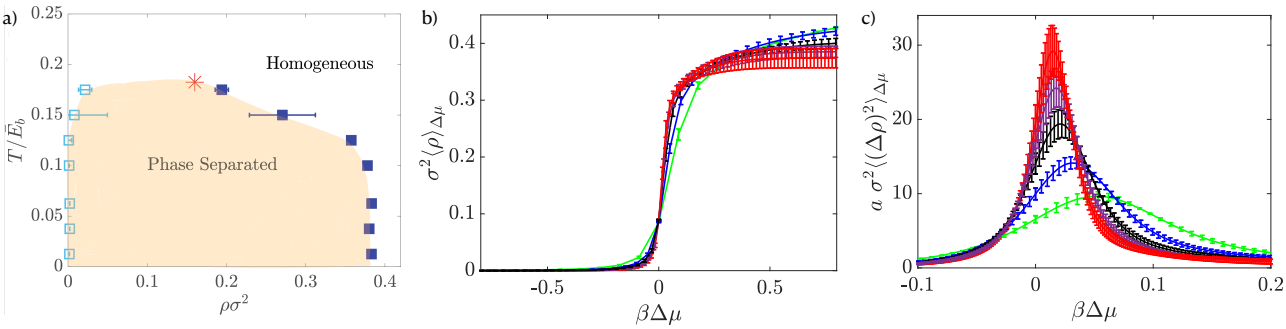

Figure 5.4: Phase diagram and coexisting phases. a) The phase diagram as a function of the reduced density and reduced temperature. The light blue squares are the dilute phase points and the solid blue squares are the dense phase points. The shaded region represents the phase points where there is phase separation. There is no dense phase observed. b) the average density from Eq. 5.20 as a function of the relative chemical potential, $\Delta\mu$, between the dense and dilute phase for circular probe areas of radii d = 6σ (cyan), 8σ (blue), 10σ (black), 12σ (purple), and 14σ (red). c) The average intensive variance, computed from Eq. 5.22, as a function of the relative chemical potential for the subsystem sizes as b).

length scale or smaller than the corresponding phases. In Fig. 5.4b), the average density, $\langle\rho_a\rangle_{\Delta\mu}$, for different subsystem sizes was calculated as a function of the relative chemical potential, $\Delta\mu$, between the dense and dilute phases by a weighted average similar to chapter 2,

$$\sigma^2\langle\rho_a\rangle_{\Delta\mu} = \sigma^2\left\langle\rho_a e^{a\Delta\mu\rho_a}\right\rangle_0 \ , \tag{5.20}$$

and

$$\langle\dots\rangle = \int d\rho_a \dots P(\rho_a), \tag{5.21}$$

where $P(\rho_a)$ is the probability distribution of observing a local density of area a which has a large deviation form. It can be seen that the average density of the system with a zero chemical potential is the same as the system density, $\langle\rho_a\rangle_0\sigma^2 = N\sigma^2/L^2 = 0.1$. For a positive chemical potential, the slope increases quickly to the dense phase at about $\rho\sigma^2 \approx 0.38$. The slope of the dense phase decreases as a function of increasing subsystem size which is expected since larger probe areas will have smaller fluctuations as the thermodynamic limit is approached. For negative chemical potential, the density quickly decreases to a density close to zero which represents the dilute phase density. By fitting these two slopes for the dense and the dilute phases the density of each phase can be inferred for each temperature with the results shown in Fig. 5.4a). In Fig. 5.4c), the intensive variance for each probe area is plotted as a function of the relative chemical potential which is written as

$$a\sigma^2\langle(\Delta\rho)^2\rangle_{\Delta\mu} = \sigma^2\frac{\langle\rho_a\rangle_{\Delta\mu}}{d\Delta\mu} \ . \tag{5.22}$$

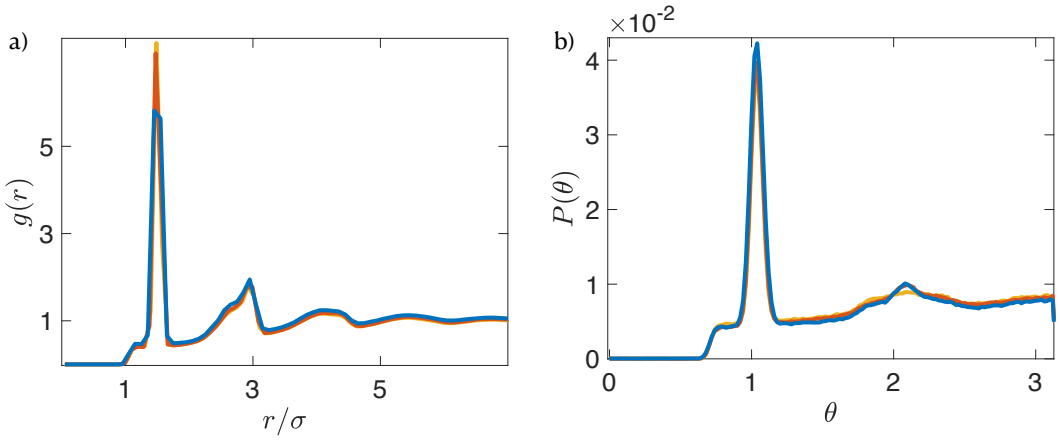

Figure 5.5: Steady state structure properties. a) The radial distribution function for temperatures of $T/\bar{E}_B = 0.18$(blue), 0.15(red), and 0.14(yellow) and their corresponding dense phase densities of $\rho\sigma^2 = 0.27$, 0.32, and 0.36. b) The distribution of relative angles between two bonds of a LAT molecule at the same phase points as b) with an average at 1.2 radians (68 degrees).

The intensive variance peak grows with system size with scaling falling in the category of first order phase transitions.

As mentioned previously, there was no dense phase found at low temperatures and in Fig. 5.3 the system snapshots show that there are many holes in the steady state dense phase. To characterize the structure of the dense phase, we have plotted the radial distribution function for dense phases for three phase points within the coexistance curve in Fig. 5.5a) and they look similar to a liquid with short range correlations but no long range order. Another question is if this is an ordered liquid with some local order or if the bonds are truly disordered. If this were a pure hexagonal crystal each LAT molecule would have a relative bond angle of 120 degrees. However, in Fig. Fig. 5.5b) the distribution of relative angles between two bonds of a LAT are plotted which shows that the average angle is about 70 degrees. This peak represents the spindle-like structures that form in the dense phase. In fact, it has been proven that a hexagonal structure is not mechanically stable for a nonzero temperature [194]. Hence, these complicated steady state structures are a combination of kinetic constraints on bonding and on thermal noise.

Dynamical properties

Now that we have characterized the steady state properties of the system we would like to understand the dynamical properties and how they depend on the bonding kinetics. The dynamical results of the model are shown in Fig. 5.6. In Fig. 5.6a), a system above the critical temperature was quenched to a temperature in the phase separated region at $T/\bar{E}_B = 0.14$

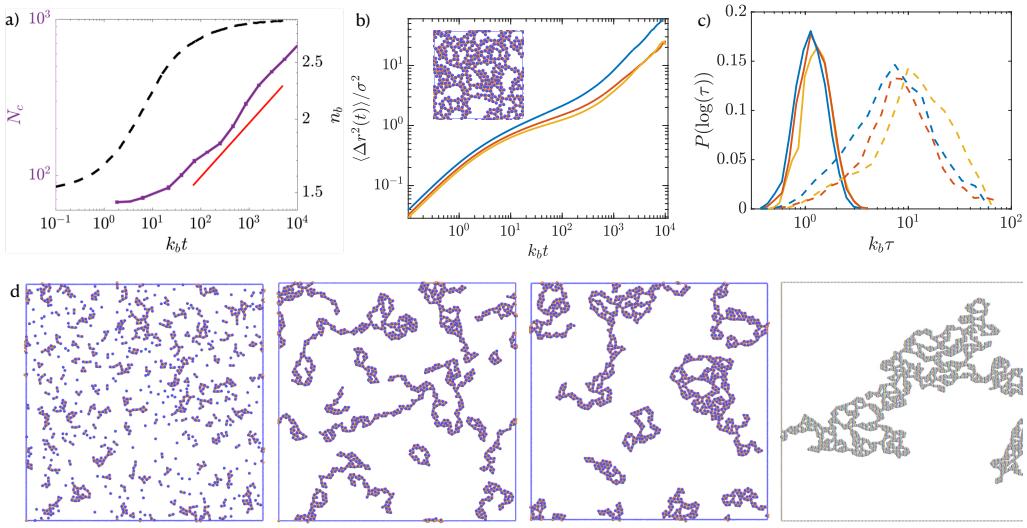

Figure 5.6: Simulation results of LAT model. a) The largest cluster size (purple solid line) with error bars from 11 independent runs and average bonds (black dashed line) as a function of time plotted on the log-log scale, with the fitted slope close to 1/3 for the largest cluster size versus time curve. b) The mean squared displacement as a function of time showing caging effects that become more distinct with decreasing temperature for $T/\bar{E}_B = 0.18$ (blue), 0.16 (red), and 0.14 (yellow). c) The distributions of persistence times (dashed line), the time to move a distance σ, and exchange times (solid line), the time to move another distance σ given that a LAT molecule has already moved a distance σ, for the same three temperatures in b). The lack of overlap between the two distributions shows that there is dynamic heterogeneity. d) The time evolution of aggregation as plotted in a) going from right to left panels show configurations for the start, early, middle, and last times of the simulation.

and the largest cluster size and average number of bonds were plotted as a function of time at each stage of the coarsening process. We find that the system eventually forms a large single cluster but with long times for campactification with a growth exponent of 1/3 consistent with Ostwald ripening [195, 196, 197]. Snapshots at different stages of the growth process are shown in Fig. 5.6d). At short times, the number of bonds quickly grow forming many small clusters as shown in the first panel. However, because of the kinetic constraints the second and third panels show that extended structures form at intermediate times with long structural reorganization times to campactify due to limited bond availability. The last snapshot in Fig. 5.6d) shows that the system does eventually form a single large cluster but with a spindle-like structure and at a density far from close packed at $\rho\sigma^2 = 0.38$. In Fig. 5.6b, the mean squared displacement of the dense phase is plotted as a function of time for a range of temperatures within the phase separated region which shows caging effects, marked by a decrease in slope at intermediate times, with the time to break their cage given

by the average time to break a bond. The inset shows a snapshot of the isolated condensed phase system. In Fig. 5.6c), the persistence time, the time for a molecule to travel their particle diameter, and the exchange time, the time to travel their diameter again given that they have already traveled their diameter is plotted [198]. It shows that LAT molecules are likely to keep moving once they break their cages to start moving, giving evidence of dynamical facilitation with a decade of time between the two distributions.

5.4 Summary

Based on experimental observations, a minimal model of 2 dimensional aggregation of LAT-Grb2-SOS complexes was devised. Simulations of the model show steady-state condensed phases being far from fully-packed and display spindle-like structures with no solid-like phase at low temperatures. Additionally, the results display caging effects in the mean squared displacement and evidence of dynamical facilitation shown by the decade of separation in the peaks of the persistence and exchange time distributions. In future works, we are curious to apply our modeling strategy to 3 dimensional protein droplet systems at the microscopic level, and explore possible differences in the kinetics. Since the model devised has minimal assumptions on the mechanism of condensation, it is believed that the model will describe generic features of 2 dimensional phase transitions within the cell.

Appendix A

Probability and stochastic variables

A.1 Fokker Plank

Let us expand a generic function $f[x(t),t]$ of the random variable $x(t)$ which satisfies the SDE (1.1) up to order $dW(t)$,

$$df[x(t),t] \overset{\alpha}{=} \frac{\partial f}{\partial t}dt + \frac{\partial f}{\partial x}dx + \frac{1}{2}\frac{\partial^2 f}{\partial x^2}dx^2 \ . \tag{A.1}$$

Our goal is to represent this equation as a function that is linear in dt. We can represent the SDE in the general α discretization as

$$dx \overset{\alpha}{=} F(\bar{x},t)dt + B(\bar{x},t)dW(t) \ . \tag{A.2}$$

One's first inclination might be to plug the SDE directly into (A.1) without modification but this would not give us the correct answer. This is because depending on the discretization (or integration rule) there will be more (or less) terms of order dt depending on our choice. Therefore, after plugging the SDE into the expansion of $f[x(t),t]$ we have to express $\bar{x}$ in terms of x by using Taylor expansions to get the correct terms up to order dt:

$$df[x(t),t] \overset{\alpha}{=} \frac{\partial f}{\partial t}dt + \frac{\partial f}{\partial x}[F(\bar{x},t)dt + B(\bar{x},t)dW(t)] + \frac{1}{2}\frac{\partial^2 f}{\partial x^2}[F(\bar{x},t)dt + B(\bar{x},t)dW(t)]^2. \tag{A.3}$$

Now expressing F and B in terms of x we get:

$$F(\bar{x},t) = F(x,t) + \mathcal{O}(dt) \ , \tag{A.4}$$

and

$$B(\bar{x},t) \overset{\alpha}{=} B(x,t) + \alpha\frac{dB(x,t)}{dx}\bigg|_{x=\bar{x}} dx + \mathcal{O}(dt) \ . \tag{A.5}$$

We use the fact that this is a Taylor series around $\bar{x} = x$, and use the fact that $(\bar{x} - x) = \alpha dx$ from (1.8). Note that in (A.4), since we are evaluating $F(\bar{x},t)$ at $\alpha = 0$, this is interpreted

as the Ito drift. Likewise, in (A.5) we are interpreting the noise amplitude $B(x,t)$ in the Ito sense and expanding $B(\bar{x},t)$ around $B(x,t)$. We go to first order in dx for $B(\bar{x},t)$ because there will be terms that will end up being of order dt. Now we can input the above equations into the expansion (A.3). We will do this term by term. The first term of (A.3) $\frac{\partial f}{\partial t}dt$ is already first order in dt so it will not change. The second term of (A.3) becomes

$$\frac{\partial f}{\partial x}[F(\bar{x},t)dt + B(\bar{x},t)dW(t)] \stackrel{\alpha}{=} \frac{\partial f}{\partial x}[F(x,t) + \left(B(x,t) + \alpha \frac{dB(x,t)}{dx}\bigg|_{x=\bar{x}} dx\right) dW(t)] \ . \quad \text{(A.6)}$$

The final expression of the second term of (A.3) is obtained by noting that

$$dx(t)dW(t) = F(\bar{x},t)dtdW(t) + B(\bar{x},t)dW^2 = B(x,t)dW^2 + \mathcal{O}(dt) = B(x,t)dt + \mathcal{O}(dt) \ . \quad \text{(A.7)}$$

With this the second term of (A.3) becomes

$$\frac{\partial f}{\partial x}[F(\bar{x},t)dt + B(\bar{x},t)dW(t)] \stackrel{\alpha}{=} \frac{\partial f}{\partial x}[F(x,t) + B(x,t)dW(t) + \alpha \frac{dB(x,t)}{dx}\bigg|_{x=\bar{x}} B(x,t)dt] \ . \quad \text{(A.8)}$$

Finally, the last term of (A.3) can be reduced by noting that

$$dx^2 = B^2(x,t)dW^2 + \mathcal{O}(dt) = B^2(x,t)dt + \mathcal{O}(dt) \ , \quad \text{(A.9)}$$

where we have expressed B to zeroth order in x because the α discretization adds terms of order dt so this is the contribution to lowest order. The last term then becomes

$$\frac{1}{2}\frac{\partial^2 f}{\partial x^2}dx^2 = B^2(x,t)\frac{1}{2}\frac{d^2 f}{dx^2} \ . \quad \text{(A.10)}$$

Putting all three terms together we get

$$df[x(t),t] \stackrel{\alpha}{=} \left[\frac{\partial f}{\partial t} + \frac{\partial f}{\partial x}F(x,t) + \alpha \frac{\partial f}{\partial x}\frac{dB(x,t)}{dx}\bigg|_{x=\bar{x}} B(x,t) + B^2(x,t)\frac{1}{2}\frac{d^2 f}{dx^2}\right] dt \quad \text{(A.11)}$$
$$+ \frac{\partial f}{\partial x}B(x,t)dW(t) \ .$$

This is called Ito's Lemma. Now we can use this result to derive the Fokker-Planck equation. If we assume the observable is independent of time explicitly, then we write the average of the function f as

$$\langle f[x(t)]\rangle = \int_{-\infty}^{\infty} f(x)P(x,t)dx \ . \quad \text{(A.12)}$$

Taking the time derivative gives

$$\frac{d\langle f[x(t)]\rangle}{dt} = \int_{-\infty}^{\infty} f(x)\frac{\partial P(x,t)}{\partial t}dx \ . \quad \text{(A.13)}$$

We can equate this to another form by explicitly taking the average of the time derivative of the function obtained earlier in the section:

$$\langle \frac{df[x(t)]}{dt} \rangle \stackrel{\alpha}{=} \int_{-\infty}^{\infty} \left[\frac{\partial f}{\partial x} F(x,t) + \alpha \frac{\partial f}{\partial x} \frac{dB(x,t)}{dx}\bigg|_{x=\bar{x}} B(x,t) + B^2 \frac{1}{2} \frac{d^2 f}{dx^2} \right] P(x,t) dx \ . \tag{A.14}$$

Integrating by parts once on the first two terms on the right and twice on the last term we get

$$\int_{-\infty}^{\infty} f \left[-\frac{\partial (F(x,t)P(x,t))}{\partial x} - \frac{\partial (\alpha B'(x,t)B(x,t)P(x,t))}{\partial x} + \frac{1}{2} \frac{\partial^2 (B(x,t)^2 P(x,t))}{\partial x^2} \right] dx \ . \tag{A.15}$$

Since averaging is a linear operation we have that $\langle \frac{df[x(t)]}{dt} \rangle = \frac{d\langle f[x(t)] \rangle}{dt}$. The Fokker-Planck equation becomes

We can generalize the diffusion constant to a tensor if there are multiple noise sources by

$$D_{ij} = \frac{1}{2} \sum_{k=1}^{n} B_{ik} B_{kj} \ . \tag{A.16}$$

A.2 Path Integral

We denote the realization of the noise at $t = 0$ as $H_0(x_0, x_{dt})$ and $X_1(x_0, \zeta_0)$ the realization of x_{dt}. Namely, $H_0(x_0, x_{dt})$ makes true the following equation

$$(x_{dt} - X_1(x_0, \zeta_0))\Big|_{\zeta_0 = H_0(x_0, x_{dt})} = 0 \ . \tag{A.17}$$

Defining the difference between the noise at $t = 0$ and its realization we get

$$M(\zeta_0, x_0, x_{dt}) = \zeta_0 - \frac{\frac{x_{dt} - x_0}{dt} - F(\bar{x})}{B(\bar{x})} \ . \tag{A.18}$$

We can do a change of variables on the delta function in the transition probability as

$$\delta M(\zeta_0, x_0, x_{dt}) = \frac{\delta(x_{dt} - X(x_0, \zeta_0))}{|\partial_{x_{dt}} M(\zeta_0, x_0, x_{dt})|} \ . \tag{A.19}$$

Rearranging, we get

$$\delta(x_{dt} - X(x_0, \zeta_0)) = \delta M(\zeta_0, x_0, x_{dt}) |\partial_{x_{dt}} M(\zeta_0, x_0, x_{dt})|. \tag{A.20}$$

We can reduce this by noting that

$$|\partial_{x_{dt}} M(\zeta_0, x_0, x_{dt})| = \partial_{x_{dt}} [\frac{\frac{x_{dt} - x_0}{dt} - F(\bar{x})}{B(\bar{x})}] \ . \tag{A.21}$$

Doing a Taylor expansion on the $\bar{x}$, we get

$$|\partial_{x_{dt}} M(\zeta_0, x_0, x_{dt})| = \frac{1}{B(\bar{x_0})dt}[1 - \alpha F'(\bar{x_0})dt - (x_{dt} - x_0 - F(\bar{x})dt)\alpha\frac{B'(\bar{x_0})}{B(\bar{x_0})}] \ . \tag{A.22}$$

Using the delta function, we can substitute for ζ_0 to get

$$\delta(x_{dt} - X(x_0, \zeta_0)) = \delta M(\zeta_0, x_0, x_{dt})|\partial_{x_{dt}} M(\zeta_0, x_0, x_{dt})| \tag{A.23}$$

$$= \frac{1}{B(\bar{x_0})dt}[1 - \alpha dt F'(\bar{x_0}) - \zeta_0 B'(\bar{x_0})\alpha dt] \ . \tag{A.24}$$

Exponentiation is nontrivial since $\zeta_t dt$ is of order $dt^{1/2}$. Using the fact that $\zeta_t^2 \to 2D$ as $dt \to 0$ in the L^2-norm sense (see section 3.2) we write that

$$\exp(A\zeta_0 dt - DA^2 dt) = 1 + A\zeta_0 dt + \mathcal{O}(dt) \ . \tag{A.25}$$

With these prescriptions, the exponentiation becomes

$$\delta(x_{dt} - X(x_0, \zeta_0)) = \frac{1}{|B(\bar{x_0})|dt} \exp(-\alpha dt F'(\bar{x_0}) - \zeta_0 B'(\bar{x_0})\alpha dt - D[B'(\bar{x_0})]^2\alpha^2 dt) \ . \tag{A.26}$$

Inserting this into the transition probability and noting that

$$P(\zeta_0) = \left(\frac{dt}{4\pi D}\right)^{1/2} \exp\left(-\frac{\zeta_0^2 dt}{4D}\right) \ , \tag{A.27}$$

and using the properties of the delta-function (See Appendix A)
we get

$$P(x_{dt}|x_0) \stackrel{\alpha}{=} \frac{1}{|B(\bar{x_0})|}\left(\frac{1}{4\pi D dt}\right)^{1/2} \int d\zeta_0 \exp\Big[- \alpha dt F'(\bar{x_0}) - \zeta_0 B'(\bar{x_0})\alpha dt$$
$$- D[B'(\bar{x_0})]^2\alpha^2 dt\Big] \exp\left(- \frac{\zeta_0^2 dt}{4D}\right) \ . \tag{A.28}$$

This is simply a Gaussian integral so the transition probability becomes

$$P(x_{dt}|x_0) \stackrel{\alpha}{=} \tag{A.29}$$

$$\frac{1}{|B(\bar{x_0})|}\left(\frac{1}{4\pi D dt}\right)^{1/2} \exp\left(-\frac{dt}{4D}\left[\frac{\frac{x_{dt}-x_0}{dt} - F(\bar{x_0}) + 2\alpha D B(\bar{x_0})B'(\bar{x_0})}{B(\bar{x_0})}\right]^2 - \alpha dt F(\bar{x_0})\right) . \tag{A.30}$$

Martin-Siggia-Rose-Janssen-DeDominicis

This formalism is used in quantum field theory, reaction-diffusion models, and lattice gas models in combination with fluctuating hydrodynamics. The specific connections will be left to another set of notes. It was originally constructed by the names of this section [199, 200, 201].

Let's consider an arbitrary functional of the trajectory $O[x_{t+dt}]$. The average of this quantity is

$$\langle O[x_{t+dt}]\rangle = \int D[x_{t+dt}]O[x_{t+dt}] \int d\zeta_t \delta(x_{t+dt} - X_1(\zeta_t))p(\zeta_t) \tag{A.31}$$

where $X_1(\zeta_t)$ is the realization of x_{t+dt}. We can define a new variable as

$$G = x_{t+dt} - X_1(\zeta_t) = x_{t+dt} - x_t - F(\bar{x}_t)dt + B(\bar{x}_t)\zeta_t dt \ . \tag{A.32}$$

We can do a change of variables on the delta function to get

$$\langle O[x_{t+dt}]\rangle = \int D[x_{t+dt}]O[x_{t+dt}] \int d\zeta_t \left|\frac{\delta G}{\delta x_{t+dt}}\right| \delta(G)p(\zeta_t) \ . \tag{A.33}$$

Using (1.57), the Jacobian becomes

$$\left|\frac{\delta G}{\delta x_{t+dt}}\right| = 1 - \alpha F'(\bar{x}_t)dt - \alpha B'(\bar{x}_t)\zeta_t dt \tag{A.34}$$

$$= \exp(-\alpha F'(\bar{x}_t)dt - \alpha B'(\bar{x}_t)\zeta_t dt - D\alpha^2[B'(\bar{x}_t)]^2 dt) \ . \tag{A.35}$$

Before we put all the parts together to calculate the average we want to represent the delta function as a Fourier series:

$$\delta(G) = \delta(x_{t+dt} - x_t - F(\bar{x}_t)dt + B(\bar{x}_t)\zeta_t dt) \tag{A.36}$$

$$= \int d\hat{x} \exp[-\hat{x}(x_{t+dt} - x_t - F(\bar{x}_t)dt + B(\bar{x}_t)\zeta_t dt)] \ . \tag{A.37}$$

We note once again that the probability of drawing a noise is (A.27) and that

$$\int d\zeta_t \left|\frac{\delta G}{\delta x_{t+dt}}\right| \delta(G)p(\zeta_t) \tag{A.38}$$

$$\propto \int d\hat{x} \exp\Bigg[- dt\hat{x}(\frac{x_{t+dt} - x_t}{dt} - F(\bar{x}_t) + 2\alpha D B'(\bar{x}_t)B(\bar{x}_t)) \tag{A.39}$$

$$+ [B(\bar{x}_t)]^2(\hat{x})^2 D dt - \alpha F'(\bar{x}_t)dt\Bigg] \ . \tag{A.40}$$

The path probability is obtained by setting the observable above to $O[x_{t+dt}] = 1$ in the average. We can represent the path probability as

$$p(x_{t+dt}|x_t) = \int D[x_{t+dt}, \hat{x}] \exp\Bigg[- dt\hat{x}(\frac{x_{t+dt} - x_t}{dt} - F(\bar{x}_t) + 2\alpha D B'(\bar{x}_t)B(\bar{x}_t)) \tag{A.41}$$

$$+ [B(\bar{x}_t)]^2(\hat{x})^2 D dt - \alpha F'(\bar{x}_t)dt\Bigg] \ . \tag{A.42}$$

Taking the limit as $dt \Rightarrow 0$, we get

$$p(x_T|x_0) = \tag{A.43}$$

$$\int D\left[x_t, \hat{x}\right] \exp\left[\int dt - \hat{x}\left(\dot{x}_t - F(x_t) + 2\alpha D B'(x_t)B(x_t)\right) + \left[B(x_t)\right]^2(\hat{x})^2 D - \alpha F'(x_t)\right] . \tag{A.44}$$

This transition probability can be written in the form of a classical action as

$$\int D[x_t, \hat{x}] \exp\left[-S(x, \hat{x})\right] \ , \tag{A.45}$$

with

$$S(x_t, \hat{x}) = \hat{x}\left[\dot{x}_t - F(x_t) + 2\alpha D B'(x_t)B(x_t)\right] - \left[B(x_t)\right]^2(\hat{x})^2 D + \alpha F'(x_t) \ . \tag{A.46}$$

One could solve for equations of motion for x_t and $\hat{x}$. This is called an instanton solution and represents the optimal trajectory in the low noise limit. In this case, the equations of motion for $\hat{x}$ represent the optimal realization of the noise. We note that the MSRJD and the Onsager-Machlup formulations are equivalent equations. In the MSRJD formalism we represent the delta function as a Fourier transform before integrating over the noise. If we integrate over $\hat{x}$ in MSRJD, we will get the Onsager-Machlap action. The MSRJD formulation is used for describing time or space correlations as Feynman diagrams.

Bibliography

[1] Pieter Rein ten Wolde et al. "Fundamental limits to cellular sensing". In: *Journal of Statistical Physics* 162.5 (2016), pp. 1395–1424.

[2] J Tailleur and ME Cates. "Statistical mechanics of interacting run-and-tumble bacteria". In: *Physical review letters* 100.21 (2008), p. 218103.

[3] William YC Huang et al. "Phosphotyrosine-mediated LAT assembly on membranes drives kinetic bifurcation in recruitment dynamics of the Ras activator SOS". In: *Proceedings of the National Academy of Sciences* 113.29 (2016), pp. 8218–8223.

[4] Lakshmi Balagopalan et al. "The linker for activation of T cells (LAT) signaling hub: from signaling complexes to microclusters". In: *Journal of Biological Chemistry* 290.44 (2015), pp. 26422–26429.

[5] Adam H Courtney, Wan-Lin Lo, and Arthur Weiss. "TCR signaling: mechanisms of initiation and propagation". In: *Trends in biochemical sciences* 43.2 (2018), pp. 108–123.

[6] Thomas Speck et al. "Dynamical mean-field theory and weakly non-linear analysis for the phase separation of active Brownian particles". In: *J. Chem. Phys.* 142.22 (2015). ISSN: 00219606.

[7] Marie D Harton and Eric Batchelor. "Determining the limitations and benefits of noise in gene regulation and signal transduction through single cell, microscopy-based analysis". In: *Journal of molecular biology* 429.8 (2017), pp. 1143–1154.

[8] Raphaël Chetrite and Hugo Touchette. "Nonequilibrium Markov processes conditioned on large deviations". In: *Annales Henri Poincaré*. Vol. 16. 9. Springer. 2015, pp. 2005–2057.

[9] P Hanggi et al. "Note on time evolution of non-Markov processes". In: *Journal of Statistical Physics* 18.2 (1978), pp. 155–159.

[10] NG Van Kampen. "Itô versus stratonovich". In: *Journal of Statistical Physics* 24.1 (1981), pp. 175–187.

[11] Crispin Gardiner. *Stochastic methods*. Vol. 4. springer Berlin, 2009.

[12] Hannes Risken. "Fokker-planck equation". In: *The Fokker-Planck Equation*. Springer, 1996, pp. 63–95.

[13] A. W. C. Lau and T. C. Lubensky. "State-dependent diffusion: Thermodynamic consistency and its path integral formulation". In: *Physical Review E* 76.1 (2007), p. 011123.

[14] Andre C Barato and Raphael Chetrite. "A formal view on level 2.5 large deviations and fluctuation relations". In: *Journal of Statistical Physics* 160.5 (2015), pp. 1154–1172.

[15] Johannes Hoppenau, Daniel Nickelsen, and Andreas Engel. "Level 2 and level 2.5 large deviation functionals for systems with and without detailed balance". In: *New journal of physics* 18.8 (2016), p. 083010.

[16] Leticia F Cugliandolo and Vivien Lecomte. "Rules of calculus in the path integral representation of white noise Langevin equations: the Onsager–Machlup approach". In: *Journal of Physics A: Mathematical and Theoretical* 50.34 (2017), p. 345001.

[17] Todd R Gingrich, Grant M Rotskoff, and Jordan M Horowitz. "Inferring dissipation from current fluctuations". In: *Journal of Physics A: Mathematical and Theoretical* 50.18 (2017), p. 184004.

[18] Christian Maes. *Non-dissipative effects in nonequilibrium systems*. Springer, 2018.

[19] Hugo Touchette. "The large deviation approach to statistical mechanics". In: *Physics Reports* 478.1-3 (2009), pp. 1–69.

[20] Raphaël Chetrite and Hugo Touchette. "Nonequilibrium microcanonical and canonical ensembles and their equivalence". In: *Physical review letters* 111.12 (2013), p. 120601.

[21] Raphaël Chetrite and Hugo Touchette. "Nonequilibrium microcanonical and canonical ensembles and their equivalence". In: *Phys. Rev. Lett.* 111.12 (2013), pp. 1–5. ISSN: 00319007.

[22] Joel. L. Lebowitz and Herbert Spohn. "A Gallavotti-Cohen Type Symmetry in the Large Deviation Functional for Stochastic Dynamics". In: *Phys. Rev. E* (1998), pp. 333–365. ISSN: 1572-9613. URL: `http://arxiv.org/abs/cond-mat/9811220%0Ahttp://dx.doi.org/10.1023/A:1004589714161`.

[23] Juan P. Garrahan and Igor Lesanovsky. "Thermodynamics of quantum jump trajectories". In: *Phys. Rev. Lett.* 104.16 (2010), pp. 1–4. ISSN: 00319007.

[24] Bernard Derrida and Tridib Sadhu. "Large deviations conditioned on large deviations I: Markov chain and Langevin equation". In: *Journal of Statistical Physics* 176.4 (2019), pp. 773–805.

[25] Trevor GrandPre and David T Limmer. "Current fluctuations of interacting active Brownian particles". In: *Physical Review E* 98.6 (2018), p. 060601.

[26] T. Speck and U. Seifert. "Restoring a fluctuation-dissipation theorem in a nonequilibrium steady state". In: *Europhys. Lett.* 74.3 (2006), pp. 391–396. ISSN: 02955075.

[27] J. Prost, J. F. Joanny, and J. M.R. Parrondo. "Generalized fluctuation-dissipation theorem for steady-state systems". In: *Phys. Rev. Lett.* 103.9 (2009), pp. 1–4. ISSN: 00319007.

[28] Marco Baiesi, Christian Maes, and Bram Wynants. "Fluctuations and response of nonequilibrium states". In: *Phys. Rev. Lett.* 103.1 (2009), pp. 1–4. ISSN: 00319007. DOI: 10.1103/PhysRevLett.103.010602.

[29] U. Seifert and T. Speck. "Fluctuation-dissipation theorem in nonequilibrium steady states". In: *Europhys. Lett.* 89.1 (2010). ISSN: 02955075.

[30] Raphaël Chetrite and Shamik Gupta. "Two Refreshing Views of Fluctuation Theorems Through Kinematics Elements and Exponential Martingale". In: *J. Stat. Phys.* 143.3 (2011), pp. 543–584. ISSN: 00224715.

[31] M. Baiesi and C. Maes. "An update on the nonequilibrium linear response". In: *New J. Phys.* 15 (2013). ISSN: 13672630.

[32] Christian Maes. "On the Second Fluctuation-Dissipation Theorem for Nonequilibrium Baths". In: *J. Stat. Phys.* 154.3 (2014), pp. 705–722. ISSN: 00224715.

[33] Denis J. Evans and Debra J. Searles. "Equilibrium microstates which generate second law violating steady states". In: *Phys. Rev. E* 50.2 (1994), pp. 1645–1648. ISSN: 1063651X. DOI: 10.1103/PhysRevE.50.1645.

[34] Jorge Kurchan. "Fluctuation theorem for stochastic dynamics". In: *Phys. Rev. E* (1997). ISSN: 0305-4470. URL: http://arxiv.org/abs/cond-mat/9709304%0Ahttp://dx.doi.org/10.1088/0305-4470/31/16/003.

[35] Gavin E Crooks. "Entropy production fluctuation theorem and the nonequilibrium work relation for free energy differences". In: *Physical Review E* 60.3 (1999), p. 2721.

[36] Udo Seifert. "Entropy production along a stochastic trajectory and an integral fluctuation theorem". In: *Physical review letters* 95.4 (2005), p. 040602.

[37] Christopher Jarzynski. "Nonequilibrium equality for free energy differences". In: *Physical Review Letters* 78.14 (1997), p. 2690.

[38] Giovanni Gallavotti and Ezechiel Godert David Cohen. "Dynamical ensembles in nonequilibrium statistical mechanics". In: *Physical review letters* 74.14 (1995), p. 2694.

[39] Andre C Barato and Udo Seifert. "Thermodynamic uncertainty relation for biomolecular processes". In: *Physical review letters* 114.15 (2015), p. 158101.

[40] Todd R Gingrich et al. "Dissipation bounds all steady-state current fluctuations". In: *Physical review letters* 116.12 (2016), p. 120601.

[41] Matteo Polettini, Alexandre Lazarescu, and Massimiliano Esposito. "Tightening the uncertainty principle for stochastic currents". In: *Phys. Rev. E* 94.5 (2016), pp. 1–10. ISSN: 24700053.

[42] Trevor GrandPre et al. "Entropy production fluctuations encode collective behavior in active matter". In: *Physical Review E* 103.1 (2021), p. 012613.

[43] Raphaël Chetrite and Hugo Touchette. "Nonequilibrium Markov Processes Conditioned on Large Deviations". In: *Ann. Hen. P.* 16.9 (2015), pp. 2005–2057. ISSN: 14240637.

[44] Thomas Speck. "Thermodynamic formalism and linear response theory for nonequilibrium steady states". In: *Phys. Rev. E* 94.2 (2016), pp. 1–6. ISSN: 24700053.

[45] Chloe Ya Gao and David T. Limmer. "Transport coefficients from large deviation functions". In: *Entropy* 19.11 (2017), pp. 1–16. ISSN: 10994300.

[46] Pierre Gaspard and Raymond Kapral. "Communication: Mechanochemical fluctuation theorem and thermodynamics of self-phoretic motors". In: *The Journal of chemical physics* 147.21 (2017), p. 211101.

[47] Chloe Ya Gao and David T Limmer. "Nonlinear transport coefficients from large deviation functions". In: *The Journal of chemical physics* 151.1 (2019), p. 014101.

[48] Michael E. Cates and Julien Tailleur. "Motility-Induced Phase Separation". In: *Ann. Rev. Cond. Mat. Phys.* 6.1 (2015), pp. 219–244. ISSN: 1947-5454. URL: `http://www.annualreviews.org/doi/10.1146/annurev-conmatphys-031214-014710`.

[49] Ahmad K Omar et al. "Active Crystallization". In: *arXiv preprint arXiv:2012.09803* (2020).

[50] Volker Schaller et al. "Polar patterns of driven filaments". In: *Nature* 467.7311 (2010), pp. 73–77. ISSN: 14764687. URL: `http://dx.doi.org/10.1038/nature09312`.

[51] Yutaka Sumino et al. "Large-scale vortex lattice emerging from collectively moving microtubules". In: *Nature* 483.7390 (2012), pp. 448–452. ISSN: 00280836.

[52] V. Schaller et al. "Frozen steady states in active systems". In: *Proc. Natl. Acad. Sci. U.S.A.* 108.48 (2011), pp. 19183–19188. ISSN: 0027-8424. URL: `http://www.pnas.org/cgi/doi/10.1073/pnas.1107540108`.

[53] Howard C. Berg and Douglas A. Brown. "Chemotaxis in Escherichia coli analysed by three-dimensional tracking". In: *Nature* 239.5374 (1972), pp. 500–504. ISSN: 00280836.

[54] James A. Shapiro. "The significances of bacterial colony patterns". In: *BioEssays* 17.7 (1995), pp. 597–607. ISSN: 15211878.

[55] Christopher Dombrowski et al. "Self-concentration and large-scale coherence in bacterial dynamics". In: *Phys. Rev. Lett.* 93.9 (2004), pp. 2–5. ISSN: 00319007. DOI: `10.1103/PhysRevLett.93.098103`.

[56] Jane Hill et al. "Hydrodynamic surface interactions enable escherichia coli to seek efficient routes to swim upstream". In: *Phys. Rev. Lett.* 98.6 (2007), pp. 1–4. ISSN: 00319007.

[57] Eric Lauga et al. "Swimming in circles: Motion of bacteria near solid boundaries". In: *Biophys. J.* 90.2 (2006), pp. 400–412. ISSN: 00063495. URL: http://dx.doi.org/10.1529/biophysj.105.069401.

[58] Xiongfei Fu et al. "Stripe formation in bacterial systems with density-suppressed motility". In: *Phys. Rev. Lett.* 108.19 (2012), pp. 1–5. ISSN: 00319007.

[59] Matthew R. Parsek and E. P. Greenberg. "Sociomicrobiology: The connections between quorum sensing and biofilms". In: *Trends Microbiol.* 13.1 (2005), pp. 27–33. ISSN: 0966842X.

[60] Jeremie Palacci et al. "Colloidal Surfers". In: *Science* 339.February (2013), pp. 936–939. ISSN: 0036-8075. URL: http://www.sciencemag.org/content/339/6122/936.full.pdf.

[61] Vijay Narayan, Narayanan Menon, and Sriram Ramaswamy. "Nonequilibrium steady states in a vibrated-rod monolayer: Tetratic, nematic, and smectic correlations". In: *J. Stat. Mech.* 1 (2006). ISSN: 17425468.

[62] Jonathan R. Howse et al. "Self-Motile Colloidal Particles: From Directed Propulsion to Random Walk". In: *Phys. Rev. Lett.* 99.4 (2007), pp. 8–11. ISSN: 00319007.

[63] Andreas Walther and Axel H E Müller. "Janus particles". In: *Soft Matter* 4.4 (2008), p. 663. ISSN: 1744-683X. URL: http://xlink.rsc.org/?DOI=b718131k.

[64] Antoine Bricard et al. "Emergence of macroscopic directed motion in populations of motile colloids". In: *Nature* 503.7474 (2013), pp. 95–98. ISSN: 00280836. DOI: 10.1038/nature12673. URL: http://dx.doi.org/10.1038/nature12673.

[65] Caleb G Wagner, Michael F Hagan, and Aparna Baskaran. "Steady-state distributions of ideal active Brownian particles under confinement and forcing". In: *J. Stat. Mech.* 2017.4 (2017), p. 43203.

[66] John D Weeks, David Chandler, and Hans C Andersen. "Role of repulsive forces in determining the equilibrium structure of simple liquids". In: *The Journal of chemical physics* 54.12 (1971), pp. 5237–5247.

[67] J P Hansen and I R McDonald. "Theory of Simple Liquids". In: *Elsevier* (1977).

[68] C. Appert-Rolland et al. "Universal cumulants of the current in diffusive systems on a ring". In: *Phys. Rev. E* 78.2 (2008), pp. 1–16. ISSN: 15393755. DOI: 10.1103/PhysRevE.78.021122.

[69] Lester O Hedges et al. "Dynamic Order-Disorder in Atomistic". In: 323.March (2009), pp. 1309–1314.

[70] Julian Bialké, Hartmut Löwen, and Thomas Speck. "Microscopic theory for the phase separation of self-propelled repulsive disks". In: *Euro Phys. Lett.* 103.3 (2013). ISSN: 02955075.

[71] Benjamin Hancock and Aparna Baskaran. "Statistical mechanics and hydrodynamics of self-propelled hard spheres". In: *J. Stat. Mech.* 2017.3 (2017). ISSN: 17425468.

[72] Raphael Wittkowski, Joakim Stenhammar, and Michael E. Cates. "Nonequilibrium dynamics of mixtures of active and passive particles". In: *Phys. Rev. E* (2017), pp. 1–17. ISSN: 1367-2630.

[73] Milton Abramowitz, Irene A. Stegun, and David Miller. "Handbook of Mathematical Functions With Formulas, Graphs and Mathematical Tables". In: *J. App. Mech.* 32.1 (1965), p. 239. URL: http://appliedmechanics.asmedigitalcollection.asme.org/article.aspx?articleid=1396937.

[74] Patrick Pietzonka, Kevin Kleinbeck, and Udo Seifert. "Extreme fluctuations of active Brownian motion". In: *New J. Phys.* 18.5 (2016). ISSN: 13672630.

[75] Ushnish Ray, Garnet Kin Chan, and David T Limmer. "Exact fluctuations of nonequilibrium steady states from approximate auxiliary dynamics". In: *Phys. Rev. Lett.* (2018).

[76] Stefano Steffenoni, Gianmaria Falasco, and Klaus Kroy. "Microscopic derivation of the hydrodynamics of active-Brownian-particle suspensions". In: *Phys. Rev. E* 95.5 (2017), p. 052142. ISSN: 2470-0045. URL: http://link.aps.org/doi/10.1103/PhysRevE.95.052142.

[77] Alexandre P. Solon et al. "Pressure and phase equilibria in interacting active Brownian spheres". In: *Phys. Rev. Lett.* 114.19 (2015), pp. 1–6.

[78] Sho C. Takatori and John F. Brady. "A theory for the phase behavior of mixtures of active particles". In: *Soft Matter* 11.40 (2015), pp. 7920–7931. ISSN: 1744-683X. URL: http://xlink.rsc.org/?DOI=C5SM01792K.

[79] Jérémie Palacci et al. "Sedimentation and effective temperature of active colloidal suspensions". In: *Phys. Rev. Lett.* 105.8 (2010), pp. 1–4. ISSN: 00319007.

[80] Bo Wang et al. "When Brownian diffusion is not Gaussian". In: *Nature Materials* 11.6 (2012), pp. 481–485. URL: http://dx.doi.org/10.1038/nmat3308.

[81] Björn Stuhrmann et al. "Nonequilibrium fluctuations of a remodeling in vitro cytoskeleton". In: *Phys. Rev. E* 86.2 (2012), pp. 1–5.

[82] Alexandre P Solon et al. "Pressure and phase equilibria in interacting active Brownian spheres". In: *Physical review letters* 114.19 (2015), p. 198301.

[83] Thomas Speck and Robert L Jack. "Ideal bulk pressure of active Brownian particles". In: *Physical Review E* 93.6 (2016), p. 062605.

[84] Joakim Stenhammar et al. "Phase behaviour of active Brownian particles: the role of dimensionality". In: *Soft Matter* 10.10 (2014), pp. 1489–1499. ISSN: 1744-683X. URL: http://xlink.rsc.org/?DOI=C3SM52813H.

[85] Subhadip Chakraborti, Shradha Mishra, and Punyabrata Pradhan. "Additivity, density fluctuations, and nonequilibrium thermodynamics for active Brownian particles". In: *Physical Review E* 93.5 (2016), p. 052606.

[86] Yaouen Fily and M. Cristina Marchetti. "Athermal phase separation of self-propelled particles with no alignment". In: *Phys. Rev. Lett.* 108.23 (2012), pp. 1–5. ISSN: 00319007.

[87] Hannes Risken and Till Frank. "The Fokker-Planck Equation: Methods of Solutions and Applications (Springer Series in Synergetics)". In: *Springer* (1996). URL: http://www.amazon.ca/exec/obidos/redirect?tag=citeulike09-20&path=ASIN/354061530X.

[88] Xu Zheng et al. "Non-Gaussian statistics for the motion of self-propelled Janus particles: Experiment versus theory". In: *Phys. Rev. E* 88.3 (2013), pp. 1–11.

[89] Chong Wai Io et al. "Experimental investigation of mesoscopic heterogeneous motion of laser-activated self-propelling Janus particles in suspension". In: *Phys. Rev. E* 96.6 (2017), pp. 1–5.

[90] Stephen Whitelam, Katherine Klymko, and Dibyendu Mandal. "Phase separation and large deviations of lattice active matter". In: *Journal of Chemical Physics* 148.15 (2018). ISSN: 00219606. DOI: 10.1063/1.5023403.

[91] Robert L. Jack, Ian R. Thompson, and Peter Sollich. "Hyperuniformity and phase separation in biased ensembles of trajectories for diffusive systems". In: *Physical Review Letters* 114.6 (2015), pp. 1–5. ISSN: 10797114. DOI: 10.1103/PhysRevLett.114.060601.

[92] E. Pitard, V. Lecomte, and F. Van Wijland. "Dynamic transition in an atomic glass former: A molecular-dynamics evidence". In: *Epl* 96.5 (2011). ISSN: 02955075. DOI: 10.1209/0295-5075/96/56002.

[93] J. P. Garrahan et al. "Dynamical first-order phase transition in kinetically constrained models of glasses". In: *Physical Review Letters* 98.19 (2007), pp. 0–3. ISSN: 00319007. DOI: 10.1103/PhysRevLett.98.195702.

[94] Shachi Katira, Juan P. Garrahan, and Kranthi K. Mandadapu. "Solvation in Space-Time: Pre-transition Effects in Trajectory Space". In: *Phys. Rev. Lett.* 120.26 (2017), p. 260602. URL: http://arxiv.org/abs/1710.04747.

[95] Dibyendu Mandal, Katherine Klymko, and Michael R. DeWeese. "Entropy Production and Fluctuation Theorems for Active Matter". In: *Phys. Rev. Lett.* 119.25 (2017), pp. 1–6.

[96] Étienne Fodor et al. "How far from equilibrium is active matter?" In: *Physical review letters* 117.3 (2016), p. 038103.

[97] Jakob Mehl, Thomas Speck, and Udo Seifert. "Large deviation function for entropy production in driven one-dimensional systems". In: *Phys. Rev. E* 78.1 (2008), pp. 1–4.

[98] Thomas Speck, Andreas Engel, and Udo Seifert. "The large deviation function for entropy production: The optimal trajectory and the role of fluctuations". In: *J. Stat. Mech.* 2012.12 (2012).

[99] Ethan Levien, Trevor GrandPre, and Ariel Amir. "Large Deviation Principle Linking Lineage Statistics to Fitness in Microbial Populations". In: *Physical Review Letters* 125.4 (2020), p. 048102.

[100] Yaouen Fily, Silke Henkes, and M. Cristina Marchetti. "Freezing and phase separation of self-propelled disks". In: *Soft Matter* 10.13 (2014), pp. 2132–2140. ISSN: 1744-683X. URL: http://xlink.rsc.org/?DOI=C3SM52469H.

[101] D. Andrieux and P. Gaspard. "Fluctuation theorem and Onsager reciprocity relations". In: *J. Chem. Phys.* 121.13 (2004), pp. 6167–6174. ISSN: 00219606. DOI: 10.1063/1.1782391.

[102] Ivan Di Terlizzi and Marco Baiesi. "Kinetic uncertainty relation". In: *Journal of Physics A: Mathematical and Theoretical* 52.2 (2018), 02LT03.

[103] Jeremy A Owen, Todd R Gingrich, and Jordan M Horowitz. "Universal thermodynamic bounds on nonequilibrium response with biochemical applications". In: *Physical Review X* 10.1 (2020), p. 011066.

[104] Cesare Nardini and Hugo Touchette. "Process interpretation of current entropic bounds". In: *The European Physical Journal B* 91.1 (2018), p. 16.

[105] Andreas Dechant and Shin-ichi Sasa. "Fluctuation–response inequality out of equilibrium". In: *Proceedings of the National Academy of Sciences* 117.12 (2020), pp. 6430–6436.

[106] Matteo Polettini and Massimiliano Esposito. "Effective fluctuation and response theory". In: *Journal of Statistical Physics* 176.1 (2019), pp. 94–168.

[107] Maximilien Barbier and Pierre Gaspard. "Microreversibility, nonequilibrium current fluctuations, and response theory". In: *Journal of Physics A: Mathematical and Theoretical* 51.35 (2018), p. 355001.

[108] Caleb G Wagner, Michael F Hagan, and Aparna Baskaran. "Response of active Brownian particles to boundary driving". In: *Physical Review E* 100.4 (2019), p. 042610.

[109] Kiryl Asheichyk et al. "Response of active Brownian particles to shear flow". In: *The Journal of chemical physics* 150.14 (2019), p. 144111.

[110] Sara Dal Cengio, Demian Levis, and Ignacio Pagonabarraga. "Linear response theory and Green-Kubo relations for active matter". In: *Physical Review Letters* 123.23 (2019), p. 238003.

[111] Lorenzo Caprini, Umberto Marini Bettolo Marconi, and Angelo Vulpiani. "Linear response and correlation of a self-propelled particle in the presence of external fields". In: *Journal of Statistical Mechanics: Theory and Experiment* 2018.3 (2018), p. 033203.

[112] Zhenghan Liao et al. "A mechanism for anomalous transport in chiral active liquids". In: *The Journal of chemical physics* 151.19 (2019), p. 194108.

[113] M. E. Cates and J. Tailleur. "When are active Brownian particles and run-and-tumble particles equivalent? Consequences for motility-induced phase separation". In: *Europhys. Lett.* 101.2 (2013). ISSN: 02955075.

[114] Gabriel S Redner, Michael F Hagan, and Aparna Baskaran. "Structure and dynamics of a phase-separating active colloidal fluid". In: *Physical review letters* 110.5 (2013), p. 055701.

[115] Pelerine Tsobgni Nyawo and Hugo Touchette. "A minimal model of dynamical phase transition". In: *EPL (Europhysics Letters)* 116.5 (2017), p. 50009.

[116] Pelerine Tsobgni Nyawo and Hugo Touchette. "Dynamical phase transition in drifted Brownian motion". In: *Physical Review E* 98.5 (2018), p. 052103.

[117] Sophie Hermann and Matthias Schmidt. "Active ideal sedimentation: exact two-dimensional steady states". In: *Soft Matter* 14.9 (2018), pp. 1614–1621.

[118] Alexandre P Solon, Michael E Cates, and Julien Tailleur. "Active brownian particles and run-and-tumble particles: A comparative study". In: *The European Physical Journal Special Topics* 224.7 (2015), pp. 1231–1262.

[119] Chiu Fan Lee. "Active particles under confinement: aggregation at the wall and gradient formation inside a channel". In: *New Journal of Physics* 15.5 (2013), p. 055007.

[120] Ahmad K Omar et al. "Phase Diagram of Active Brownian Spheres: Crystallization and the Metastability of Motility-Induced Phase Separation". In: *Physical Review Letters* 126.18 (2021), p. 188002.

[121] Cesare Nardini et al. "Entropy production in field theories without time-reversal symmetry: quantifying the non-equilibrium character of active matter". In: *Physical Review X* 7.2 (2017), p. 021007.

[122] Étienne Fodor, Takahiro Nemoto, and Suriyanarayanan Vaikuntanathan. "Dissipation controls transport and phase transitions in active fluids: mobility, diffusion and biased ensembles". In: *New Journal of Physics* 22.1 (2020), p. 013052.

[123] Clara del Junco, Laura Tociu, and Suriyanarayanan Vaikuntanathan. "Energy dissipation and fluctuations in a driven liquid". In: *Proceedings of the National Academy of Sciences* 115.14 (2018), pp. 3569–3574.

[124] Pierre Gaspard and Raymond Kapral. "Fluctuating chemohydrodynamics and the stochastic motion of self-diffusiophoretic particles". In: *The Journal of chemical physics* 148.13 (2018), p. 134104.

[125] Kinjal Dasbiswas, Kranthi K Mandadapu, and Suriyanarayanan Vaikuntanathan. "Topological localization in out-of-equilibrium dissipative systems". In: *Proceedings of the National Academy of Sciences* 115.39 (2018), E9031–E9040.

[126] Vishal Soni et al. "The odd free surface flows of a colloidal chiral fluid". In: *Nature Physics* 15.11 (2019), pp. 1188–1194.

[127] Zhenghan Liao, William TM Irvine, and Suriyanarayanan Vaikuntanathan. "Rectification in Nonequilibrium Parity Violating Metamaterials". In: *Physical Review X* 10.2 (2020), p. 021036.

[128] Fernando Caballero and Michael E. Cates. "Stealth Entropy Production in Active Field Theories near Ising Critical Points". In: *Phys. Rev. Lett.* 124 (24 June 2020), p. 240604. DOI: 10.1103/PhysRevLett.124.240604. URL: https://link.aps.org/doi/10.1103/PhysRevLett.124.240604.

[129] Dibyendu Mandal, Katherine Klymko, and Michael R DeWeese. "Entropy production and fluctuation theorems for active matter". In: *Physical review letters* 119.25 (2017), p. 258001.

[130] Luuk Metselaar, Julia M Yeomans, and Amin Doostmohammadi. "Topology and morphology of self-deforming active shells". In: *Physical Review Letters* 123.20 (2019), p. 208001.

[131] Yao Li and Pieter Rein ten Wolde. "Shape Transformations of Vesicles Induced by Swim Pressure". In: *Physical review letters* 123.14 (2019), p. 148003.

[132] Chao Wang et al. "Shape transformation and manipulation of a vesicle by active particles". In: *The Journal of chemical physics* 150.4 (2019), p. 044907.

[133] Richard G Morris and Madan Rao. "Active morphogenesis of epithelial monolayers". In: *Physical Review E* 100.2 (2019), p. 022413.

[134] Nicolas Bain and Denis Bartolo. "Dynamic response and hydrodynamics of polarized crowds". In: *Science* 363.6422 (2019), pp. 46–49.

[135] Alexandre Morin and Denis Bartolo. "Flowing active liquids in a pipe: Hysteretic response of polar flocks to external fields". In: *Physical Review X* 8.2 (2018), p. 021037.

[136] Antoine Bricard et al. "Emergence of macroscopic directed motion in populations of motile colloids". In: *Nature* 503.7474 (2013), pp. 95–98.

[137] Alexander Mietke et al. "Minimal model of cellular symmetry breaking". In: *Physical review letters* 123.18 (2019), p. 188101.

[138] Alexander Morozov. "From chaos to order in active fluids". In: *Science* 355.6331 (2017), pp. 1262–1263.

[139] Anton Souslov et al. "Topological sound in active-liquid metamaterials". In: *Nature Physics* 13.11 (2017), pp. 1091–1094.

[140] Chad Ropp et al. "Dissipative self-organization in optical space". In: *Nature Photonics* 12.12 (2018), pp. 739–743.

[141] Sho C Takatori and Amaresh Sahu. "Active Contact Forces Drive Nonequilibrium Fluctuations in Membrane Vesicles". In: *Physical Review Letters* 124.15 (2020), p. 158102.

[142] Debasish Chaudhuri. "Active brownian particles: Entropy production and fluctuation response". In: *Physical Review E* 90.2 (2014), p. 022131.

[143] Patrick Pietzonka et al. "Autonomous Engines Driven by Active Matter: Energetics and Design Principles". In: *Phys. Rev. X* 9 (4 Nov. 2019), p. 041032. DOI: 10.1103/PhysRevX.9.041032. URL: https://link.aps.org/doi/10.1103/PhysRevX.9.041032.

[144] Sudeesh Krishnamurthy et al. "A micrometre-sized heat engine operating between bacterial reservoirs". In: *Nature Physics* 12.12 (2016), p. 1134.

[145] Ruben Zakine et al. "Stochastic Stirling engine operating in contact with active baths". In: *Entropy* 19.5 (2017), p. 193.

[146] D Martin et al. "Extracting maximum power from active colloidal heat engines". In: *EPL (Europhysics Letters)* 121.6 (2018), p. 60005.

[147] Arnab Saha et al. "Stochastic heat engine powered by active dissipation". In: *Journal of Statistical Mechanics: Theory and Experiment* 2018.11 (2018), p. 113203.

[148] Timothy Ekeh, Michael E. Cates, and Étienne Fodor. "Thermodynamic cycles with active matter". In: *Phys. Rev. E* 102 (1 July 2020), p. 010101. DOI: 10.1103/PhysRevE.102.010101. URL: https://link.aps.org/doi/10.1103/PhysRevE.102.010101.

[149] Subhasish Chaki and Rajarshi Chakrabarti. "Entropy production and work fluctuation relations for a single particle in active bath". In: *Physica A: Statistical Mechanics and its Applications* 511 (2018), pp. 302–315.

[150] Jordan M Horowitz and Todd R Gingrich. "Thermodynamic uncertainty relations constrain non-equilibrium fluctuations". In: *Nature Physics* (2019), pp. 1–6.

[151] Jeffrey M Epstein and Kranthi K Mandadapu. "Time-reversal symmetry breaking in two-dimensional nonequilibrium viscous fluids". In: *Physical Review E* 101.5 (2020), p. 052614.

[152] Cory Hargus et al. "Time reversal symmetry breaking and odd viscosity in active fluids: Green–Kubo and NEMD results". In: *The Journal of Chemical Physics* 152.20 (2020), p. 201102.

[153] Holger Merlitz et al. "Linear response approach to active Brownian particles in time-varying activity fields". In: *The Journal of Chemical Physics* 148.19 (2018), p. 194116.

[154] Todd R. Gingrich et al. "Dissipation Bounds All Steady-State Current Fluctuations". In: *Phys. Rev. Lett.* 116 (12 Mar. 2016), p. 120601. DOI: 10.1103/PhysRevLett.116.120601. URL: https://link.aps.org/doi/10.1103/PhysRevLett.116.120601.

[155] Yaouen Fily, Aparna Baskaran, and Michael F Hagan. "Equilibrium mappings in polar-isotropic confined active particles". In: *The European Physical Journal E* 40.6 (2017), pp. 1–9.

[156] Hartmut Löwen. "Active colloidal molecules". In: *EPL (Europhysics Letters)* 121.5 (2018), p. 58001.

[157] Roland G Winkler. "Dynamics of flexible active Brownian dumbbells in the absence and the presence of shear flow". In: *Soft matter* 12.16 (2016), pp. 3737–3749.

[158] Joel Lebowitz and Herbert Spohn. "A gallavotti-cohen-type symmetry in the large deviation functional for stochastic dynamics". In: *Journal of Statistical Physics* 95.1-2 (1999), pp. 333–365.

[159] Christian Maes and Karel Netočn. "Time-reversal and entropy". In: *Journal of statistical physics* 110.1-2 (2003), pp. 269–310.

[160] Lorenzo Caprini et al. "The entropy production of Ornstein–Uhlenbeck active particles: a path integral method for correlations". In: *Journal of Statistical Mechanics: Theory and Experiment* 2019.5 (2019), p. 053203.

[161] Subhasish Chaki and Rajarshi Chakrabarti. "Effects of active fluctuations on energetics of a colloidal particle: Superdiffusion, dissipation and entropy production". In: *Physica A: Statistical Mechanics and its Applications* 530 (2019), p. 121574.

[162] Francesco Cagnetta et al. "Large fluctuations and dynamic phase transition in a system of self-propelled particles". In: *Physical review letters* 119.15 (2017), p. 158002.

[163] Takahiro Nemoto et al. "Optimizing active work: Dynamical phase transitions, collective motion, and jamming". In: *Physical Review E* 99.2 (2019), p. 022605.

[164] Suraj Shankar and M Cristina Marchetti. "Hidden entropy production and work fluctuations in an ideal active gas". In: *Physical Review E* 98.2 (2018), p. 020604.

[165] Grzegorz Szamel. "Stochastic thermodynamics for self-propelled particles". In: *Physical Review E* 100.5 (2019), p. 050603.

[166] Patrick Pietzonka and Udo Seifert. "Entropy production of active particles and for particles in active baths". In: *Journal of Physics A: Mathematical and Theoretical* 51.1 (2017), 01LT01.

[167] Lennart Dabelow, Stefano Bo, and Ralf Eichhorn. "Irreversibility in active matter systems: Fluctuation theorem and mutual information". In: *Physical Review X* 9.2 (2019), p. 021009.

[168] Thomas Speck. "Stochastic thermodynamics with reservoirs: Sheared and active colloidal particles". In: *arXiv preprint arXiv* 1707 (2017).

[169] Cristian Giardina, Jorge Kurchan, and Luca Peliti. "Direct evaluation of large-deviation functions". In: *Physical review letters* 96.12 (2006), p. 120603.

[170] Hugo Touchette. "Introduction to dynamical large deviations of Markov processes". In: *Physica A: Statistical Mechanics and its Applications* 504 (2018), pp. 5–19.

[171] Raphaël Chetrite and Hugo Touchette. "Variational and optimal control representations of conditioned and driven processes". In: *Journal of Statistical Mechanics: Theory and Experiment* 2015.12 (2015), P12001.

[172] F Cagnetta and E Mallmin. "Efficiency of one-dimensional active transport conditioned on motility". In: *Physical Review E* 101.2 (2020), p. 022130.

[173] Yann-Edwin Keta et al. "Collective motion in large deviations of active particles". In: *Physical Review E* 103.2 (2021), p. 022603.

[174] Pietro Chiarantoni et al. "Work fluctuations of self-propelled particles in the phase separated state". In: *Journal of Physics A: Mathematical and Theoretical* (2020).

[175] David S Dean. "Langevin equation for the density of a system of interacting Langevin processes". In: *Journal of Physics A: Mathematical and General* 29.24 (1996), p. L613.

[176] Jakub Dolezal and Robert L Jack. "Large deviations and optimal control forces for hard particles in one dimension". In: *Journal of Statistical Mechanics: Theory and Experiment* 2019.12 (2019), p. 123208.

[177] Avishek Das and David T Limmer. "Variational control forces for enhanced sampling of nonequilibrium molecular dynamics simulations". In: *The Journal of Chemical Physics* 151.24 (2019), p. 244123.

[178] Laura Tociu et al. "How Dissipation Constrains Fluctuations in Nonequilibrium Liquids: Diffusion, Structure, and Biased Interactions". In: *Physical Review X* 9.4 (2019), p. 041026.

[179] Emanuele Crosato, Mikhail Prokopenko, and Richard E Spinney. "Irreversibility and emergent structure in active matter". In: *Physical Review E* 100.4 (2019), p. 042613.

[180] Ramil Nigmatullin and Mikhail Prokopenko. "Thermodynamic efficiency of interactions in self-organizing systems". In: *arXiv:1912.08948* (2019).

[181] Anthony A Hyman, Christoph A Weber, and Frank Jülicher. "Liquid-liquid phase separation in biology". In: *Annual review of cell and developmental biology* 30 (2014), pp. 39–58.

[182] Salman F Banani et al. "Biomolecular condensates: organizers of cellular biochemistry". In: *Nature reviews Molecular cell biology* 18.5 (2017), pp. 285–298.

[183] Joel Berry, Clifford P Brangwynne, and Mikko Haataja. "Physical principles of intracellular organization via active and passive phase transitions". In: *Reports on Progress in Physics* 81.4 (2018), p. 046601.

[184] Simon Alberti, Amy Gladfelter, and Tanja Mittag. "Considerations and challenges in studying liquid-liquid phase separation and biomolecular condensates". In: *Cell* 176.3 (2019), pp. 419–434.

[185] Lindsay B Case, Jonathon A Ditlev, and Michael K Rosen. "Regulation of transmembrane signaling by phase separation". In: *Annual review of biophysics* 48 (2019), pp. 465–494.

[186] Wilton T Snead et al. "Membrane surfaces regulate assembly of a ribonucleoprotein condensate". In: *bioRxiv* (2021).

[187] William YC Huang et al. "Allosteric modulation of Grb2 recruitment to the intrinsically disordered scaffold protein, LAT, by remote site phosphorylation". In: *Journal of the American Chemical Society* 139.49 (2017), pp. 18009–18015.

[188] Tsung-Jen Liao et al. "High-affinity interactions of the nSH3/cSH3 domains of Grb2 with the C-terminal proline-rich domain of SOS1". In: *Journal of the American Chemical Society* 142.7 (2020), pp. 3401–3411.

[189] Kumud Majumder, Sangeeta Choudhury, and Raj K Bhatnagar. "Recombinant enrichment by exploitation of the wobble bases in the recognition site of long-cutters: design, synthesis and incorporation of zero-background linkers in cloning and expression vectors." In: *Gene* 163.1 (1995), pp. 167–168.

[190] Daan Frenkel and Berend Smit. *Understanding molecular simulation: from algorithms to applications*. Vol. 1. Elsevier, 2001.

[191] Evgeny B Stukalin et al. "Self-healing of unentangled polymer networks with reversible bonds". In: *Macromolecules* 46.18 (2013), pp. 7525–7541.

[192] Christoph Fröhner and Frank Noé. "Reversible interacting-particle reaction dynamics". In: *The Journal of Physical Chemistry B* 122.49 (2018), pp. 11240–11250.

[193] Robert S Hoy and Glenn H Fredrickson. "Thermoreversible associating polymer networks. I. Interplay of thermodynamics, chemical kinetics, and polymer physics". In: *The Journal of chemical physics* 131.22 (2009), p. 224902.

[194] Xiaoming Mao and Tom C Lubensky. "Maxwell lattices and topological mechanics". In: *Annual Review of Condensed Matter Physics* 9 (2018), pp. 413–433.

[195] AJ Bray. "Defect relaxation and coarsening exponents". In: *Physical Review E* 58.2 (1998), p. 1508.

[196] Peter Willis Voorhees. "Ostwald ripening of two-phase mixtures". In: *Annual Review of Materials Science* 22.1 (1992), pp. 197–215.

[197] P Taylor. "Ostwald ripening in emulsions". In: *Advances in colloid and interface science* 75.2 (1998), pp. 107–163.

[198] Lester O Hedges et al. *Decoupling of exchange and persistence times in atomistic models of glass formers*. 2007.

[199] Paul Cecil Martin, ED Siggia, and HA Rose. "Statistical dynamics of classical systems". In: *Physical Review A* 8.1 (1973), p. 423.

[200] Hans-Karl Janssen. "On a Lagrangean for classical field dynamics and renormalization group calculations of dynamical critical properties". In: *Zeitschrift für Physik B Condensed Matter* 23.4 (1976), pp. 377–380.

[201] C. de Dominicis. "TECHNIQUES DE RENORMALISATION DE LA THÉORIE DES CHAMPS ET DYNAMIQUE DES PHÉNOMÈNES CRITIQUES". In: *J. Phys. (Paris) Colloq.* 373 (1976).